

ABSTRACT

RUTKOWSKI, DAVID MATTHEW. Simulations to Predict the Phase Behavior and Structure of Multipolar Colloidal Particles. (Under the direction of Dr. Carol K. Hall).

Colloidal particles with anisotropic charge distributions can assemble into a number of interesting structures including chains, lattices and micelles that could be useful in biotechnology, optics and electronics. The goal of this work is to understand how the properties of the colloidal particles, such as their charge distribution or shape, affect the self-assembly and phase behavior of collections of such particles. The specific aim of this work is to understand how the separation between a pair of oppositely signed charges affects the phase behavior and structure of assemblies of colloidal particles. To examine these particles, we have used both discontinuous molecular dynamics (DMD) and Monte Carlo (MC) simulation techniques.

In our first study of colloidal particles with finite charge separation, we simulate systems of 2-D colloidal rods with four possible charge separations. Our simulations show that the charge separation does indeed have a large effect on the phase behavior as can be seen in the phase diagrams we construct for these four systems in the area fraction-reduced temperature plane. The phase diagrams delineate the boundaries between isotropic fluid, string-fluid and percolated fluid for all systems considered. In particular, we find that coarse gel-like structures tend to form at large charge separations while denser aggregates form at small charge separations, suggesting a route to forming low volume gels by focusing on systems with large charge separations.

Next we examine systems of circular particles with four embedded charges of alternating sign fixed to a triangular lattice. This system is found to form a limit periodic

structure, a theoretical structure with an infinite number of phase transitions, under specific conditions. The limit-periodic structure only forms when the rotation of the particles in the system is restricted to increments of $\pi/3$. When the rotation is restricted to increments of $\pi/6$ or the rotation is continuous, related structures form including a striped phase and a phase with nematic order. Neither the distance from the point charges to the center of the particle nor the angle between the charges influences whether the system forms a limit-periodic structure, suggesting that point quadrupoles may also be able to form limit-periodic structures. Results from these simulations will likely aid in the quest to find an experimental realization of a limit-periodic structure.

Next we examine the effect of charge separation on the self-assembly of systems of 2-D colloidal particles with off-center extended dipoles. We simulate systems with both small and large charge separations for a set of displacements of the dipole from the particle center. Upon cooling, these particles self-assemble into closed, cyclic structures at large displacements including dimers, triangular shapes and square shapes, and chain-like structures at small displacements. At extremely low temperatures, the cyclic structures form interesting lattices with particles of similar chirality grouped together. Results from this work could aid in the experimental construction of open lattice-like structures that could find use in photonic applications.

Finally, we present work in collaboration with Drs. Bhuvnesh Bharti and Orlin Velev in which we investigate how the surface coverage affects the self-assembly of systems of Janus particles coated with both an iron oxide and fatty acid chain layer. We model these particles by decorating a sphere with evenly dispersed points that interact with points on

other spheres through square-well interactions. The interactions are designed to mimic specific coverage values for the iron oxide/fatty acid chain layer. Structures similar to those found in experiment form readily in the simulations. The number of clusters formed as a function of surface coverage agrees well with experiment. The aggregation behavior of these novel particles can therefore, be described by a relatively simple model.

© Copyright 2016 by David Matthew Rutkowski

All Rights Reserved

Simulations to Predict the Phase Behavior and Structure of Multipolar Colloidal Particles

by
David Matthew Rutkowski

A dissertation submitted to the Graduate Faculty of
North Carolina State University
in partial fulfillment of the
requirements for the degree of
Doctor of Philosophy

Chemical Engineering

Raleigh, North Carolina

2016

APPROVED BY:

Dr. Carol K. Hall
Committee Chair

Dr. Keith E. Gubbins

Dr. Orlin D. Velev

Dr. Erik E. Santiso

Dr. Joseph B. Tracy

DEDICATION

This dissertation is dedicated to my mother, Anne Rutkowski, my father, Frank Rutkowski, and my brother, Mark Rutkowski, for their constant support and encouragement.

BIOGRAPHY

David Rutkowski was born in Reading, Pennsylvania to his parents Frank and Anne Rutkowski. David attended Wyomissing Area High School and graduated in 2006. He then attended the University of Pittsburgh and majored in chemical engineering. After completing his Bachelor of Science in May 2011 he began his graduate studies in the Department of Chemical and Biomolecular Engineering at North Carolina State University working under the direction of his advisor, Dr. Carol Hall.

ACKNOWLEDGMENTS

I would like to acknowledge and thank my PhD advisor, Dr. Carol Hall for guiding me throughout my graduate studies. I am particularly grateful to her for encouraging me to become more adept at public speaking and to focus my ideas as a writer. I would also like to thank Prof. Sabine Klapp, who advised me while I worked in Germany. Her insights and feedback will be missed. I am grateful to Dr. Josh Socolar for pointing out the importance of the structures I had found through earlier simulations and then giving me the benefit of his expertise on the double-dipole project. I wish to acknowledge the other members of my committee: Dr. Orlin Velev, Dr. Erik Santiso and Dr. Keith Gubbins for their helpful suggestions over the years. Specifically, I would like to thank Dr. Velev for the very useful discussions on experimental work and Dr. Santiso for several discussions on simulation. Finally, I am grateful to my collaborators, Dr. Bhuvnesh Bharti and Dr. Catherine Marcoux, for working with me on several interesting projects.

I would like to thank the Research Triangle MRSEC on Programmable Soft Matter for provided the majority of my support. Being a MRSEC fellow gave me ample opportunities to present my work and to receive feedback from students and professors across the Center. Additionally, the presentations of other students and the seminars gave me a much broader view of materials science than I would have had otherwise. I would like to acknowledge the NSF IRES grant that allowed me to travel to Germany several times; that collaboration was enlightening. I would also like to thank the U.S. Department of Education Graduate Assistance in Areas of National Need (GAANN) Computational Science Fellowship for providing partial financial support.

I would like to thank the members of the Hall research group for always being available for discussion. Firstly, I am grateful to Dr. Steven Benner and Dr. Binwu Zhao; your input over the years was truly invaluable. Additionally, I would like to thank Dr. Benner for introducing me to the importance of fitness; it helped balance out graduate school. I am indebted to Dr. Emily Curtis, Dr. Dave Latshaw and Ms. Lauren Ridge for introducing me to simulations and the lab, and for several helpful discussions regarding computer programming. Gary Gatling was also extremely helpful with setting up our computer system and ensuring that our system was always running, and for that I am very thankful. I would like to thank postdocs Dr. Xingqing Xiao, Dr. Qing Shao, Dr. Nathan Duff and Dr. Abhishek Singh for providing guidance. I am especially grateful to Dr. Shao and Dr. Duff for providing me with helpful insights into computer setup. Finally, I wish to thank Kye Won Wang, Yiming Wang, Ryan Maloney and Amelia Chen for useful discussions.

TABLE OF CONTENTS

LIST OF FIGURES	ix
CHAPTER 1	1
Motivation and Overview.....	1
1.1 Motivation.....	2
1.2 Overview.....	3
1.2.1 The Effect of Charge Separation on the Phase Behavior of Dipolar Colloidal Rods	4
1.2.2 Formation of Limit-periodic Structures by Double-dipole Particles Confined to a Triangular Lattice.....	4
1.2.3 Simulation Study on the Structural Properties of Colloidal Particles with Offset Dipoles.....	5
1.2.4 Capillary Bridging as a Tool for Assembling Discrete Clusters of Patchy Particles.....	5
1.2.5 Future Work.....	6
1.3 Publications.....	6
1.4 References.....	7
CHAPTER 2	9
The Effect of Charge Separation on the Phase Behavior of Dipolar Colloidal Rods	9
2.1 Introduction.....	12
2.2 Methods.....	19
2.3 Results.....	27
2.4 Discussion and Conclusions	31
2.5 Acknowledgements.....	36
2.6 References.....	37
Appendix 2-1 Discontinuous Potential Development.....	53
CHAPTER 3	55
Formation of Limit-periodic Structures by Double-dipole Particles Confined to a Triangular Lattice.....	55

3.1 Introduction.....	57
3.2 Methods.....	61
3.3 Results and Discussion	67
3.4 Discussion and Conclusions	75
3.5 Acknowledgements.....	78
3.6 References.....	79
CHAPTER 4	95
Simulation Study on the Structural Properties of Colloidal Particles with Offset	
Dipoles.....	95
4.1 Introduction.....	98
4.2 Model and Methods	101
4.3 Results and Discussion	107
4.4 Conclusions.....	117
4.5 Acknowledgements.....	119
4.6 References.....	120
CHAPTER 5	134
Capillary Bridging as a Tool for Assembling Discrete Clusters of Patchy Particles.....	134
5.1 Introduction.....	137
5.2 MC Simulation Details	139
5.2.1 Monodisperse interaction potential	140
5.2.2 Interaction potentials for a mixture of 4 μ m and 2 μ m spheres.....	141
5.3 Results and Discussion	141
5.3.1 Liquid-lipid driven particle clustering.....	142
5.3.2 Thermal switching of clusters	144
5.3.3 Monte Carlo simulations of patch particle clustering.....	145
5.3.4 Capillary bridging of complex particles and their mixtures.....	148
5.4 Conclusions.....	149
5.5 Acknowledgments.....	150
5.6 References.....	151

CHAPTER 6	166
Conclusions and Future Work	166
6.1 Conclusions.....	167
6.2 Future Recommendations	169
6.2.1 Simulations in External Fields.....	170
6.2.2 3d Offset Dipolar Spheres	171
6.2.3 Spheres with Four Embedded Point Dipoles.....	172
6.3 References.....	173

LIST OF FIGURES

- Figure 2.1.** Model of 4:1 dipolar rod used in our DMD simulations incorporating seven spheres bonded together to represent the excluded volume of the rod and two smaller spheres shown in red and blue at the ends to represent the charges of the extended dipole. The outermost square wells for the charged spheres are shown as dashed circles.....43
- Figure 2.2.** Plot of charge separation versus rod length both reduced by the rod width, which shows the regions where a head-tail pair of dipolar rods is preferred and where a side-side pair of dipolar rods is preferred. The dashed conformation delineation line shifts slightly depending on the potential used to model the interactions between the charged groups in the dipolar rod. The hashed region is infeasible because it has charge separations that are longer than the rod itself. The dotted line indicates the aspect ratio at which the simulations in this paper were performed.44
- Figure 2.3.** Plot comparing the continuous Yukawa potential energy and our discontinuous potential energy between charges of opposite sign versus the distance between the centers of the two charges. Charges with the same sign interact through a square shoulder that has the same energy boundaries and magnitudes, but has positive values of energy instead of negative.....45
- Figure 2.4.** Order parameters calculated in our simulations along with sample data (blue points) and curves fit to the data (red lines). (a) The definition of percolation probability and an example of a percolated system. (b) The definition of the extent of polymerization and an example of a string-fluid.46
- Figure 2.5.** (a) The definition of the head-tail order parameter and an image of a pair of rods that are head-tail ordered. (b) The definition of the side-side order parameter and an image of a pair of rods that are side-side ordered.47

Figure 2.6. Phase diagram for 4:1 dipolar rods with charge separation of 3.7 plotted in the area fraction vs temperature plane. Fluid, string-fluid, H-T string-fluid, H-T “gel” and H-T & S-S ordered “gel” phases are present in this diagram.	48
Figure 2.7. Phase diagram for dipolar rods with charge separation 3.5 plotted in the area fraction vs temperature plane. Fluid, string-fluid, H-T string-fluid, H-T “gel”, “gel”, and H-T and S-S “gel” are present.	49
Figure 2.8. Phase diagram of dipolar rods with 3.0 charge separation plotted in the area fraction vs temperature plane. Fluid, string-fluid, S-S “gel” and H-T and S-S “gel” are present.	50
Figure 2.9. Phase diagram of dipolar rods with charge separation 2.5 plotted in the area fraction vs temperature plane. Fluid, S-S string-fluid, and S-S “gel” are present. There is no H-T transition for this system; the rods always line up in S-S fashion.	51
Figure 2.10. The rod-rod potential energy vs. “joint” angle curves for the Yukawa potential (dashed lines) and our discontinuous potential (solid lines). The three-step discontinuous potential used in our simulations was derived by matching the rod-rod potential energy calculated for the continuous Yukawa potential with that for the discontinuous potential. Black, red and blue lines are for charge separation 3.7, 3.5 and 3.0, respectively.	52
Figure 3.1. (a) Black-stripe model in which the specific pattern of lines induces the formation of a limit-periodic structure upon slow temperature quench ¹¹ . (b) Double-dipole disk model with four charges of alternating sign. The charges in play a similar role to the top and bottom lines in (a); the horizontal bar in (a) is however absent in (b).	82
Figure 3.2. Double dipole disk model used in simulations where blue circles represent negative point charges and red circles represent positive point charges. θ and ϕ refer to fixed angles while δ refers to the distance between the center of the disk and a charge. The orientation of the particle is defined	

by the angle α , which for the orientation shown is equal to $\pi/3$. The orientation is therefore positive for clockwise rotations and negative for counterclockwise rotations.83

Figure 3.3. (a) Sublattice labeling with level-1 ordering shown in which sublattice A contains rattlers whose orientations are not shown. (b) Mapping used to define the value of e_x for an individual disk based on its orientation (up, left or right) and sublattice (A, B, C or D) (Figure adapted from Ref ¹¹). The 3D arrows shown inside the tetrahedrons are the four possibilities for the unit vector e_x 84

Figure 3.4. (a) Sublattice labeling with striped phase shown. (b) Mapping used to define the value of e_k for an individual disk based on its orientation and sublattice (A, B, C or D). The 3D arrows shown inside the octahedrons are the six possibilities for the unit vector e_k 85

Figure 3.5. Images of some of the non-limit-periodic-structures found in our simulations. The gray spheres represent the excluded area of the disk but are shown at reduced size to better visualize the orientation of the disks. Striped phases have alternating bands of disks whose order is determined by the striped order parameter. These stripes can also occur for just the rattlers as shown in the second image. The unidirectional rattler phase is investigated by first measuring ϕ_1 on the entire system and then calculating the nematic order parameter on the rattlers.86

Figure 3.6. Left: Image of a rattler (disk 6) and its surrounding six disks (disks 0-5) which are in a Kagome lattice configuration. Regardless of the orientation of the rattler, its potential energy of interaction with the surrounding six disks is zero. The dotted lines show four of the distances which cancel out pairwise according to the color of the lines. Right: Images showing the distortion of the rattlers in the α -rattler and the β -rattler phases with the perfectly aligned level-1 structure shown behind transparently. D_1 and D_2

refer to the two sublattices which contain disks which are rotated off of their level-1 structure while D_3 is the non-distorted sublattice.....87

Figure 3.7. (a) Striped order parameter, ψ_1 , versus reduced temperature T^* for continuous rotation simulations. Values of δ are shown in the legend. (b) ϕ_1 (filled symbols and solid lines) and nematic order parameter (open symbols and dashed lines) for continuous rotation simulations. Values of δ are shown in the legend.88

Figure 3.8. ψ_1 for $\delta \leq 0.25$ using the R6 moveset. Values in the legend indicate the value of δ89

Figure 3.9. ϕ_1 (a) and ψ_2 (b) vs. T^* for $\delta \geq 0.30$ using the R6 moveset. Note the difference in the horizontal scales on the two plots. Values in the legend indicate the value of δ90

Figure 3.10. Subset of the system (22x24 of a 64x64 system) at $\delta = 0.35$ using the R3 moveset color coded according to the level the disks are in. Gray corresponds to level-1, green to level-2, red to level-3, blue to level-4 and black is not ordered. The figure on the right plots ϕ_n for these four levels versus $\log(T^*)$91

Figure 3.11. Order parameters for four levels of order plotted versus $\tilde{\tau}$ where gray circles are for level-1, green crosses for level-2, red triangles for level-3 and blue x's for level-4.92

Figure 3.12. State diagram showing the different phases found for a given moveset as a function of δ . Red squares stand for striped phase, blue triangles for α -rattler phase, pink upside-down triangles for β -rattler phase, green diamonds for striped rattler phase and black circles for limit-periodic phase.93

Figure 4.1. Model of the offset-dipole sphere used in this work. The large sphere represents the excluded volume of the particle and has a diameter of σ . The two smaller spheres represent the locations of the positive (red) and

negative (blue) charges on the extended dipole. The charges do not, in actuality, have a physical size and are pictured here as spheres for clarity.123

Figure 4.2. Cosine of the angle between two extended dipoles for two offset dipoles confined to the x-y plane at their minimum potential energy (ground state) configuration as a function of the displacement, δ^* . Lines represent minimization of the pair potential energy as a function of δ^* for either a point dipole (black) ²³, Case 1 (red) and Case 2 (blue). Dashed lines are results for $k=0$ (Coulomb potential). Points are results from simulated annealing MC simulations.124

Figure 4.3. Ground state structures for systems of three particles for both Case 1 and Case 2. Images on the left show representative structures where the value below the image is δ^* for the particle and the numbers in parenthesis for Case 2 are the angle θ . The plots on the right display the Δ_{ij} for the three pairs of dipoles (Δ_{12} , Δ_{13} , Δ_{23}) as a function of δ^* . Colors on the right plots highlight regions where the corresponding structures on the left are the minimum energy structure.125

Figure 4.4 Ground state structures for systems of four particles for both Case 1 and Case 2. Images on the left show representative structures where the number below the image is the value of δ^* for the particle and the number in parenthesis for Case 2 is equal to θ . The plots on the right display the values of Δ_{ij} as a function of δ^* . Colors on the right plots highlight regions where the corresponding structures on the left are the minimum energy structure.....126

Figure 4.5. Plot showing the most stable cyclic structure as a function of the shift of the dipole, δ^* from the particle center, δ , for Case 1 and 2.127

Figure 4.6. Snapshots of low temperature systems at $\varphi = 0.1$ for $d^* = 0.01$ systems. Green indicates one chirality while purple the other. Numbers indicate the value of δ^* . T1 is a temperature below the polymerization transition but

	above the percolation transition and T2 is a temperature below the percolation transition for each system.	128
Figure 4.7.	a) Percolation and b) polymerization transition lines as functions of T for Case 1. Numbers in the legends indicate the value of δ^*	129
Figure 4.8.	Snapshots of structures formed in finite temperature simulations using Case 2. T1 is a temperature below the polymerization transition but above the percolation transition and T2 is a temperature below percolation transition for each system.	130
Figure 4.9.	a) Percolation and b) polymerization transition lines as functions of T for Case 2. Numbers in the legends indicate the value of δ^* while those in the parenthesis indicate the value of θ . The open circles are the percolation transitions for the fused cyclic cluster simulations which are described later.	131
Figure 4.10.	Fraction of particles that are in polygons, f_c , as a function of δ^* for a) Case 1 and b) Case 2. Numbers in the legends indicate the area fraction for each curve. These values were calculated for configurations at T2.....	132
Figure 4.11.	Structures formed from fused cyclic cluster simulations for particles with $d^* = 0.40$ at an area fraction of 0.1. Values below the images indicate the angle, θ , used in our model as shown in Figure 4.1.....	133
Figure 5.1.	(a) A schematic summarizing the general methodology for fabricating lipid patched polystyrene (PS) microspheres. (b) Interactions between all three surface-pairs of the patchy microparticle. Here the thickness of the liquid fatty acid layer and particle size are not to scale.	154
Figure 5.2.	(a) Optical micrographs illustrating the self-assembly of lipid-wetted Janus particles into ordered colloidal clusters in aqueous dispersion. The inset shows an SEM image of the Janus particles before assembly in the dried state. (b-e) Examples of 2D and 3D clusters formed by capillary binding of the microspheres. Scale bar in (a) 50 μm and (b) 5 μm	155

Figure 5.3. (a) The fraction of Janus particles self-assembled into clusters at different temperatures for ethanolamine salts of *n*-dodecanoic acid (squares) and *n*-hexadecanoic acid (circles). The vertical lines indicate the fluid-to-gel phase transition temperature (T_p) of the fatty acids on iron oxide surfaces. (b) and (c) The clusters disassembled upon decreasing the temperature below the fluid-to-gel phase transition of the fatty acid, i.e. when the liquid in the capillary bridge freezes. At temperature $T < T_p$, the fraction of assembled particles remains negligibly small. The corresponding schematics illustrate thermally reversible capillary bridge formation and rupturing. Scale bar in (b) 10 μm156

Figure 5.4. (a) Self-assemblies formed by the patchy particles ($f = 0.15$) in Monte Carlo simulations of the capillary assembly process. The inset shows an individual particle unit formed by distributing 252 domains on a central core. (b) Micrograph of patchy microspheres with fractional patch area of 0.15 assembled into low aggregation number clusters. (c-e) Surface interaction energy map for different patch sized particles ($f = 0.50, 0.20,$ and 0.15). The attractive interaction between the lipid coated patches was modeled on the basis of a square-well attractive potential. (f) The increase in the fraction of assembled particles upon increasing the relative patch area (f) in simulations (filled circles) and experiments (open squares). Scale bar in (b) 50 μm157

Figure 5.5. (a-c) Micrographs of the assemblies formed by a mixture of 4 μm and 2 μm Janus particles. (d-f) Capillary bridged self-assemblies formed by double-patched microspheres. The insets in the frames are the clusters observed in corresponding Monte Carlo simulations. Scale bar in each image is 2 μm158

Figure 5.6. SEM image of the single patched particles with relative surface patch area ' f ' (a) 0.2; and (b) $f = 0.15$. The value of fractional patch area (light grey region on the particles) was estimated by analyzing the micrographs using ImageJ software package. (c) SEM micrograph for double patched

particles where two distinct triangular patches were introduced onto the particles surface by metal vapor deposition from diagonally opposite sides. Scale bar = 4 μm	159
Figure 5.7. Determination of the zeta potential of iron oxide coated flat surface at pH 9.5. Here the zeta potential was determined by measuring the apparent zeta potential (or electrophoretic mobility) of tracer particles (-37 mV) away from the flat surface. The scattered points are experimentally measured data points and the red linear fit to the points.	160
Figure 5.8. Zeta potential of all surfaces present in the assembly dispersion. All the surfaces were negatively charged at pH 9.5 and hence electrostatically repulsive.....	161
Figure 5.9. Microscope images showing the dynamics of the self-assembly of Janus particles driven by lipid mediated capillary bridging. Mean cluster aggregation number increases as the assembly progresses. The kinetics of assembly is quantified in Figure 5.10. Scale in (c) = 50 μm	162
Figure 5.10. Monte Carlo simulation snapshots showing the near-equilibrium clusters formed by patchy particles with surface patch fraction (a) $f = 0.2$, and (b) $f = 0.5$. The red-red patches were attractive, and red-blue and blue-blue patches were repulsive.	163
Figure 5.11. Kinetics of particle clustering for different patch sized particles (a-b) $f = 0.15$, (c-d) $f = 0.20$, (e-f) $f = 0.50$. Both MC simulations (b, d, f) and experiments (a, c, f) show similar qualitative behavior where particles assemble (or reassemble) into higher aggregation number clusters with increasing assembly duration (or move number for simulations).....	164
Figure 5.12. Monte Carlo simulations snapshots for the equilibrium clusters formed by (a) Mixture of dissimilar sized particles Janus particles ($f = 0.5$), and (b) Double-patched particles.	165

CHAPTER 1

Motivation and Overview

1.1 Motivation

Colloidal systems consist of particles on the order of nanometers to micrometers suspended in a carrier fluid. Due to their size, these particles are assumed to behave classically, yet they are small enough to be affected by Brownian motion. These particles can self-assemble into complex structures under the effects of Brownian motion and are therefore attractive candidates for fabricating structures via a “bottom-up” procedure.

Colloidal particles which are not spherically symmetric with regards to one of their properties including shape ¹⁻⁵, charge distribution ⁶⁻¹⁰ and surface coating ¹¹ are of interest in a variety of fields including biotechnology, electronics, and photonics. The widespread excitement surrounding these so called anisotropic colloidal particles stems from their ability to self-assemble into complex phases and structures including micelles ¹² and open lattices ¹¹. One of the main goals of materials science is to program the interactions between individual colloidal particles so that the desired self-assembled structure is reliably obtained. To do this an understanding of how anisotropic particles behave is essential.

Furthering understanding of how the attributes of individual particles affect their self-assembly is a task well suited for simulation. Studying the behavior of these particles experimentally can be difficult due both to issues in creating monodisperse systems and the large parameter space of possible anisotropic colloidal particle characteristics. Simulation can therefore play a helpful role in determining the types of colloidal particles to further investigate in experiment. Models of colloidal particles which coarse grain out the solvent and consider the colloid as a single sphere have proven able to reproduce structures seen in

experiment and have been a useful tool for understanding how the interactions between particles affect the structures into which these particles assemble.

Models of particles with charge separation as their main anisotropy have been studied through simulation. The simplest model for a particle with a separation of charge is the dipolar hard sphere. Particles of this type have been simulated extensively and it has been found, rather unexpectedly, that they do not phase separate but instead form chains¹³⁻¹⁸. This chaining behavior leads to a proposed application as low volume fraction gels. Many additional types of charge asymmetry have been investigated via simulation including particles with higher moments such as quadrupolar and hexapolar spheres¹⁹, particles in time-dependent fields¹⁰, and cubes with embedded dipoles²⁰.

This thesis describes the results of simulations designed to investigate how the precise location of embedded charges within colloidal particles affects their self-assembly and ultimately their phase behavior. This work often focuses on the use of an extended rather than point dipole in which there is a finite separation distance between the two oppositely signed charges. The distance between these charges is found to have a large effect on the structure into which the particles ultimately assemble.

1.2 Overview

In this section a summary of the chapters composing the rest of the thesis is given. All chapters have their own literature review and references.

1.2.1 The Effect of Charge Separation on the Phase Behavior of Dipolar Colloidal Rods

Chapter 2 describes our results from simulations of monodisperse systems of dipolar rods with an embedded, extended dipole. We investigated particles with four different separation distances between the charges through two-dimensional discontinuous molecular dynamics simulation. Phase diagrams for these systems in the area fraction vs. temperature plane were constructed, outlining the polymerization and percolation boundaries. Two parameters were also developed that describe the number of head-tail and side-side partners present in a system. Ultimately we found that increasing the charge separation leads to an increased propensity to form head-tail partners and consequently space filling networks. We also determined that our gels went through a structural coarsening transition at low temperature driven by the side-side aggregation of chains formed at higher temperature.

1.2.2 Formation of Limit-periodic Structures by Double-dipole Particles Confined to a Triangular Lattice

Chapter 3 describes the results from Monte Carlo simulations of disks decorated with four charges of alternating sign fixed to a triangular lattice. These particles were found to form a limit-periodic structure upon annealing, but only when the rotation of the particles was restricted to increments of $\pi/3$. Allowing the disks more rotational freedom resulted in related phases including a striped phase and a partially-nematic-like phase. Additionally, we found that neither the distance the charges were from the center of the disk nor the angle affected whether they formed the limit-periodic structure, suggesting that even point quadrupolar systems may be able to form limit-periodic structure under the correct

conditions. The results from this paper outline a new, simple model that can form limit-periodic structures and further delineate the strict conditions which must be met for their formation.

1.2.3 Simulation Study on the Structural Properties of Colloidal Particles with Offset Dipoles

Chapter 4 describes results from Monte Carlo simulations of monodisperse systems of spheres in which the dipole is both extended and displaced a certain distance, δ , from the center of the particle. We place particular emphasis on comparing our results to similar simulation studies which focused on point dipoles. Since we use an intermediate-range Yukawa potential, we are able to explore phase space and outline the boundaries between fluid, string-fluid and percolated states. We find structures consistent with prior experiment and simulation work as well as several new structures. At extremely low temperatures and large shifts we find open lattice arrangements composed of smaller clusters of particles which may be useful in optical applications.

1.2.4 Capillary Bridging as a Tool for Assembling Discrete Clusters of Patchy Particles

Chapter 5 describes Monte Carlo simulation results taken from the paper “Capillary Bridging as a Tool for Assembling Discrete Clusters of Patchy Particles,” which describes the self-assembly of Janus particles covered with a metal and fatty acid chain layer. These particles are modeled by evenly dispersing points on the surface of spheres which interact with other points depending on their assigned type. We find good agreement between our

simulation results on the size of the cluster as a function of surface coverage of the particle and see aggregates similar to those found in experiment.

1.2.5 Future Work

Finally, in Chapter 6 we provide an outline for future work on the simulation of particles under the influence of external fields via both MC and continuous MD simulation, on the simulation of offset dipolar spheres in three dimensions rather than in quasi-2d as in Chapter 4, and on the simulation of a model involving four point dipoles rather than charges as in Chapter 3.

1.3 Publications

Chapters 2-5 are based on the following publications:

Chapter 2: D. M. Rutkowski, O. D. Velev, S. H. L. Klapp and C. K. Hall, “The Effect of Charge Separation on the Phase Behavior of Colloidal Rods” *Soft Matter*, 2016

Chapter 3: D. M. Rutkowski, C. Marcoux, J. E. S. Socolar, C. K. Hall, “Formation of limit-periodic structures by double-dipole particles confined to a triangular lattice” *Physical Review E*. Submitted

Chapter 4: D. M. Rutkowski, O. D. Velev, S. H. L. Klapp and C. K. Hall, “Simulation Study on the Structural Properties of Colloidal Particles with Offset Dipoles” In Preparation

Chapter 5: B. Bharti, D. Rutkowski, K. Han, A. U. Kumar, C. K. Hall and O. D. Velev, “Capillary Bridging as a Tool for Assembling Discrete Clusters of Patchy Particles” *JACS*, accepted

1.4 References

1. J. Yan, K. Chaudhary, S. C. Bae, J. A. Lewis and S. Granick, *Nature Communications*, 2013, 4, 1516 (DOI:10.1038/ncomms2520).
2. J. J. Crassous, A. M. Mihut, E. Wernersson, P. Pfliegerer, J. Vermant, P. Linse and P. Schurtenberger, *Nature Communications*, 2014, 5, 5516 (DOI:10.1038/ncomms6516).
3. J. W. Tavaoli, P. Bauer, M. Fermigier, D. Bartolo, J. Heuvingh and O. du Roure, *Soft Matter*, 2013, 9, 9103-9110 (DOI:10.1039/c3sm51589c).
4. C. W. Shields, S. Zhu, Y. Yang, B. Bharti, J. Liu, B. B. Yellen, O. D. Velev and G. P. Lopez, *Soft Matter*, 2013, 9, 9219-9229 (DOI:10.1039/c3sm51119g).
5. N. Yanai, M. Sindoro, J. Yan and S. Granick, *J. Am. Chem. Soc.*, 2013, 135, 34-37 (DOI:10.1021/ja309361d).
6. S. K. Smoukov, S. Gangwal, M. Marquez and O. D. Velev, *Soft Matter*, 2009, 5, 1285-1292 (DOI:10.1039/b814304h).
7. B. Ren, A. Ruditskiy, J. H. Song and I. Kretzschmar, *Langmuir*, 2012, 28, 1149-1156 (DOI:10.1021/la203969f).
8. A. Snezhko and I. S. Aranson, *Nature Materials*, 2011, 10, 698-703 (DOI:10.1038/NMAT3083).
9. S. Sacanna, L. Rossi and D. J. Pine, *J. Am. Chem. Soc.*, 2012, 134, 6112-6115 (DOI:10.1021/ja301344n).
10. J. Yan, M. Bloom, S. C. Bae, E. Luijten and S. Granick, *Nature*, 2012, 491, 578-+ (DOI:10.1038/nature11619).

11. Q. Chen, S. C. Bae and S. Granick, *Nature*, 2011, 469, 381-384
(DOI:10.1038/nature09713).
12. A. Walther and A. H. E. Mueller, *Chem. Rev.*, 2013, 113, 5194-5261
(DOI:10.1021/cr300089t).
13. L. Rovigatti, J. Russo and F. Sciortino, *Soft Matter*, 2012, 8, 6310-6319
(DOI:10.1039/c2sm25192b).
14. J. Weis, *Journal of Physics-Condensed Matter*, 2003, 15, S1471-S1495
(DOI:10.1088/0953-8984/15/15/311).
15. S. Klapp, *Journal of Physics-Condensed Matter*, 2005, 17, R525-R550
(DOI:10.1088/0953-8984/17/15/R02).
16. D. Levesque and J. Weis, *Physical Review E*, 1994, 49, 5131-5140
(DOI:10.1103/PhysRevE.49.5131).
17. J. Tavares, J. Weis and M. da Gama, *Physical Review E*, 1999, 59, 4388-4395
(DOI:10.1103/PhysRevE.59.4388).
18. P. Camp, J. Shelley and G. Patey, *Phys. Rev. Lett.*, 2000, 84, 115-118
(DOI:10.1103/PhysRevLett.84.115).
19. K. Van Workum and J. Douglas, *Phys Rev E.*, 2006, 73, 031502
(DOI:10.1103/PhysRevE.73.031502).
20. H. R. Vutukuri, F. Smalenburg, S. Badaire, A. Imhof, M. Dijkstra and A. van Blaaderen, *Soft Matter*, 2014, 10, 9110-9119 (DOI:10.1039/c4sm01778a).

CHAPTER 2

The Effect of Charge Separation on the Phase Behavior of Dipolar Colloidal Rods

Chapter 2 is essentially a manuscript by David M. Rutkowski, Orlin D. Velev, Sabine H. L. Klapp and Carol K. Hall accepted by Soft Matter.

The Effect of Charge Separation on the Phase Behavior of Dipolar Colloidal Rods

David M Rutkowski^a, Orlin D. Velev^a, Sabine H. L. Klapp^b and Carol K. Hall^{a*}

^aDepartment of Chemical and Biomolecular Engineering, North Carolina State University, 911 Partners Way, Raleigh, North Carolina 27695, USA

^bInstitute of Theoretical Physics, Technical University of Berlin, Str. EW 7-1 Hardenberstr. 36, D-10623 Berlin, Germany

Abstract

Colloids with anisotropic shape and charge distribution can assemble into a variety of structures that could find use as novel materials for optical, photonic, electronic and structural applications. Because experimental characterization of the many possible types of multi-shape and multipolar colloidal particles that could form useful structures is difficult, the search for novel colloidal materials can be enhanced by simulations of colloidal particle assembly. We have simulated a system of dipolar colloidal rods at fixed aspect ratio using discontinuous molecular dynamics (DMD) to investigate how the charge separation of an embedded dipole affects the types of assemblies that occur. Each dipolar rod is modeled as several overlapping spheres fixed in an elongated shape to represent excluded volume and two smaller, embedded spheres to represent the charges that make up the extended dipole. Large charge separations predominately form structures where the rods link head-to-tail while small charge separations predominately form structures where the rods stack side-by-side. Rods with small charge separations tend to form dense aggregates while rods with large

charge separations tend to form coarse gel-like structures. Structural phase boundaries between fluid, string-fluid, and “gel” (networked) phases are mapped out and characterized as to whether they have global head-to-tail or global side-by-side order. A structural coarsening transition is observed for particles with large charge separations in which the head-tail networks thicken as temperature is lowered due to an increased tendency to form side-by-side structures. Triangularly connected networks form at small charge separations; these may be useful for encapsulating smaller particles.

2.1 Introduction

Colloidal particles can assemble into a rich variety of structures that hold promise for application in biotechnology¹⁻³, photonics⁴⁻⁷, and electronics or computation⁸⁻¹⁰. When the shape, surface coating or internal charge distribution of the particles are anisotropic, the diversity of possible structures becomes even richer, offering enhanced opportunities for tuning the local order, leading to interesting and novel colloidal architectures including chains, crystals, gels and ribbons¹¹. Particles with anisotropic shape including suspensions of rod-shaped particles¹² can form both nematic and smectic phases, a feature useful in display devices¹³. Similarly, patchy particles including Janus particles can self-assemble into a multitude of different phases including giant micelles and bilayers¹⁴. These anisotropies can be manipulated through imposition of external fields leading to even better control over the structures formed¹⁵⁻¹⁸.

Not surprisingly, colloidal particles with anisotropic charge distributions exhibit complex phase behavior. Distributions of electric or magnetic charges in a colloidal particle can be treated as one or more embedded dipoles. The simplest type of colloidal particle with charge distribution is the dipolar sphere which has a single point-dipole located in its center. The anisotropic distribution of charge on dipolar spheres leads to a propensity to form chains, especially in response to external electric fields and, as a consequence, holds promise for creating photonic crystals with novel symmetries, electrical materials, and water-based electrorheological fluids^{11, 19, 20}. Manipulating these chains with external electric or magnetic fields may allow for the formation of materials with switchable properties such as switching from radiation absorber to reflectors¹¹. Here we consider dipolar rods - colloidal particles

with anisotropies in both shape and charge distribution - to obtain a basic understanding of how these two factors combine to yield interesting phase diagrams.

Dipolar colloidal rods display more complex phase behavior than particles with only one form of asymmetry, such as dipolar spherical particles or rod-shaped particles. For example, electrically dipolar rods have been created experimentally by Zhang et al. using PRINT which they found aligned in a head-to-tail fashion along an external electric field ²¹. Kozek et al. have synthesized nano-meter sized dipolar rods by coating a gold rod in silica and then attaching a magnetic overcoat to the silica layer. These particles have been found to align with an external electric field ²². Magnetic dipolar rods can be created experimentally by methods such as covering silica rods with a thin layer of nickel so that the rods become magnetically responsive ²³. These rods have been found to form cyclical structures that are responsive to an external field. Gold nanorods synthesized by Fava et al with cetyl trimethyl ammonium bromide (CTAB) on the sides and polystyrene molecules (PS) on the ends assemble into chains, side-side oriented chains, raft structures, and even spheres, depending on solvent quality ²⁴. Nanorods which instead have poly(N-isopropylacrylamide) (PNIPAm) on the ends, have been found to photothermally self-assemble into chains ²⁵. Many of the techniques used for fabricating multipolar particles suffer from either low yields or high polydispersity, limiting the practicality of experimentally investigating the bulk phase properties of these particles ¹⁹. As a consequence, most experimental and many simulation investigations, including this work, focus on the behavior of dipolar colloidal rods at surfaces.

A number of simulation techniques have been used to investigate the phase behavior of colloidal particles that are either rod-like, dipolar or both. Bolhuis and Frenkel found using a combination of Monte Carlo techniques and Gibbs-Duhem integration that the phase diagram for hard rods is highly dependent on their aspect ratio, displaying a nematic phase and smectic phase at moderate aspect ratios and densities¹². McGrother and Jackson used both canonical and Gibbs ensemble Monte Carlo (GEMC) to simulate a system of dipolar spherocylinders with a point dipole embedded in the center and found evidence for vapor-liquid coexistence as the aspect ratio increased²⁶. Alvarez and Klapp applied Monte Carlo simulations to systems of dipolar rods with permanent magnetic dipole moments modeled as fused magnetic dipolar spheres²⁷. Additionally, they investigated rod-like particles with a longitudinal point dipole and found clusters of parallel rods as we do in our simulations at low charge distances²⁸. Miller et al. used molecular dynamics to investigate systems of dipolar dumbbells, representing the dipole-dipole interaction by a combination of a soft-sphere interaction and Coulombic interaction, and found that these particles aligned into head-to-tail chains²⁹. Schmidle et al. performed simulations of two dimensional systems of dipolar spheres in the presence of electric fields and found close agreement between the structures formed in simulation and the experimentally observed structure formed by similar particles^{30, 31}. Goyal et al. showed using discontinuous molecular dynamics (DMD) simulations that three-dimensional systems of spherical dipolar colloidal particles³² form a number of phases including low volume fraction gels and high volume fraction hexagonally-close-packed, body centered tetragonal and face-centered cubic phases. Additionally, they found that mixtures of these particles formed bicontinuous gels³³. Like Goyal et al. we have

used a short-ranged potential designed to mimic electrostatic charges interacting in a high salt solution.

The long term goal of our investigation into the phase behavior of colloidal particles via molecular-level computer simulations is to screen the many types of structures formed by anisotropic particles so as to identify the ones that would be of interest for advanced applications. Molecular simulation has an advantage over experiment in this regard because precisely defined, monodisperse “molecules” of virtually any type can be generated. In contrast, many of the techniques for fabricating particles, including microcontact printing, Pickering emulsion techniques, and oil water emulsion techniques, cannot produce large quantities of monodisperse particles¹⁹. This makes it hard to identify the specific molecular features which are responsible for the behaviors of the particles. An attractive alternative, therefore, is to first identify interesting structures through computer simulation and then to explore these structures more precisely through experimentation.

The objective of the current research is to systematically investigate how the internal charge separation of dipolar colloidal rods affects the types of assemblies that occur over a range of temperatures and densities with the internal charge separation of the extended dipole being the control parameter. While others have investigated dipolar colloidal rods through simulation, the focus has usually been on how the aspect ratio of the rod affects the phase behavior^{27, 34} instead of how the internal charge separation affects the phase behavior, as we focus on in this work. A key consideration in the types of assemblies that form is the alignment of the particles at different conditions. A pair of rods can in general align in two orientations: either head-to-tail or side-by-side^{26, 27, 34}. In our model a shift between these

two orientations occurs when the charge separation is varied. The exact charge separation value that defines the boundary between these two orientations depends on both the aspect ratio of the rod and the expression for the potential energy of interaction between the electric charges, herein represented by a screened Coulomb potential, i.e. a Yukawa potential. A Yukawa potential was chosen because it allows for a faster evolution of the system than would a Coulomb potential with long range interactions. The simulations approach is used to map out the conditions under which a system of 2-d dipolar rods will predominantly align side-by-side or head-to-tail. While it can easily be determined if an isolated pair of particles will form head-tail or side-side pairs, the details of where these transitions occur in many particle systems and whether there are any other structural transitions is more challenging to discern without performing simulations.

Simulations of systems of dipolar particles can be classified according to how the dipole moment is represented: by a point dipole or by an extended dipole. Those simulations implementing a point dipole representation use the standard expression for the dipole-dipole interaction potential and are more suitable when the separation between the charges of the dipole is small ²⁶. The expression breaks down when the interparticle separation is on the same order of magnitude as the separation between the charges that make up the dipole. This can be dealt with by either adding higher order terms to the expansion, eg. quadrupolar, octapolar, etc., or by explicitly modeling the individual charges with an extended dipole ³⁵. Simulations with extended dipoles typically use a form of the Coulomb potential between the individual positive and negative charges on different molecules ^{29, 36} and are more appropriate when the two charges are separated by a distance on the same order or greater

than the distance separating the centers of the dipoles. Dipolar spheres with embedded, extended dipoles have been used in simulation to learn how the charge separation affects the phase behavior^{35, 37}. Simulations of dipolar rods with extended dipoles have also been performed but, as mentioned earlier, these have focused on how the aspect ratio of the rods, not the charge separation alone, affects the phase behavior³⁶. Because we are interested in how changing the charge separation within a dipolar rod affects phase behavior, we have chosen to explicitly model the charges on the dipole rather than use a point dipole representation.

The method we have chosen to use for our simulations of dipolar rods is discontinuous molecular dynamics simulations (DMD). Unlike typical molecular dynamics (MD) simulations in which the interaction between two particles is represented by a continuous function of the inter-particle distance, DMD uses potentials that are a discontinuous function of the inter-particle distance. The advantage of using a discontinuous potential is that when two particles are between discontinuities nothing needs to be calculated and the particles move ballistically. The particle velocities change only when the two particles reach a discontinuity. As a consequence, DMD moves through time by advancing between “collision” events rather than using a fixed time step as in MD. For this reason, DMD is an event-driven algorithm; it uses an event scheduling queue to determine the soonest to occur collision in the system and then updates the entire system to that time. The DMD algorithm is a much faster procedure than calculating the potential between each particle at the discrete uniformly-spaced time steps associated with MD. This speedup allows the simulation of longer timescales than would typically be possible and is applicable to our

system since rods take longer time to achieve their equilibrium state than spheres due to their extra rotational modes.

In this paper we present results from DMD simulations of dipolar rods modeled as spherocylinders with a length to width ratio of 4:1 for four values of the charge separation to width ratio (2.5, 3.0, 3.5, and 3.7). Our simulations were performed in 2-d, where 2-d means a two dimensional simulation box, to better correspond with experiments in which colloidal particles are placed on a glass slide or have sedimented onto a surface^{19, 38}. Since we are interested only in the general phase behavior of dipolar colloidal rods we have not modeled a specific system, but have developed a system guided by experimentally feasible parameters. We investigate the conditions at which the fluid phase, the string-fluid phase, the “gel” phase, the head-to-tail ordered phase, and the side-by-side ordered phase occur. The definitions of these phases are described in the Model and Methods section.

Our results include the following highlights. Phase diagrams in the area fraction vs. temperature plane have been calculated for all four charge separations investigated (2.5, 3.0, 3.5 and 3.7) which delineate boundaries between the three main phases investigated (fluid, string-fluid and “gel”) along with other transitions indicating the development of head-tail and side-side ordering. We also discovered a structural coarsening transition for systems of particles with charge separations 3.5 and 3.7; where structural coarsening refers to the thickening of network structures as head-tail “gels” formed at intermediate temperatures additionally form side-side structures at low temperatures. Rods with a charge separation of 3.0 form a mixed side-side and head-tail “gel” at low temperatures, which does not seem to be the equilibrium structure, suggesting the rods are dynamically arrested in a metastable

state. Rods that form head-tail aggregates percolate at higher temperatures than those that form side-side structures, with the shortest charge separation, 2.5, percolating only at intermediate area fractions.

2.2 Methods

We represented our 4:1 aspect ratio dipolar rod by a group of seven overlapping spheres, which are each separated from their nearest neighbor by a distance of 0.5σ resulting in an aspect ratio of 4:1; the spheres are bonded together to approximate the rod shape as shown in Figure 2.1. We chose to use an aspect ratio of 4:1 since this is closest to nanorods created by Wu and Tracy³⁹. We chose to use a distance of 0.5σ arbitrarily, but found it resulted in a small difference between the area of a true spherocylinder and our model as discussed in our conclusions section. Seven spheres are used based on the aspect ratio and distance between nearest spheres in the rod. Since DMD is an event-driven simulation technique, it is significantly easier to find collision times between particles if the particles are spheres rather than another shape. The positive and negative charges are represented by two smaller spheres embedded at selected locations near the ends of the dipolar rod; hence this is an extended dipole representation. The larger spheres have a diameter of σ while the smaller spheres representing the charges have a diameter of 0.3σ . The smaller spheres were chosen to have a diameter of 0.3σ to correspond with work performed previously by Goyal et al., but were otherwise chosen arbitrarily³². These larger spheres do not interact with each other on the same chain, and are bonded to nearest neighbors and next nearest neighbors using the method of Bellemans. The length of the bonds between neighboring spheres varies between

$(1 - \delta)\sigma$ and $(1 + \delta)\sigma$ where σ is the length of the bond between the centers of the spheres and δ is the so-called Bellemans' constant which is used to define how tightly the spheres are bound to each other ⁴⁰.

In our simulations we set δ equal to 7.654×10^{-3} in reduced units of length, which serves to keep the rod relatively straight, and keeps the angle between the center sphere and the two end spheres of the rod greater than or equal to 170 degrees. The Bellemans' constant for the smaller spheres is the same as that for the large spheres so that all the distances are consistent (i.e. all bonds can be at either their shortest or longest distance without any bond overlapping). The small spheres are bonded to the large sphere at the end of the rod that they are closest to. They are also bonded to each other so that they maintain their position within the rod. The small spheres are used only to localize the centers of the charge and do not interact with the uncharged spheres except through bonds within the rod.

The small spheres in different rods interact with each other via a square well (i.e. attractive) potential if the charges that the spheres represent are of opposite sign while they interact with a square shoulder (i.e. repulsive) potential if the charges are of the same sign. The square shoulder has the same boundaries and magnitude as the square well, but has positive energies instead of negative ones. The pair potential between charges on the ends of different rods was modeled as a three-step square-well or square-shoulder potential designed to approximate a Yukawa potential. The Yukawa potential, also known as the screened Coulomb potential, is defined as

$$U(r^*) = -\varepsilon/r^* \exp(-\kappa^*(r^* - 1)) \quad (1)$$

where $U(r^*)$ is the potential energy between a pair of charges with opposite sign, ϵ is a constant with units of energy related to the strength of the interaction, κ^* is the reduced inverse Debye screening length and r^* is the dimensionless distance, defined as $r^* = r/\sigma$, between two charges ⁴¹. The parameters for the Yukawa potential used in our simulation were chosen to be characteristic of rods with a diameter of 20 nm, the typical size of the gold nano-rods synthesized by Kozek et al. and Maity et al. ^{22, 42}, and suspended in a solution of 10^{-5} M NaCl. From these values, we calculated the Debye length, $1/\kappa$, to be 96.1 nm using the formula for 1:1 electrolytes, $1/\kappa = 0.304/[NaCl]^{0.5}$, where $[NaCl]$ is the concentration of NaCl in solution ⁴³. The reduced inverse Debye length, $\kappa^* = \sigma\kappa$, is thus 0.208. The reduced temperature for our simulations is $T^* = \tilde{T}k_B T/\epsilon$ where k_B is the Boltzmann constant, ϵ is the constant in the Yukawa potential, and \tilde{T} is equal to 0.864. \tilde{T} was calculated by setting our Yukawa potential equal to a simplified Coulomb potential, $U_C(r^*) = -1/r^*$, at the distance of closest approach for two charged spheres in our simulations, $r^* = 0.3$. The reduced area fraction in our simulations is defined as $\rho^* = \rho\sigma^2$.

For the continuous Yukawa potential just defined, we plot the boundary between head-tail dominated and side-side dominated regions in the reduced charge separation vs. rod length parameter space in Figure 2.2, creating a ground-state phase diagram for a pair of dipolar rods. This boundary is calculated by equating the total potential energy of a pair of rods in the head-tail configuration and a pair in the side-side configuration to give the charge separation at which the two configurations are equal in energy for a given rod length. This plot has the correct limiting behavior in that it predicts that dipolar spheres, which have a rod length of 1.0, should always form head-tail structures, regardless of the charge separation.

For our system of dipolar rods which has an aspect ratio of 4:1, the internal charge separation at which the head-tail and side-side configurations have the same interaction energy is 3.43 in reduced units of length.

The full definition of the three step discontinuous potential well used to model the interaction between centers of oppositely-signed charges on each rod is given below. The potential used between charges of the same sign has the same potential boundaries and energy magnitudes, but opposite signs for the epsilon values defined below, i.e. it is a square shoulder.

$$U_{SW}(r) = \begin{cases} \infty & \text{if } r < \sigma_1 \\ -\varepsilon_1 & \text{if } \sigma_1 < r < \sigma_2 \\ -\varepsilon_2 & \text{if } \sigma_2 < r < \sigma_3 \\ -\varepsilon_3 & \text{if } \sigma_3 < r < \sigma_4 \\ 0 & \text{if } r > \sigma_4 \end{cases} \quad (1)$$

The values of the interaction energy parameters are $\varepsilon_1 = 3.129$, $\varepsilon_2 = 1.717$, and $\varepsilon_3 = 0.719$ while the values for the well boundaries are $\sigma_1 = 0.3\sigma$, $\sigma_2 = 0.433\sigma$, $\sigma_3 = 0.595\sigma$, and $\sigma_4 = 1.1$. A comparison between this discontinuous potential and the Yukawa potential on which it is based is shown below in Figure 2.3. In the appendix we describe the procedure that we used to determine the ε and σ values listed above and the discontinuous potential between oppositely charged small spheres shown in Figure 2.3. Here we just point out that discontinuous charge-charge potential to mimic the Yukawa potential was chosen not by matching the charge-charge potential directly but by matching the total potential between a pair of dipolar rods, the “rod-rod potential”, over a variety of configurations.

We performed simulations at four values of the charge separation, two that should predominately form side-side aggregates, charge separations 2.5 and 3.0, and two that should

predominately form head-tail aggregates, charge separations 3.5 and 3.7. The only difference between these simulations was the distance between the charges in the embedded, extended dipole.

For all charge separations we followed the same simulation procedure. Our systems consisted of 500 dipolar rods with aspect ratio 4:1 in a square 2-d simulation box with periodic boundary conditions. As with regular MD, DMD is naturally performed in the NVE ensemble since energy is conserved between collisions. In order to implement constant temperature, we used the Andersen thermostat, in which a randomly-chosen particle collides with a “ghost” particle so that the system attains a Boltzmann distribution around the desired temperature⁴⁴. We started at a high reduced temperature, $T^* = 5.0$, in order to get a random configuration and then slowly lowered the temperature in a simulated annealing procedure. Simulated annealing allows us to examine structures that are close to equilibrium across a wide range of temperatures. The temperature was lowered in discrete steps; first in steps of 1.0 in reduced units, then steps of 0.1 from 2.0 to 0.30 and finally in steps of 0.01 from 0.30 to 0.01 allowing the system to equilibrate for 100 million collisions at each temperature step. We decrease the temperature in slower increments at lower temperatures because equilibrium takes longer to reach at lower temperatures. We stopped the cooling procedure once the temperature reached a value of 0.01. At this temperature a “gel” or aggregate structure had formed for all rods simulated. In order to determine what phase the system is in, we need to first define the clustering criterion for our particles. In our simulations we define two rods to be in the same cluster if oppositely charged spheres on this pair are within each other’s outermost well, which is 1.1σ . If the charges are of the same sign they are not counted as a

pair, since their interaction is repulsive instead of attractive as is required for a cluster to be established. If a rod is determined to be in a cluster with a second rod which is in turn in a cluster with a third rod all three rods will be considered to be in the same cluster. A cluster containing all of the particles in the system is therefore possible.

The percolation probability, Π , gives the probability of finding a spanning or percolating cluster in a given system and is defined as the number of configurations which have a cluster that is percolated, C_{per} , over the total number of configurations investigated, C .

$$\Pi = \langle C_{per}/C \rangle \quad (2)$$

A cluster is percolated if it connects to itself and spans the box, forming a cluster of infinite length when periodic images of the box are included. For a given configuration, the percolation state is 1 if the system is percolated and 0 if the system is not percolated⁴⁵. The percolation probability at a given temperature step in our simulations is the average of this percolation state over 20 configurations at that temperature. The boundary between the “gel” phase, which is associated with a system that is percolated, and the string-fluid phase, which is associated with a system that is not percolated, is determined by locating the inflection point in the percolation probability vs temperature curve. We determined the transition temperature between percolated and non-percolated states by plotting the percolation probability versus temperature and then fitting a tanh function to this curve in order to find the inflection point as shown in Figure 2.4(a). This inflection point gives the percolation temperature, which is the transition temperature between the string-fluid and “gel” phases⁴⁵.

The extent of polymerization, Φ , gives a measure of when the particles start to associate, and is defined as the ensemble average of the number of rods in the system that are in a cluster, N_a , divided by the number of rods in the system, N ,

$$\Phi = \langle N_a/N \rangle \quad (3)$$

The extent of polymerization varies between 0 and 1 since there cannot be more rods in a cluster than the number of rods in the system. The inflection point in a plot of the extent of polymerization versus temperature defines the boundary between fluid and string-fluid phases for a given area fraction as shown in Figure 2.4(b). In order to find the inflection point, we fit the extent of polymerization versus temperature to a logistic5 curve which has the form $\Phi = C_1 + (C_2 - C_1)/(1 + (C_3/T)^{C_4})^{C_5}$ which involves 5 fitting constants (C_1, C_2, C_3, C_4, C_5). We are not suggesting that this function underlies the relationship between the temperature and the extent of polymerization for our system, and have only used this function to get a smooth curve with which to find the inflection point.

Two order parameters were developed to determine whether the system is arranged in a head-to-tail or a side-to-side arrangement. A rod i is defined to have a head-tail partner if one of its charges is $< 1.1\sigma$ away from an oppositely signed charge on a neighboring rod j and the remaining charge on rod i is $\geq 1.1\chi$ away from the remaining charge on rod j (See Figure 2.5(a)). The parameter χ is the distance that the two farthest opposite charges are from each other when a pair of rods are at contact with one rod lying along the x-axis and the other lying along the y-axis. Thus, χ is equal to $\sigma/2\sqrt{2}[-1 + 2\sqrt{2} + 2l + n_s]$ where n_s is the number of spheres used in the rod model (in our case this is equal to seven) and l is equal to the separation distance between the charges on a single rod reduced by σ . A single rod can

have multiple head-tail partners, but our head-tail order parameter only measures whether or not a rod has at least one head-tail partner. The head-tail order parameter, H , is defined as the average number of rods with at least one head-tail partner, N_{H-T} , divided by the number of rods in the system.

$$H = \langle N_{H-T}/N \rangle \quad (4)$$

Like the extent of polymerization, the head-tail order parameter must be between 0 and 1. In order to determine the boundary between non-head-tail ordered and head-tail ordered we fit this order parameter versus temperature to a logistic5 curve as shown in Figure 2.5(a). The inflection point in this curve was taken to be this boundary.

A rod i is defined to have a side-side partner if one of its charges is $< 1.1\sigma$ away from an opposite charge on a neighboring rod j and the remaining charge on rod i is $< 1.1\chi$ away from the remaining charge on rod j (See Figure 2.5(b)). As with the head-tail order parameter, a single rod can have multiple side-side partners, but our side-side order parameter only measures whether or not a rod has at least one side-side partner. The side-side order parameter, S , is defined as the average of the number of rods that have at least one side-side partner, N_{S-S} , divided by the number of rods in the system.

$$S = \langle N_{S-S}/N \rangle \quad (5)$$

In order to determine the boundary between non-side-side ordered and side-side ordered we fit this order parameter versus temperature to a logistic5 curve. Again the inflection point in this curve versus temperature is taken to be the boundary between non-side-side ordered and side-side ordered as shown in Figure 2.5(b). Two rods cannot be both a head-tail pair and a side-side pair; the order parameters are defined in a way that they are exclusive of each other.

2.3 Results

We present the simulation results for four systems: two that should predominately form head-tail structures (internal charge separations of 3.7 and 3.5) and two that should predominately form side-side structures (internal charge separations of 3.0 and 2.5).

We first present the results for dipolar rods with an internal charge separation of 3.7. The phase diagram for this system plotted in the volume area fraction versus temperature plane is shown in Figure 2.6. As the system is cooled from a reduced temperature of 5.0, it first transitions from a fluid phase to a string-fluid phase. While each pair making up the clusters in this string-fluid has to be at least head-tail (H-T) ordered or side-side (S-S) ordered, the system as a whole is not considered S-S ordered or H-T ordered until the S-S order parameter or the H-T order parameter displays an inflection point. Thus the string-fluid at intermediate area fractions is neither H-T nor S-S ordered. This globally disordered string-fluid further transitions to a string-fluid with global H-T order, and so is called an H-T string fluid. Upon further cooling the system transitions to an H-T “gel”, and then further transitions to a “gel” with both H-T and S-S order. This last transition reflects a coarsening of the overall “gel” structure where the single strands of the H-T “gel” aggregate together to form S-S aggregates, resulting in a more compact structure. Images of both the head-tail ordered “gel” and the coarser “gel” (H-T and S-S) are shown in Figure 2.6 as well along with images of the string-fluid and fluid phases. At high area fractions the percolation line crosses the polymerization line resulting in the system being percolated at a higher temperature than that at which all the rods in the system have partners. This suggests that the system has a percolated group of rods but that not all rods in the system have a partner. A difficulty with

this high area fraction region, however, is that the polymerization probability always has a large value even at high temperatures because the particles are forced to be near each other due to area constraints. At higher area fractions, the polymerization probability indicates a transition from a state in which the majority of rods have a partner to a state in which all of the rods have a partner. This is in contrast to lower area fractions where the polymerization probability indicates the transition from a state in which no rods have a partner to a state in which most rods do have a partner. Thus as we increase area fraction our distance based clustering parameters may be misrepresenting where boundaries should occur.

Plots of the S-S order parameter versus temperature for charge separation 3.7 rods display a sudden decrease as the temperature is lowered just before the “gel” transition is reached at all area fractions. Before this dip, the S-S order parameter behaves as expected, increasing slightly as the temperature is decreased up to a reduced temperature of around 1. As the temperature is lowered further, the S-S order parameter first decreases and later increases as the “gel” structure coarsens. This dip in the S-S order parameter occurs roughly at the temperature where the H-T order parameter approaches 1. This suggests that the formation of the largest H-T ordered structures depletes some of the S-S partners that existed at higher temperatures. This is the only charge separation and order parameter which displays this behavior.

We next present the results for dipolar rods with an internal charge separation of 3.5. The phase diagram for this system is shown in Figure 2.7 It is very similar to that for charge separation of 3.7 with two main exceptions. The first exception is that the globally disordered string-fluid region for charge separation 3.5 exists over a wider range of temperatures than

for charge separation 3.7. The second exception is that the H-T order transition is shifted towards lower temperatures especially at higher area fractions. Consequently, this system transitions from a globally disordered gel phase into a H-T “gel” phase at area fractions above 0.35. Like the previous system, this system also displays a “gel” coarsening at the lowest temperatures where the system is a “gel” with both H-T and S-S order. At these low temperatures the S-S order parameter for this system is noticeably higher than for the previous system at the same temperature. This is consistent with the idea that as the charges move closer together the rods are more likely to form S-S pairs even though the dominant pair structure formed should still be H-T for this system. The higher S-S order parameter also results in thicker structures than in the charge separation 3.7 case, since there are more S-S pairs.

The third system investigated consists of dipolar rods with an internal charge separation of 3.0. This is the first of two systems considered that predominately form S-S structures. The phase diagram for this system is shown in Figure 2.8. As the temperature is lowered this system shows a transition from a fluid into a globally disordered string-fluid which, upon further cooling, transitions to a S-S string-fluid at high area fractions or a string-fluid which has both S-S and H-T order at low area fractions. Both of these string-fluids transition directly to a “gel” which has both H-T and S-S order as the temperature is lowered further. The occurrence of this H-T and S-S “gel” phase does not seem to indicate a coarsening as it did in the charge separation 3.5 and 3.7 cases since the “gel” phase that forms has a very open structure with groupings of three rods forming triangular aggregates as

can be seen in Figure 2.8. While triangular aggregates are unusual for systems of dipolar spheres they have been seen in prior simulations of dipolar rods³⁶.

The fourth and final system investigated consists of dipolar rods with an internal charge separation of 2.5. Since the charges on the rods with an internal charge separation of 2.5 are far from the ends of the rods, the rods do not experience any attraction if they are in H-T alignment using our discontinuous potential. This obviously favors the formation of S-S structures. Consequently, this system transitions from a fluid to an S-S string-fluid at all area fractions as can be seen in the phase diagram for this system in Figure 2.9. For this system the polymerization probability curve nearly coincides with the S-S order curve, which further indicates the particles are only ordering in an S-S fashion. Upon further cooling and at intermediate area fractions this S-S string-fluid transitions to a coarse S-S “gel”. At low area fractions (below 0.25) and at very high area fractions (above 0.60) the system does not have a stable percolation transition. Examples of non-percolated structures at very low and very high area fractions are shown in Figure 2.9. The absence of a percolation transition at low area fraction is likely a consequence of the S-S ordering of the system. S-S aggregates have a more difficult time spanning the box than H-T aggregates since the S-S aggregates have smaller aspect ratios than the H-T aggregates. We believe that the disappearance of the percolation transition at high area fractions occurs because the system is jammed. The S-S clusters form individual domains instead of long structures which percolate. Although percolated structures may be the true equilibrium structure, our system does not reach this state and becomes stuck in a metastable, non-percolated state. Interestingly, a similar

structure has been seen experimentally with rods that have surfactant molecules attached to their sides ⁴⁶ and in simulations of 2-d spherocylinders ⁴⁷.

2.4 Discussion and Conclusions

We have calculated phase diagrams for monodisperse systems of 4:1 dipolar colloidal rods with internal charge separations of 3.7, 3.5, 3.0, and 2.5 using discontinuous molecular dynamics simulations with a charge–charge potential that is a discontinuous approximation to a Yukawa potential. These phase diagrams displayed fluid, string-fluid and “gel” phases which were further characterized either by H-T or S-S ordering of the rods. We found a gel coarsening transition for systems of dipolar rods with charge separations of 3.5 and 3.7 which was indicated by an increase in the S-S order parameter. Dipolar rods with charge separations of 3.0 were found to form “gels” with mixed S-S and H-T ordered structures. Dipolar rods with charge separations of 2.5 formed coarse “gels” containing only S-S structures over a limited range of area fractions. Consideration of the four cases discussed indicates that as the charge separation is decreased, the temperature at which the percolation transition occurs shifts to lower values. The main reason for this is that the interactions between the charges become weaker as the charge separation is reduced since the charges become further embedded within the rod. The fluid to string-fluid boundaries also shift towards lower temperatures as the charge separation is reduced for the same reason.

The novel aspects of our contribution are the following. While others have investigated how the rod aspect ratio affects the phase behavior ^{27, 34} we instead focus solely on the internal charge separation. We find that coarse gel-like structures form at high charge

separations while denser aggregates form at low charge separations. This suggests that in order to readily form low volume fraction gel structures, the internal charge separation within dipolar colloidal particles should be large as possible. We find triangularly connected networks at charge separation 3.0, which may be of use for encapsulating smaller particles. An intriguing gel coarsening transition occurs for the two largest charge separations investigated, which suggests using temperature to control the density of a gel of rod-like colloidal particles. Our simulations illustrate how the area fractions, connectivity and coarseness of gel structures can be tuned on the basis of the type of rod-like particles undergoing assembly. The structures formed in our simulations could constitute model systems for low volume fraction gels or materials whose properties (e.g. viscosity, conductivity, etc.) are controllable by dialing in the core-shell parameters for the individual colloidal particles or the strength of the magnetic or electric field polarization.

By determining which self-assembled structures our dipolar rods can possibly form and at what conditions, we have aided our experimental colleagues in determining the types of phases and structures which will form from various synthesized core-shell rod-like particles. An example of such a core-shell particle is a ferromagnetic nanorod with an inorganic shell overcoat, the thickness of which could determine whether these magnetic dipoles form head-to-tail or side-by-side structures, i.e., the relevant regions on Figure 2.2⁴². The magnitude of the dipole could be controlled by the changing the strength of the external field, leading to the polarization of the ferromagnetic core. Though the structures formed at low temperatures in our simulations may not be equilibrium states, they may still represent

states which could be experimentally accessible through rapid cooling or rapid gel-formation after momentary magnetic polarization.

Our use of DMD and a rod model with short range interactions was motivated by our desire to highlight regions of the phase diagram for further investigation by experimentalists. This combination of model and simulation technique allowed us to investigate these complex particles quickly and efficiently. The main advantage of DMD is the limited computational resources required (a single processor workstation) in comparison to simulation techniques which use continuous potentials. While the speed of continuous potential simulation techniques has increased through the creation of parallel algorithms, DMD still allows us to simulate more systems in a short time frame given limited computational resources. Though our simulations focused on situations with high salt concentration where short-range interactions were appropriate, it is interesting that the aggregate structures obtained from our simulations appear similar to those obtained in simulations employing long range interactions. Accounting for long range continuous potentials is often the most time consuming part of a simulation; obtaining results which could be qualitatively correct via short range potentials is an attractive idea ⁴⁸.

The structures formed in our simulations appear consistent with those found by others who have simulated dipolar rods. For instance, McGrother et al. found that dipolar rods with an embedded point dipole form S-S structures when the aspect ratio is greater than or equal to 2:1 and H-T structures when the aspect ratio is smaller ²⁶. Varying the aspect ratio of a rod with a point-dipole is equivalent to exploring the x axis in our Figure 2.2; the switch between H-T and S-S on this line occurs at an aspect ratio of approximately 1.30:1, which is

consistent with what McGrother et al. had found. Simulations by Aoshima and Satoh of dipolar rods with an extended dipole form H-T and S-S structures as well as higher order structures including triangular and double chain structures³⁶. By simulating rods of several aspect ratios with the same difference between rod length and charge separation, they found that the structures formed in their simulations switched from H-T dominated to S-S dominated as the aspect ratio increased. Their systems would fall on a line parallel to the boundary between the H-T favored and the infeasible region in Figure 2.2. According to Figure 2.2, all three of their charge separations would be in the S-S favorable region. This suggests that if we were to simulate the same particles we would likely obtain different results from Aoshima and Satoh, and our system would be predominately S-S structures and would not switch to an H-T dominated system. Our results also appear to be consistent with simulations of magnetic nanorods composed of fused dipolar spheres performed by Alvarez and Klapp²⁷. They do not find nematic order at our aspect ratio regardless of the interaction energy and their percolation transitions occur at decreasing volume fraction as the interaction energy is increased (temperature decreased).

Since the type of behavior observed, phase separation or self-assembly into chains, has been found to depend on the type of model used, at least for dipolar spheres, it is instructive to compare the types of behaviors that we observe for dipolar rods with those observed using other models.³⁷ Grand canonical Monte Carlo simulations of hard sphere point dipoles⁴⁹, Wang-Landau simulations of Stockmayer fluids with high dipole strength⁵⁰, and Monte Carlo simulations of hard sphere extended dipoles³⁷ all result in the formation of chains of particles, while simulations of the Stockmayer fluid with low dipole strength appear

to exhibit vapor-liquid equilibrium ⁵¹. Both simulations of dipolar spherocylinders and dipolar dumbbells have found ranges of aspect ratios where vapor-liquid coexistence occurs ^{26, 52, 53}. Since our model does not include a Stockmayer-like potential and our aspect ratio is significantly above the aspect ratio where spherocylinders display vapor-liquid coexistence, we would expect that our simulations would not display vapor-liquid equilibrium and would instead form chains of particles.

Though small, the differences between the model used in our simulations and a true spherocylinder could potentially lead to anomalous behavior. The percent difference in area between a spherocylinder and the rod used in our simulation is 3.44% due to small gaps between the spheres in our model. If these gaps are too large, they could cause the rods to stack in an offset manner or potentially cause the rods to have a more difficult time sliding past each other at high area fractions. Donaldson and Kantorovich have encountered an analogous situation where cubes constructed from spheres were found to stack closer to each other than true cubes would; these authors surmise that this is the cause of the slight discrepancy observed between their theory and simulation results ⁵⁴. We have not, however, observed our rods stacking in an offset manner in our simulations. Unlike many rod models, ours is not infinitely stiff. This may allow rod particles in our simulations to diffuse past each other more easily than true spherocylinders would. However, we have calculated the persistence length of our rods without charges to be $38.7\sigma \pm 2.6\sigma$, which is significantly higher than our rod length of 4.0σ .

One issue with all of our simulations is whether the structures we measure are equilibrium in nature or simply long lived transient states. The low area fraction non-

percolated structure in Figure 2.9 in particular suggests that we are not reaching a true equilibrium state since the clusters do not aggregate together even though there is seemingly nothing keeping them apart. For the conditions in this region (charge separation 3.5, low area fraction, low temperature) in particular we ran simulations which were twice as long but we were unable to obtain appreciably different results. From this, we cannot rule out that our simulations may simply be long lived transient states, and our phase diagrams are therefore not describing equilibrium structures. We suggest that our simulations may be limited by both the tight bonding we had to implement in order to maintain a rigid rod shape and the implementation of our Andersen thermostat which tended to slow down the dynamics of the system. Simulations using a rigid rod with a different thermostat may have a higher chance of reaching a state more suggestive of equilibrium.

2.5 Acknowledgements

This work was supported by the Research Triangle MRSEC under grant number DMR-1121107, the US National Science Foundation under grant OISE 1065466 and the German Research Foundation (DFG) through grant IRTG 1524.

2.6 References

1. S. Mitragotri and J. Lahann, *Nature Materials*, 2009, 8, 15-23
(DOI:10.1038/NMAT2344).
2. F. Caruso, R. A. Caruso and H. Mohwald, *Science*, 1998, 282, 1111-1114
(DOI:10.1126/science.282.5391.1111).
3. D. A. Giljohann, D. S. Seferos, W. L. Daniel, M. D. Massich, P. C. Patel and C. A. Mirkin, *Angewandte Chemie-International Edition*, 2010, 49, 3280-3294
(DOI:10.1002/anie.200904359).
4. S. Kredentser, O. Buluy, P. Davidson, I. Dozov, S. Malynych, V. Reshetnyak, K. Slyusarenko and Y. Reznikov, *Soft Matter*, 2013, 9, 5061-5066
(DOI:10.1039/c3sm27881f).
5. Y. Li, W. Cai and G. Duan, *Chemistry of Materials*, 2008, 20, 615-624
(DOI:10.1021/cm701977g).
6. A. Hynninen, J. H. J. Thijssen, E. C. M. Vermolen, M. Dijkstra and A. Van Blaaderen, *Nature Materials*, 2007, 6, 202-205 (DOI:10.1038/nmat1841).
7. J. Baumgartl, M. Zvyagolskaya and C. Bechinger, *Phys. Rev. Lett.*, 2007, 99, 205503
(DOI:10.1103/PhysRevLett.99.205503).
8. Y. Chen, X. Ding, S. S. Lin, S. Yang, P. Huang, N. Nama, Y. Zhao, A. A. Nawaz, F. Guo, W. Wang, Y. Gu, T. E. Mallouk and T. J. Huang, *Acs Nano*, 2013, 7, 3306-3314
(DOI:10.1021/nm4000034).
9. D. J. Milliron, S. M. Hughes, Y. Cui, L. Manna, J. B. Li, L. W. Wang and A. P. Alivisatos, *Nature*, 2004, 430, 190-195 (DOI:10.1038/nature02695).

10. C. L. Phillips, E. Jankowski, B. J. Krishnatreya, K. V. Edmond, S. Sacanna, D. G. Grier, D. J. Pinei and S. C. Glotzer, *Soft Matter*, 2014, 10, 7468-7479 (DOI:10.1039/c4sm00796d).
11. B. Bharti and O. D. Velev, *Langmuir*, 2015, 31, 7897-7908 (DOI:10.1021/la504793y).
12. P. Bolhuis and D. Frenkel, *J. Chem. Phys.*, 1997, 106, 666-687 (DOI:10.1063/1.473404).
13. M. J. Solomon and P. T. Spicer, *Soft Matter*, 2010, 6, 1391-1400 (DOI:10.1039/b918281k).
14. A. Walther and A. H. E. Mueller, *Soft Matter*, 2008, 4, 663-668 (DOI:10.1039/b718131k).
15. A. A. Shah, B. Schultz, W. Zhang, S. C. Glotzer and M. J. Solomon, *Nature Materials*, 2015, 14, 117-124 (DOI:10.1038/NMAT4111).
16. A. Snezhko and I. S. Aranson, *Nature Materials*, 2011, 10, 698-703 (DOI:10.1038/NMAT3083).
17. J. J. Crassous, A. M. Mihut, E. Wernersson, P. Pfliegerer, J. Vermant, P. Linse and P. Schurtenberger, *Nature Communications*, 2014, 5, 5516 (DOI:10.1038/ncomms6516).
18. K. J. Lee, J. Yoon, S. Rahmani, S. Hwang, S. Bhaskar, S. Mitragotri and J. Lahann, *Proc. Natl. Acad. Sci. U. S. A.*, 2012, 109, 16057-16062 (DOI:10.1073/pnas.1213669109).

19. O. Cayre, V. Paunov and O. Velev, *Journal of Materials Chemistry*, 2003, 13, 2445-2450 (DOI:10.1039/b308817k).
20. I. D. Hosein, M. Ghebrebrhan, J. D. Joannopoulos and C. M. Liddell, *Langmuir*, 2010, 26, 2151-2159 (DOI:10.1021/la902609s).
21. H. Zhang, J. K. Nunes, S. E. A. Gratton, K. P. Herlihy, P. D. Pohlhaus and J. M. DeSimone, *New Journal of Physics*, 2009, 11, 075018 (DOI:10.1088/1367-2630/11/7/075018).
22. S. Maity, W. Wu, C. Xu, J. B. Tracy, K. Gundogdu, J. R. Bochinski and L. I. Clarke, *Nanoscale*, 2014, 6, 15236-15247 (DOI:10.1039/c4nr05179c).
23. J. Yan, K. Chaudhary, S. C. Bae, J. A. Lewis and S. Granick, *Nature Communications*, 2013, 4, 1516 (DOI:10.1038/ncomms2520).
24. D. Fava, Z. Nie, M. A. Winnik and E. Kumacheva, *Adv Mater*, 2008, 20, 4318-4322 (DOI:10.1002/adma.200702786).
25. D. Fava, M. A. Winnik and E. Kumacheva, *Chemical Communications*, 2009, , 2571-2573 (DOI:10.1039/b901412h).
26. S. McGrother and G. Jackson, *Phys. Rev. Lett.*, 1996, 76, 4183-4186 (DOI:10.1103/PhysRevLett.76.4183).
27. C. E. Alvarez and S. H. L. Klapp, *Soft Matter*, 2012, 8, 7480-7489 (DOI:10.1039/c2sm25636c).
28. C. E. Alvarez and S. H. L. Klapp, *Soft Matter*, 2013, 9, 8761-8770 (DOI:10.1039/c3sm51549d).

29. M. A. Miller, R. Blaak, C. N. Lumb and J. Hansen, *J. Chem. Phys.*, 2009, 130, 114507 (DOI:10.1063/1.3089620).
30. H. Schmidle, C. K. Hall, O. D. Velev and S. H. L. Klapp, *Soft Matter*, 2012, 8, 1521-1531 (DOI:10.1039/c1sm06576a).
31. H. Schmidle, S. Jaeger, C. K. Hall, O. D. Velev and S. H. L. Klapp, *Soft Matter*, 2013, 9, 2518-2524 (DOI:10.1039/c2sm27210e).
32. A. Goyal, C. K. Hall and O. D. Velev, *Physical Review E*, 2008, 77, 031401 (DOI:10.1103/PhysRevE.77.031401).
33. A. Goyal, C. K. Hall and O. D. Velev, *Soft Matter*, 2010, 6, 480-484 (DOI:10.1039/b907873h).
34. M. Aoshima and A. Satoh, *J. Colloid Interface Sci.*, 2004, 280, 83-90 (DOI:10.1016/j.jcis.2004.07.025).
35. V. Ballenegger and J. P. Hansen, *Mol. Phys.*, 2004, 102, 599-609 (DOI:10.1080/00268970410001675554).
36. M. Aoshima and A. Satoh, *J. Colloid Interface Sci.*, 2006, 293, 77-87 (DOI:10.1016/j.jcis.2005.06.035).
37. M. Valisko, T. Varga, A. Baczoni and D. Boda, *Mol. Phys.*, 2010, 108, 87-96 (DOI:10.1080/00268970903514553).
38. S. Gangwal, O. J. Cayre, M. Z. Bazant and O. D. Velev, *Phys. Rev. Lett.*, 2008, 100, 058302 (DOI:10.1103/PhysRevLett.100.058302).
39. W. Wu and J. B. Tracy, *Chemistry of Materials*, 2015, 27, 2888-2894 (DOI:10.1021/cm504764v).

40. A. Bellemans, J. Orban and D. Vanbelle, *Mol. Phys.*, 1980, 39, 781-782
(DOI:10.1080/00268978000100671).
41. J. Bergenholtz and M. Fuchs, *Journal of Physics-Condensed Matter*, 1999, 11,
10171-10182 (DOI:10.1088/0953-8984/11/50/310).
42. K. A. Kozek, K. M. Kozek, W. Wu, S. R. Mishra and J. B. Tracy, *Chemistry of
Materials*, 2013, 25, 4537-4544 (DOI:10.1021/cm402277y).
43. J. N. Israelachvili, *Intermolecular and surface forces*, Academic Press, Burlington,
MA, 2011.
44. H. Andersen, *J. Chem. Phys.*, 1980, 72, 2384-2393 (DOI:10.1063/1.439486).
45. H. Neitsch and S. H. L. Klapp, *J. Chem. Phys.*, 2013, 138, 064904
(DOI:10.1063/1.4790406).
46. M. Li, H. Schnablegger and S. Mann, *Nature*, 1999, 402, 393-395.
47. M. A. Bates and D. Frenkel, *J. Chem. Phys.*, 2000, 112, 10034-10041
(DOI:10.1063/1.481637).
48. C. J. Fennell and J. D. Gezelter, *J. Chem. Phys.*, 2006, 124, 234104
(DOI:10.1063/1.2206581).
49. P. Camp, J. Shelley and G. Patey, *Phys. Rev. Lett.*, 2000, 84, 115-118
(DOI:10.1103/PhysRevLett.84.115).
50. G. Ganzenmueller and P. J. Camp, *J. Chem. Phys.*, 2007, 127, 154504
(DOI:10.1063/1.2794042).
51. H. Schmidle and S. H. L. Klapp, *J. Chem. Phys.*, 2011, 134, 114903
(DOI:10.1063/1.3564916).

52. J. C. Shelley, G. N. Patey, D. Levesque and J. J. Weis, *Physical Review E*, 1999, 59, 3065-3070 (DOI:10.1103/PhysRevE.59.3065).
53. G. Ganzenmuller and P. J. Camp, *J. Chem. Phys.*, 2007, 126, 191104 (DOI:10.1063/1.2738059).
54. J. G. Donaldson and S. S. Kantorovich, *Nanoscale*, 2015, 7, 3217-3228 (DOI:10.1039/c4nr07101h).

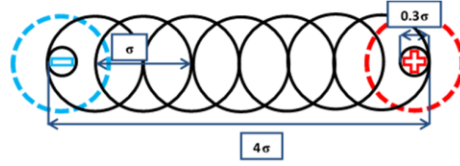


Figure 2.1. Model of 4:1 dipolar rod used in our DMD simulations incorporating seven spheres bonded together to represent the excluded volume of the rod and two smaller spheres shown in red and blue at the ends to represent the charges of the extended dipole. The outermost square wells for the charged spheres are shown as dashed circles.

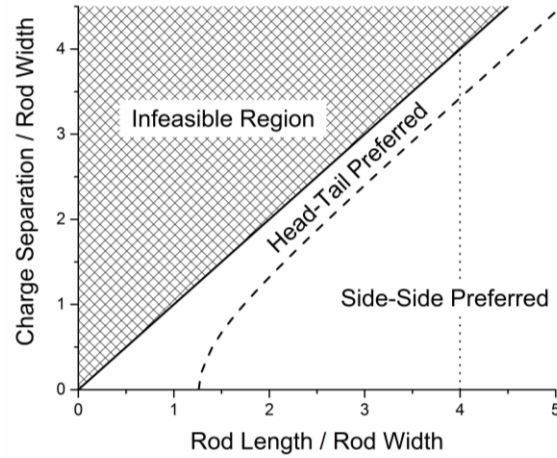


Figure 2.2. Plot of charge separation versus rod length both reduced by the rod width, which shows the regions where a head-tail pair of dipolar rods is preferred and where a side-side pair of dipolar rods is preferred. The dashed conformation delineation line shifts slightly depending on the potential used to model the interactions between the charged groups in the dipolar rod. The hashed region is infeasible because it has charge separations that are longer than the rod itself. The dotted line indicates the aspect ratio at which the simulations in this paper were performed.

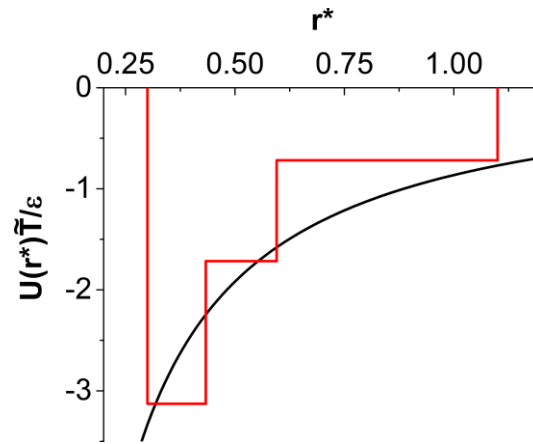


Figure 2.3. Plot comparing the continuous Yukawa potential energy and our discontinuous potential energy between charges of opposite sign versus the distance between the centers of the two charges. Charges with the same sign interact through a square shoulder that has the same energy boundaries and magnitudes, but has positive values of energy instead of negative.

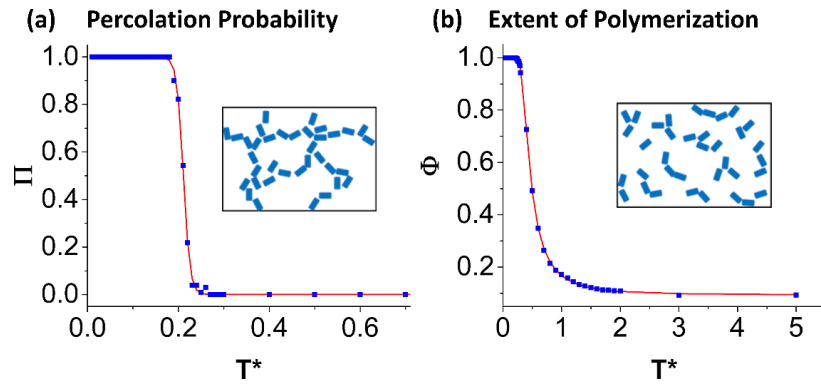


Figure 2.4. Order parameters calculated in our simulations along with sample data (blue points) and curves fit to the data (red lines). (a) The definition of percolation probability and an example of a percolated system. (b) The definition of the extent of polymerization and an example of a string-fluid.

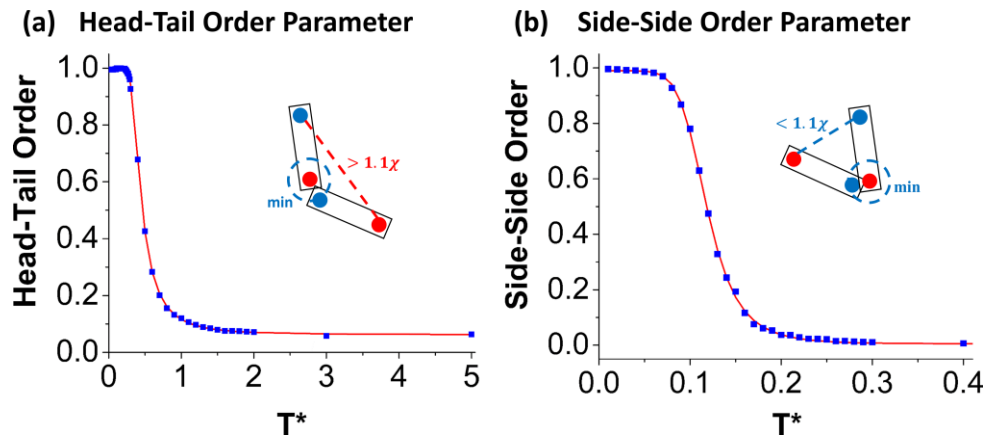


Figure 2.5. (a) The definition of the head-tail order parameter and an image of a pair of rods that are head-tail ordered. (b) The definition of the side-side order parameter and an image of a pair of rods that are side-side ordered.

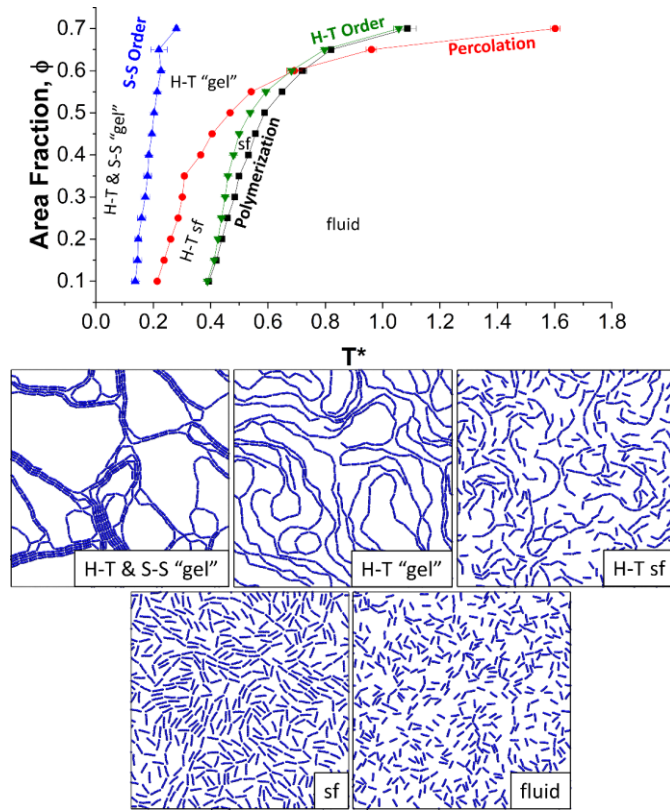


Figure 2.6. Phase diagram for 4:1 dipolar rods with charge separation of 3.7 plotted in the area fraction vs temperature plane. Fluid, string-fluid, H-T string-fluid, H-T “gel” and H-T & S-S ordered “gel” phases are present in this diagram.

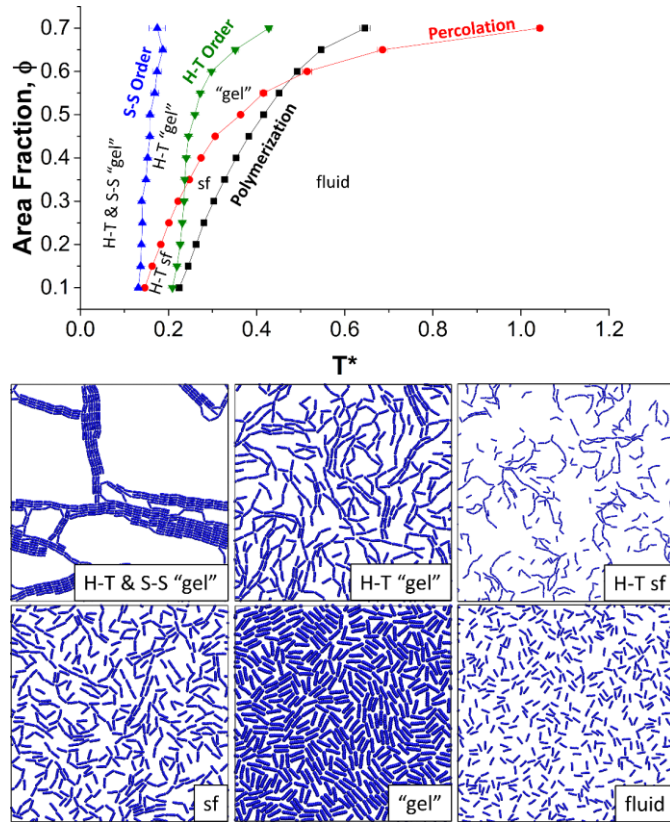


Figure 2.7. Phase diagram for dipolar rods with charge separation 3.5 plotted in the area fraction vs temperature plane. Fluid, string-fluid, H-T string-fluid, H-T "gel", "gel", and H-T and S-S "gel" are present.

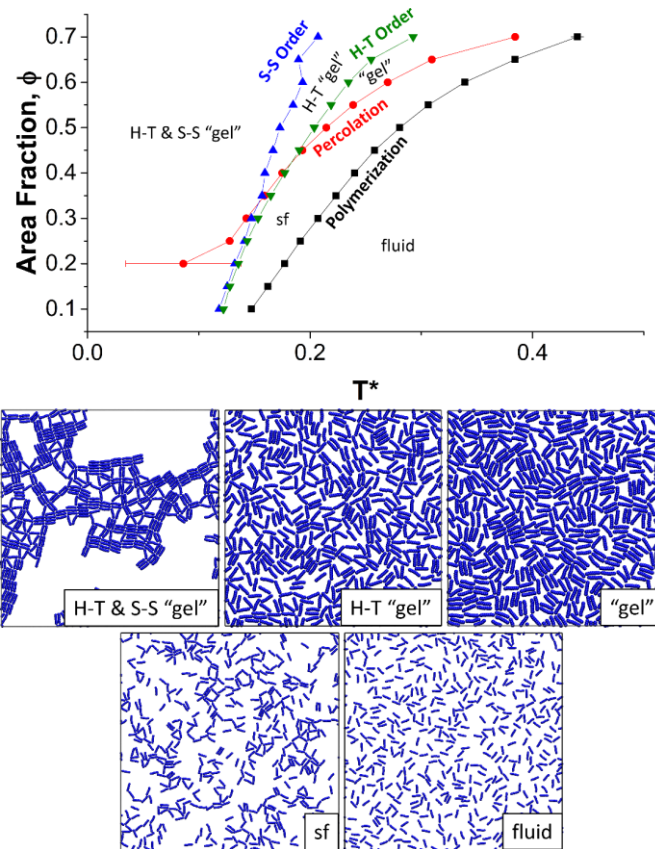


Figure 2.8. Phase diagram of dipolar rods with 3.0 charge separation plotted in the area fraction vs temperature plane. Fluid, string-fluid, S-S "gel" and H-T and S-S "gel" are present.

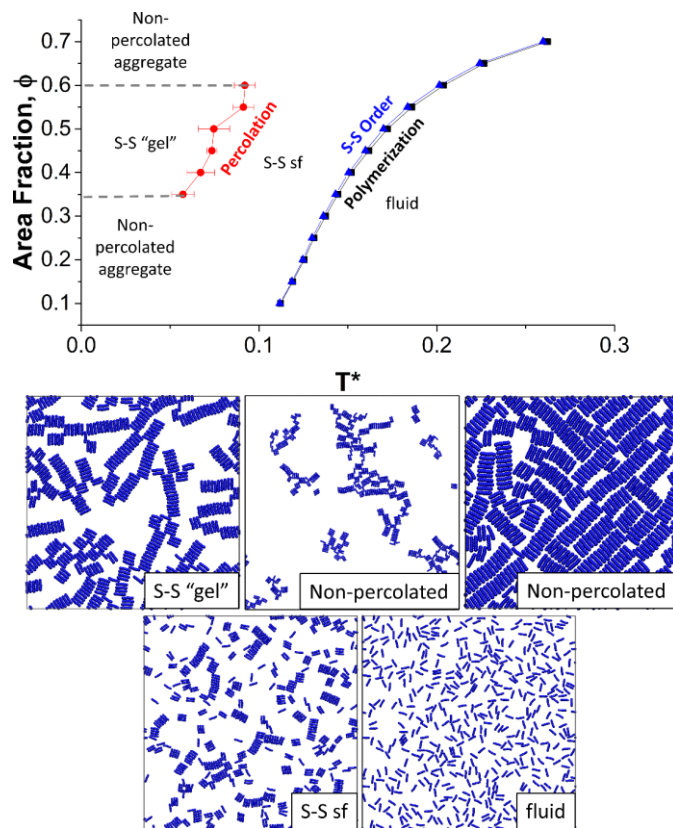


Figure 2.9. Phase diagram of dipolar rods with charge separation 2.5 plotted in the area fraction vs temperature plane. Fluid, S-S string-fluid, and S-S “gel” are present. There is no H-T transition for this system; the rods always line up in S-S fashion.

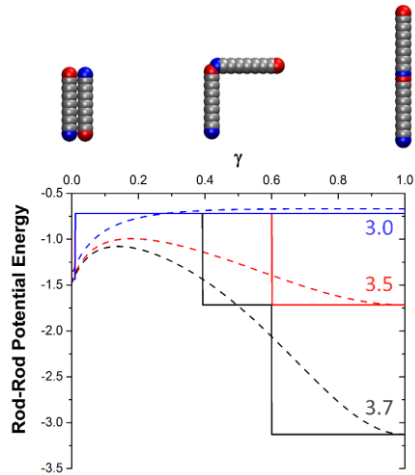


Figure 2.10. The rod-rod potential energy vs. “joint” angle curves for the Yukawa potential (dashed lines) and our discontinuous potential (solid lines). The three-step discontinuous potential used in our simulations was derived by matching the rod-rod potential energy calculated for the continuous Yukawa potential with that for the discontinuous potential. Black, red and blue lines are for charge separation 3.7, 3.5 and 3.0, respectively.

Appendix 2-1 Discontinuous Potential Development

We designed the discontinuous charge-charge potential to mimic the Yukawa potential by matching the discontinuous and continuous total potential between a pair of dipolar rods, the “rod-rod potential”, over a variety of configurations. The rod-rod potential is the sum of the four interactions between the positive and negative charges on a pair of rods, not counting interactions between charges on the same rod. We investigated the rod-rod continuous potential as a function of the angle between two adjacent rods, the so called “joint” angle, γ , as described by Alvarez et al. ²⁷. This angle is defined as $\gamma = \theta/\pi$, where θ is the angle between the two rods i.e. the rods are in a side-by-side alignment when $\gamma = 1$ and are in head-tail alignment when $\gamma = 0$ as shown at the top of Figure 2.10. Figure 2.10 displays the rod-rod continuous potential versus γ as dashed lines for charge separations of 3.0 (blue), 3.5 (red), and 3.7 (black). The corresponding rod-rod discontinuous potentials are shown in solid lines and were calculated using the continuous potential given in Equation 1 of the main text. In order to capture both head-tail and side-side tendencies it was essential that the rod-rod discontinuous potential be a good approximation to the rod-rod continuous potential at charge separations both above and below the dashed line in Figure 2.2. The goal, therefore, was to develop a discontinuous rod-rod potential which matched the continuous one at extreme values of γ to give correct energies for head-to-tail and side-by-side arrangements of the dipoles.

We chose the locations for the discontinuities in our discontinuous charge-charge potential using the following approach. For a charge separation of 3.7 we wanted a discontinuity in the discontinuous rod-rod potential at $\gamma = 0.6$ because this is approximately

the angle at which an inflection point occurs for the continuous rod-rod potential as seen in Figure 2.10. This required a discontinuity in the charge-charge potential at a reduced charge-charge distance of 0.595. Similarly, at a charge separation of 3.5 we needed a discontinuity at $\gamma = 0.6$ which required a discontinuity in the charge-charge potential at a reduced charge distance of 0.433. In addition to creating a discontinuity in the rod-rod potential for a charge separation of 3.5 this generated a discontinuity in the rod-rod potential for charge separation 3.7 at a γ of approximately 0.4. Our final discontinuity was chosen to match the rod-rod potential for all three charge separations at $\gamma = 0$. We arbitrarily chose a reduced charge-charge distance of 1.1 for this discontinuity in order to hold the rods “tightly” in a side-side configuration and this generated a discontinuity in the rod-rod potential at small γ values. This defines the three discontinuities used in our model charge-charge potential.

We chose the depths (heights) of the square well (square shoulder) charge-charge potential using the following approach. We forced the depth of the innermost well in our charge-charge potential to take a value of -3.129, the value of the continuous rod-rod potential at $\gamma = 1$ for charge separation 3.7 as shown by the black dashed line in Figure 2.10. Similarly, we set the depth of the middle well for the charge-charge potential to be -1.717 so that the discontinuous rod-rod potential would match the continuous potential at $\gamma = 1$ for charge separation 3.5. We set the depth of the outermost well to be -0.719, half the value of the average rod-rod continuous potential at $\gamma = 0$, since there are two charge pairs within this distance, in order to match to the continuous rod-rod potential for the three charge separations at $\gamma = 0$. This completes the definition of the charge-charge discontinuous potential used in our simulations.

CHAPTER 3

Formation of Limit-periodic Structures by Double-dipole Particles Confined to a Triangular Lattice

Chapter 3 is essentially a manuscript by David M. Rutkowski, Catherine Marcoux, Joshua E. S. Socolar and Carol K. Hall submitted to Physical Review E.

Formation of Limit-periodic Structures by Double-dipole Particles Confined to a Triangular Lattice

David M Rutkowski^a, Catherine Marcoux^b, Joshua E. S. Socolar^b and Carol K. Hall^{a*}

^aDepartment of Chemical and Biomolecular Engineering, North Carolina State University, 911 Partners Way, Raleigh, North Carolina 27695, USA

^bPhysics Department, Duke University, Durham, North Carolina 27708, USA

Abstract

We have performed Monte Carlo (MC) simulations on two-dimensional systems of double dipole particles confined to a triangular lattice in order to determine conditions that permit the formation of a limit-periodic phase. We have found that limit-periodic structures form only when the rotations of the particles are confined to a set of six orientations aligned with the lattice directions. Related structures form when $\pi/6$ rotations or continuous rotations are allowed. Order parameters signaling the formation of the limit-periodic structure and related structures are measured as a function of temperature. Our findings on the formation of the limit-periodic structure elucidate features relevant to the experimental creation of such a structure, which is expected to have interesting vibrational and electromagnetic modes.

3.1 Introduction

Nonperiodic structures with long range order are of interest both theoretically and experimentally due to their novel (expected or observed) electronic, photonic, elastic and frictional properties ¹. Since the discovery of quasicrystals in the 1980's the definition of the term "crystal" has changed to include nonperiodic structures, and now refers to any structures with sharp diffraction peaks indicating long-ranged translational order ². The possibility of having equilibrium phases exhibiting perfect translational order without the regular, periodic repetition of a unit cell is now well established ².

Quasicrystals are non-periodic structures that have point group symmetries that are incompatible with periodicity, meaning they have diffraction patterns indicating symmetries not found in crystals (e.g. 8, 10, or 12-fold rotational symmetry in 2D or icosahedral symmetry in 3D). The earliest examples of quasicrystals were metallic made from binary or ternary metals typically involving the element aluminum ³ More recently nonmetallic quasicrystals have been created with liquid crystals ⁴, ABC-star polymers ⁵, colloidal disks ⁶ and inorganic nanodisks ^{7,8}. Metallic quasicrystals have been found or envisioned for use as non-stick heat insulation replacing Teflon, mechanical reinforcement, corrosion resistant surfaces and as hydrogen storage materials ⁹ while nonmetallic quasicrystals are expected to be useful in photonic applications ¹⁰.

Limit-periodic structures, like quasicrystals, are homogeneous, nonperiodic structures with long range order; however, unlike quasicrystals they are composed of interleaved periodic structures with ever-increasing lattice constants. Each periodic subset of the limit-periodic structure is referred to as a "level". The structure with the smallest lattice constant is

level-1, the structure with the next largest lattice constant is level-2, and so on. An example of a limit-periodic structure can be seen in the work by Byington and Socolar in which kagome lattices of increasing size overlap to form a single limit-periodic structure ¹. Such structures have been shown to be ground states of systems with physically plausible Hamiltonians and have been observed to form through a sequence of phase transitions in simulations of slow cooling from a random initial state in several models ^{1, 11, 12}. To date, however, no experimental realization of an equilibrium or self-assembled limit-periodic structure has been reported.

The simplest demonstrations of the possibility of limit-periodic ground states are framed in the language of tiling theory. It has been shown that limit-periodic structures are the only space-filling, non-overlapping arrangements of certain types of tiles endowed with appropriate matching rules for the relative orientations of adjacent tiles. Each type of tile in a given aperiodic set is called a prototile and may be characterized by its shape alone or by decorations that specify its type and orientation. Prototiles that force limit-periodic tilings have been constructed by Berger ¹³, Robinson ¹⁴, Goodman-Strauss ¹⁵, and by Socolar and Taylor ^{1, 16}. The latter is of particular interest because only a single prototile (and its symmetry-related partners) is required.

Remarkably, as has recently been shown, strict matching rules specifying limit-periodicity are not required for the formation of limit-periodic structures. Marcoux et al. found that a simplified version of the model investigated by Socolar and Taylor can lead to a limit-periodic structure upon slow reduction of the temperature even though it has a periodic ground state ¹¹. The simplification is called the “black stripe model” and consists of a

hexagonal prototile with lines decorating its surface to indicate which neighboring orientations are favored (Figure 3.1a). If the black segments on two tiles sharing an edge are continuous across that edge, the interaction energy is taken to be zero, while a positive energy is assigned to edges where the black lines do not meet. The black-stripe decoration of the hexagonal prototile, along with the energy penalties described above, turns out to induce the formation of a limit-periodic structure even though there exist degenerate ground states that are periodic.

The model considered in this paper, shown in Figure 3.1b and termed the “double-dipole disk model,” mimics some of the crucial features of the black-stripe model. In this image, red circles represent positive charges while blue circle represent negative charges. There is a repulsive interaction (and therefore an energy penalty) when charges of like sign are near each other, while there is an attractive interaction when charges of unlike sign are near each other. These charges act to mimic the matching rules for the short segments near the top and bottom of the black stripe prototile. A key difference between the present model and the black-stripe model, however, is that the long stripe linking opposite edges of the hexagonal prototile, which is offset from the tile center, is not represented at all by the charge distribution; in this sense our model is a simplification of the black-stripe model, and formation of a limit-periodic phase in our model demonstrates a greater degree of robustness of the limit-periodic phase than previously reported.

Double dipolar disks could potentially be created from anisotropic colloidal particles. For example, colloidal particles with a small metallic patch on their surface have been shown to have quadrupolar interactions under the influence of an external electric field at high

frequency¹⁷⁻¹⁹. These particles served as branching points in a mixture of dipolar and quadrupolar colloids. Additionally, colloids embedded in a nematic liquid crystal have been found to have quadrupole-like interactions allowing them to form square lattices. These particles were shown to be at least metastable in a hexagonal close packed array after moving them via laser tweezers²⁰.

The objective of this work is to systematically investigate the propensity for systems of “double-dipole” disks to form a 2d limit-periodic structure. We perform Monte Carlo simulations to identify equilibrium phases at different temperatures of a set of models in which two parameters are varied: (1) the distance, δ , of the embedded charges from the center of each disk; and (2) the set of possible orientations of any given disk. In all cases, the disks are assumed to be pinned to the sites of a triangular lattice. We consider three sets of possible orientations of a given disk. (Note that rotation by π leaves the disk invariant.) In the set R3, the disk may adopt any of the three distinct orientations related by rotation by $\pi/3$. In the set R6, the disk may adopt any of the six orientations related by rotation by $\pi/6$. And in the set R_∞ , the disk may rotate continuously.

Highlights of our results include the following. The only rotational move set for which the limit-periodic structure forms is R3. Specifically, we have observed ordering of the first four levels through a sequence of transitions as we slowly lower the temperature of the system. The transitions occur at the same scaled temperature, T_n/E_n , where E_n is the interaction energy of a single disk with all the disks in the same level, n , up to the cutoff in the potential. Simulations using R_∞ form level-1 at large values of δ , but are unable to form level-2. Instead the disks that are not part of level-1 (termed “rattlers”) all align along a

single direction as the temperature is further lowered. Simulations using R_∞ at small values of δ are dominated by the formation of a “striped phase” in which the disks in a given stripe all have the same orientation, with that orientation alternating on successive stripes between being along the stripe and perpendicular to it. The simulations using R6 form level-1 order with rattlers aligning in the striped phase at high values of δ ; at low values of δ the entire system forms the striped phase.

3.2 Methods

An individual disk in our simulations has diameter σ and is decorated with four point charges of alternating sign at identical distances, δ , from the center of the disk as shown in Figure 3.2. With the disk in an orientation specified by an angle α , negative charges are placed at positions $\pm\delta[\sin(\alpha - \pi/6), \cos(\alpha - \pi/6)]$, and positive charges at $\pm\delta[\sin(\alpha + \pi/6), \cos(\alpha + \pi/6)]$ where the numbers inside the square brackets refer to the x- and y- coordinates of the charges in a body centered reference frame respectively. The disk in Figure 3.2 is shown in the reference configuration $\alpha = \pi/3$. The angles constructed by a pair of neighboring charges and the center of the disk therefore remain fixed and are equal to $\theta = \pi/3$ for the two closer neighboring pairs or equal to $\phi = 2\pi/3$ for the two further neighboring pairs. The back face of our particle has a reverse “chirality” to the one shown in Figure 3.1b, but we restrict our simulations to 2d, not allowing disks to flip over and thus ensuring that all retain the same single chirality at all times. Additionally of note is that the net charge and net dipole moment of the disk are both zero. The centers of the disks

are taken to be fixed at the positions of a triangular lattice with one basis vector lying in the horizontal direction; translations of the disks are not allowed.

We perform Monte Carlo (MC) simulations for various values of δ and choices of the rotational move set allowed for each individual disk. We study values of δ ranging from 0.05σ to 0.45σ in increments of 0.05σ . A move in our MC simulation consists of a rotation about the center of an individual disk. Three move sets are investigated: (R ∞) continuous rotation, (R6) rotation in $\pi/6$ increments; i.e. $\alpha = n\pi/6$ for all integers n , and (R3) rotation in $\pi/3$ increments; i.e. $\alpha = n\pi/3$. The interaction between the charges on separate disks is modeled by an attractive Yukawa potential for charges of unlike sign and a repulsive Yukawa potential of the same magnitude for charges of like sign:

$$U(r^*) = -\varepsilon q_1 q_2 / r^* \exp(-\kappa^* r^*) \quad (1)$$

In this equation, ε is a constant with units of energy per charge squared, q_1 and q_2 are the two interacting charges, $r^* = r/\sigma$ where r is the separation distance between the charges, and $\kappa^* = \kappa/\sigma$ where κ is the inverse Debye length. The majority of our simulations use $\kappa^* = 1.194$ and $\varepsilon = 0.113$, which yields $U(r^*) = -1.0$ at $r^* = 0.1$ and $U(r^*) = -10^{-6}$ at $r^* = 8.0$. All interaction energies between charges are included up to a cutoff distance $r^* = 8.1$. We refer to this potential as P_1 . P_1 is representative of a particle of size $\sigma = 0.36$ μm in a solution with a salt concentration of 10^{-6} M. We also perform simulations on a shorter range interaction potential with $\kappa^* = 5.695$, $\varepsilon = 0.177$ and a cutoff at $r^* = 2.1$; we refer to this potential as P_2 . P_2 is representative of a particle of size $\sigma = 1.73$ μm in a solution with a salt concentration of 10^{-6} M. The centers of the disks in our simulations are

constrained to lie on a triangular lattice, thus the only degree of freedom for a given disk is its orientation α .

We base our potential energy cutoff on the distance between disk centers. All charges on a pair of disks are included (or omitted) in potential energy calculations if the centers of the disk pair are within (or outside) a certain cutoff. The nearest neighbor distance between disk centers of the same level is $2^{\omega-1}\sigma$ where ω is the level number, meaning that level-4 disks have a minimum distance of 8σ between them. The cutoff at 8.1σ thus includes interactions between the disks that are nearest neighbors in the level-4 structure. If the range of the potential is applied to pairs of individual charges rather than the clusters comprising complete disks, we find that a larger cutoff distance is required for observation of the level-4 structure. The longer cutoff avoids artifacts associated with inclusion of unbalanced charges at the boundary of the cutoff region.

Our simulations are performed in a rectangular simulation box with periodic boundary conditions in both the x and y directions. The width and length of the simulation box were chosen to accommodate a triangular lattice with lattice constant σ with periodic boundary conditions. The triangular lattice contains a specified number of rows with each row having the same number of lattice points as there are rows in the system. We refer to the size of these lattices and therefore the system size as $n \times n$ where n is the number of rows in a lattice or equivalently the number of lattice points in a single row. The two system sizes investigated were 64×64 and 32×32 . The larger system is the same system size as that investigated by Byington et al. and Marcoux et al. and allows for up to level-4 order to be formed^{1, 11}. We use the larger system size for all the discrete rotation simulations (R6 and

R3) as well as for a single continuous rotation simulation (R_∞) at a δ value of 0.35. The smaller system size is used for the majority of the continuous rotation simulations since they take considerably longer to perform than the discrete cases. This is because the infinite number of possible disk orientations precludes the use of a potential lookup table (explained below). We simulated 3×10^4 MC cycles at each temperature step for the R3 case, 6×10^4 MC cycles for the R6 case and, 12×10^4 cycles for the R_∞ case. A single cycle consists of 64^2 (the number of disks in the large systems) individual rotational moves. We greatly sped up our discrete rotation simulations by constructing lookup tables for the potential between pairs of disks located at the discrete set of possible relative positions and orientations. Without the speedup afforded by this method it would be computationally difficult to simulate diverse sets of parameters in a reasonable amount of time. For the continuous case, where no lookup table was used, it took approximately 2.94 hours to simulate 10^4 cycles (where one cycle includes an attempted rotational move for each particle in the system) running on nine CPU threads using OpenMP. For the R3 case, where a lookup table was used for the same size system, the same number of cycles took approximately 3.27 minutes running on a single CPU thread.

We chose to use simulated annealing to observe the formation of successive levels of limit-periodic structures. The temperature of the system was lowered in discrete steps, allowing time for equilibration at each step²¹. If a limit-periodic phase is to emerge, increasing levels of order are expected to form as the temperature is lowered. The level-1 lattice will form at a temperature at which the rest of the disks remain free to rotate; these freely rotating disks are referred to as “rattlers”. At a lower temperature the level-2 lattice

will form. The transitions can occur for a given level ω as long as the cutoff distance for the potential exceeds $2^{\omega-1}\sigma$.

To measure the degree of order for an individual level of the limit-periodic structure, we introduce the order parameter ϕ_n from Byington et al. In calculating ϕ_n , the system is first divided into four sublattices (A, B, C and D) as in Figure 3.3a. The so called “staggered tetrahedral spin” vector, $\sigma_{n,j} = e_X$, for each disk j in the system must be measured where n is the level and e_X is a unit vector pointing towards an individual vertex, $X \in \{A_{tet}, B_{tet}, C_{tet}, D_{tet}\}$, of a 3d reference tetrahedron as in Figure 3.3b. $\sigma_{n,j}$ is calculated based on a disk’s orientation (which can be either at a rotation angle of $0, \pi/3$ clockwise or $-\pi/3$ clockwise) and the identity of the sublattice, j , on which it sits according to the diagram in Figure 3.3b. For example, a disk sitting on the D sublattice and oriented to the left would be assigned $\sigma_{n,j} = e_A$. The average total spin is defined as $\sigma_{n,tot} = 1/N \sum_j \sigma_{n,j}$, where N is the total number of disks in the system and the sum is over the whole system. ϕ_n is defined in a way that accounts for the four ways in which an individual level can order, specifically $\phi_n = \max[e_X \cdot \sigma_{n,tot}]$ where e_X runs over all four unit vectors in the reference tetrahedron in Figure 3.3. ϕ_n is equal to 1.0 if three of the sublattices have orientations consistent with the level of the limit-periodic structure, regardless of the orientation of the fourth sublattice. This order parameter can be used to characterize successive levels of the limit-periodic structure since the particles on the unordered sublattice (the rattlers) after the system forms a given level n are also in a triangular lattice arrangement which has the ability to form level $n+1$.

After level $n+1$ forms, ϕ_{n+1} can be calculated by considering only the particles that were rattlers in level n . This order parameter can be used directly for R3 simulations, but not for R^∞ or R6 simulations since ϕ_n is not defined when the orientation of the particle is at values other than $n\pi/3$. For these simulations, the orientation angle is rounded to the nearest value of $n\pi/3$ and then ϕ_n is calculated. When the angle is a multiple of $\pi/6$ but not of $\pi/3$ (which occurs often in the R6 simulations) we randomly choose the orientation angle to be either of the two angles it is halfway between.

We define an additional order parameter for the striped phase that we observe in our R^∞ and R6 simulations. The striped phase can either apply to all of the disks in the system as in Figure 3.4a or in the first image in Figure 3.5, or just to the rattlers as in the second image in Figure 3.5. A staggered octahedral spin vector, $\sigma_{n,j} = e_K$, for each disk j in the system must be measured where n is the level and e_K is a unit vector pointing towards an individual vertex, K , of a 3d reference octahedron as in Figure 3.4b and can therefore be indicated by a unit vector along one of the three Cartesian axes in 3d. $\sigma_{n,j}$ is calculated based on a disk's orientation (which can be at a rotation angle of $n\pi/6$) and the identity of the sublattice, j , on which it sits according to the diagram in Figure 3.4b. For example, a disk sitting on the D sublattice with an orientation of $\alpha = 5\pi/6$ would be assigned $\sigma_{n,j} = e_Y$. The average total spin is again defined as $\sigma_{n,tot} = 1/N \sum_j \sigma_{n,j}$, where N is the total number of disks in the system and the sum is over the whole system. The final order parameter, ψ_n , is defined in a way that accounts for the six ways in which an individual level can order, specifically

$\psi_n = \max[e_K \cdot \sigma_{n,tot}]$ where e_K runs over all six unit vectors in the reference octahedron in Figure 3.4b.

A third order parameter is used to measure the occurrence of a nematic-like phase in which the disks not forming the level-1 structure (the rattlers) all align in the same direction as shown in the two figures on the right of Figure 3.5. The order parameter for these aligned disks is taken as the 2d nematic order parameter where the global director is determined by the eigenvector associated with the largest eigenvalue of the Q-tensor. The Q-tensor in 2d is defined to be $\frac{1}{N} \sum_{i=0}^N 2\hat{u}_{i\alpha}\hat{u}_{i\beta} - \delta_{\alpha\beta}$ where \hat{u}_i is a unit vector which points in the direction of the disk, $\delta_{\alpha\beta}$ is the Kronecker delta, N is the number of disks in the system and α and β run over both x and y components²². The largest eigenvalue is the value of the 2d nematic order parameter.

3.3 Results and Discussion

One interesting aspect of our model is that the potential energy of a single rattler interacting with its nearest neighbors in the level-1 ordered pattern is independent of the orientation of the rattler. This can be shown by first investigating a single rattler with its six nearest neighbors (which form the level-1 structure around the rattler) as in Figure 3.6. The potential energy of this rattler with respect to its nearest neighbors is zero because the distances between the charges on the rattler and the charges on neighboring disks multiplied by the sign of the interaction, i.e. $\text{sgn}[U(r_{ij})]*r_{ij}$, cancel out pairwise. There are up to 24

unique pairs of these distances for the rattler; four of the distances which cancel out are shown in Figure 3.6 (left) where dashed lines of the same color represent equal distances. These distances are equal because, using the indexing in Figure 3.6, the charged bead 0 on disk 6 and the entirety of disk 0 can be transformed into charged bead 1 on disk 6 and the entire disk 1 by a counter-clockwise rigid rotation of $\pi/3$ about the center of disk 6. Since this is a rigid rotation, the distances between the charges on the rattler and the surrounding disks are maintained. The sign of charges 0 and 1 on the rattler are opposite, which results in an exact cancelation of these contributions to the energy. The other 20 pairs of signed distances arise from a similar analysis for each disk surrounding the rattler and for charges 2 and 3 on the opposite side of the rattler. This same analysis can be extended to the entire level-1 structure which has formed surrounding the rattler. That is, the whole system can be rotated about the center of an individual rattler by an increment of $\pi/3$ and all levels of a lower index than the rattler will be indistinguishable from their pre-rotated state. We have also measured the potential energy between disks of different levels in the limit-periodic structure formed during our simulations and have found it to be less than 10^{-16} .

Since the individual levels of the limit-periodic structure do not interact with each other for our model, it can be helpful to define a scaled δ for predicting how rattlers created during a transition will order upon further decrease in the temperature. The disks in level ω are separated by a distance $2^{\omega-1}\sigma$. For example, the distance between disks in level-3 is 4σ . All distances associated with a group of disks in the same level can be rescaled by dividing by this distance. In the absence of screening, this results in a rescaled value for delta:

$$\delta_{eff} = \delta / 2^{\omega-1} \quad (2)$$

δ_{eff} can be used to predict and explain the structure that a given level will form. The rattlers are effectively isolated from the disks in lower levels of the limit-periodic structure. This means that the rattlers should act as an effective system identical to the original one but with $\delta = \delta_{eff}$. The limit-periodic structure will form if and only if the level-1 structure forms for arbitrarily small δ . If the level-1 ordering requires δ above some threshold, δ_c , then the remaining rattlers at sufficiently high levels for which $\delta_{eff} < \delta_c$ will not undergo the required transition and a complete limit-periodic structure will not form.

We begin by describing our results for the simulations using the R_∞ moveset, i.e. continuous rotations). The majority of these simulations were performed using a simulation box containing 32 x 32 disks using potential P_2 , however we performed one continuous rotation simulation containing 64 x 64 disks using potential P_1 at a δ of 0.35 to ensure that finite size effects were negligible. Each rotational move lies in the range of $[0, \pi]$ with a uniform probability, allowing the disk to adopt any possible orientation in each move. The continuous rotation simulations result in a striped phase at values of $\delta \leq 0.20$ as in the leftmost image of Figure 3.5. The striped order parameter ψ_1 for this transition versus $\log(T^*)$ is shown below in Figure 3.7a. These curves appear to have two distinct regions: one in which the transition is shaped like a tanh function and one in which it is linear before plateauing to a value of 1.0 at low T^* . At values of δ between 0.25 and 0.35 the system forms a unidirectional rattler phase of the type shown in the third image in Figure 3.5. The order parameters for the systems in this range are shown in Figure 3.7b where ϕ_1 is indicated by the

solid symbols and lines, and the nematic order parameter of the rattlers is indicated by the open symbols and dashed lines. The orientation of the rattlers in this phase is an integer multiple of $\pi/3$ (i.e. the rattler is parallel to one of the three disk types composing the limit-periodic structure) and so we further specify this phase as a unidirectional α -rattler phase. We display $\delta = 0.25$ on both plots in Figure 3.7 because at low temperatures it has relatively high values of both ϕ_1 and ψ_1 , which we take to mean that this system is a mixed state between the striped phase and the α -rattler phase. This is possible because the transformation of a striped phase to a unidirectional α -rattler phase can be achieved by alternating clockwise and counterclockwise rotations by $\pi/6$ of the disks in the parallel stripe. This rotation angle can be less than $\pi/6$, leading to a mixed phase. The amount of mixing between the two phases decreases as the value of δ increases and the structure becomes more like an ideal unidirectional α -rattler phase. ψ_1 for $\delta = 0.25$ also plateaus to a value around 0.5 at intermediate temperatures and then achieves a relatively high value at lower temperatures suggesting that this temperature is close to the transition between the striped and α -rattler phase. At $\delta \geq 0.40$ the system forms a structure similar to the α -rattler phase except the orientation of the rattlers is $\alpha \in \{\pi/6, \pi/2, 5\pi/6\}$ and so we call this phase the unidirectional β -rattler phase as shown in the rightmost image in Figure 3.5. Interestingly, the sequence of transitions as a function of T^* is reversed for the two order parameters; as the value of δ increases the ϕ_1 transition occurs at increasingly higher temperatures and the nematic transition at increasingly lower temperatures. This is likely due to the fact that as δ increases,

the level-1 structure becomes more energetically stable and therefore it becomes more difficult to distort the level-1 structure to form a unidirectional rattler phase.

The failure of the simulations using R_∞ to form level-2 of the limit-periodic structure appears to be due to a distortion in the level-1 structure. This distortion occurs when the disks occupying two of the three sublattices making up the level-1 structure rotate slightly away from an integer multiple of $\alpha = \pi/3$ and their ideal position in a limit-periodic structure. The disks on both the distorted sublattices rotate off their limit-periodic orientation by the same value with one rotating clockwise and the other counter-clockwise. In order to define the distorted sublattices we focus on the level-1 “cage” surrounding a single rattler as in Figure 3.6 (right). In this “cage” there are two pairs of neighboring disks that are distorted. We refer to the sublattice containing the disk in one of these pairs which is located counterclockwise from its neighboring distorted disk as D_1 and the other sublattice containing the disk located clockwise from its neighboring distorted disk as D_2 . For the α -rattler case, the disks on D_1 are rotated clockwise while the disks on D_2 are rotated counter-clockwise as can be seen in the right top image in Figure 3.6. For the β -rattler case, the reverse is true; the disks on D_1 are rotated counter-clockwise while the disks on D_2 are rotated clockwise as can be seen in the right bottom image in Figure 3.6. The exact value of the distortion depends on both the potential and the value of δ with the distortion angle decreasing as δ increases. These distortions cause the level-2 rattler to have a preferred orientation. In the α -rattler phase the preferred orientation of the rattler is $\alpha = \alpha_{D_3}$ where α_{D_3} is the orientation of the disks

occupying the non-distorted sublattice of the level-1 structure. For the β -rattler phase $\alpha = \alpha_{D_3} + \pi / 2$. All of the level-2 rattlers attain the same orientation at low temperature.

Next we describe the results from simulations using the R6 moveset, i.e. $\pi/6$ rotation simulations. In these simulations, as in the simulations using R_∞ , a striped phase is present at values of δ less than or equal to 0.25. A plot of the striped order parameter, ψ_1 , versus temperature for values of $\delta \leq 0.25$ is shown in Figure 3.8. All curves show a sharp transition except for the curve at $\delta = 0.25$ which slightly plateaus to a value of 0.5 before it attains a value of 1.0. This system forms a mixed state of level-1 structure and striped phase at around a temperature of 0.01, but upon further lowering of the temperature, the system adopts a purely striped phase configuration. For $\delta \geq 0.30$, the system forms the level-1 structure with rattlers forming a striped phase instead of the level-2 structure. For this case, we first calculate ϕ_1 (to identify which sublattice is the rattler sublattice) and then calculate ψ_2 as shown in Figure 3.9. For one of our replicates at $\delta = 0.30$ we observe a single system-spanning stripe form while the rest of the system forms the striped rattler phase leading to the large error bars seen for this curve. The rattlers for these simulations do not align in the same fashion as in the continuous rotation simulations due to the fact that in these simulations the level-1 structure cannot distort. Instead the rattlers form a striped phase, as their δ_{eff} is always less than 0.25.

Finally, we describe our results from simulations using the R3 moveset, i.e. $\pi/3$ rotation simulations. For these simulations we found that regardless of the value of δ , the limit-periodic structure forms up to level-4 as shown in the left image of Figure 3.10. The

right image in Figure 3.10 shows plots of ϕ_n vs. $\log(T^*)$ for all four of these levels at a single δ of 0.35. The curves are similar to each other except for their transition temperatures and the value of the order parameter at high temperatures which increases with increasing level of order. The dependence of the value of the order parameter at high temperatures on the level appears to be due to a system size effect caused by the number of disks in a given level decreasing as the level increases. We confirm that this split is due to a system size effect by calculating the expected average order parameter at infinite temperature as a function of system size. To do this we randomly select rotations for n disks (as long as n a multiple of four) from the R3 moveset. Randomly selecting the rotations is equivalent to simulating a system at infinite temperature since there are no interactions between the disks. We then calculate ϕ_1 for this imaginary system as a function of the number of disks in the system, N , and fit it to the power law $\phi_1(N) = 1.0175N^{-0.507}$. The value of ϕ_n for each of the four curves in Figure 3.10 at the highest \tilde{T} simulated, \tilde{T}_n , is consistent with the values calculated with this function such that $\phi_n(\tilde{T}_n) = 75 \left(64^2 (1/4)^{n-1} \right)^{-0.507}$ where n is the level under consideration. Since the levels do not interact with each other, the curves should collapse if the temperature is divided by the total potential energy for a single disk interacting with other disks in the same level, $U_{a,i-a}$, where a is the level of a single disk, i , interacting with other disks in the same level. We refer to this scaled temperature as \tilde{T}_{i-a} and we plot the order parameters for every δ investigated versus \tilde{T}_{i-a} in Figure 3.11. Scaling the temperature in this manner causes ϕ_n to collapse into four separate curves as a function of \tilde{T}_{i-a} , corresponding

to the four levels observed in our simulations of the limit-periodic structure. These curves have similar scaled transition temperatures and merge into a single curve at \tilde{t} values lower than the transition temperature. These curves seem to be associated with continuous phase transitions as they do not have any evidence of hysteresis with temperature. We plot a state diagram showing the different phases formed at the lowest temperatures investigated on a moveset versus δ plane in Figure 3.12.

We have performed exploratory simulations in which we vary θ in our double-dipole model to be either $2\pi/3$, $\pi/2$ or $\pi/18$. Motivation for this comes from the observation that the location of the point charges does not matter in ensuring the potential energy of the rattler is zero with respect to the surrounding disks. This suggests that other values of θ could also lead to a limit-periodic structure. However, it is not clear if the individual levels of the limit-periodic structure would form for systems with θ other than $\pi/3$. Remarkably, all three systems tested ($\theta = 2\pi/3, \pi/2, \pi/18$) form up to level-4 order through a series of phase transitions similar to the case when $\theta = \pi/3$. Level-4 for each of these systems can be seen in Figure 3.13. This suggests that θ does not influence whether the system forms the limit-periodic structure. Since δ also does not affect whether the system forms a limit-periodic structure, it may even be possible to form a limit-periodic structure from dipolar disks with an embedded point quadrupole. Even more complex particles may also form the limit-periodic structure since the number of charges on the surrounding six disks also does not matter in ensuring there is no interaction between the levels as long as the number of positive and negative charges on a single disk are equal.

3.4 Discussion and Conclusions

We have determined that our double-dipole disk model can form a limit-periodic structure if the rotational moves are limited to $\pi/3$ increments (R3) but not if the rotation moves are either continuous (R_∞) or limited to $\pi/6$ increments (R6). Instead the simulations using the R6 moveset form either a striped phase or a striped rattler phase, while continuous rotation simulations form either the striped phase or a unidirectional rattler phase of one of two types. The limit-periodic structure that forms using R3 does not depend on the value of δ or θ and so a wide range of possible particles could be used to create such a structure.

By restricting our simulations to two dimensions (as opposed to confining freely-rotating particles to a plane), the disks adopt a single chirality. The importance of a single chirality for the formation of the limit-periodic structure can be illustrated by an experimental model which is visually very similar to ours that was mentioned briefly by Chen et al. in which four attractive patches were placed on a disk in the same locations as in our model²³. Instead of forming a limit-periodic structure, these particles were expected to form a Kagome lattice structure. Indeed, in exploratory simulations in quasi-2d, which allows for both chiral states to be interchangeable, we found phases that are consistent with triblock Janus disks including Kagome lattices and hexagonal close packed systems, but not limit-periodic structures. It is only by limiting our system to a single chirality, i.e. by constraining our disks to a 2d plane and disallowing rotation out of plane, that we see the formation of limit-periodic-like order.

The double-dipole disk model differs from the closely related tiling model of Marcoux et al. in two respects. First, the tiling model explicitly includes only nearest

neighbor interactions between tiles, while the double-dipole disk model includes interactions between all pairs of disks within the cutoff range. While the formation of higher level structures in the tiling model occurs through effective long range interactions mediated by chains of direct nearest neighbor interactions, the ordering of rattlers in the double-dipole disk model relies on direct interactions between disks separated by distances corresponding to the lattice constants of the higher level lattices. Second, our model naturally allows for investigation of the effects of continuous rotations. Continuous rotations in both lattice and off lattice simulations have been investigated previously using a model similar to the black stripe model in which six point dipoles are embedded within a sphere. Limit-periodic structure transitions were observed with that model ¹².

The question arises as to whether or not our model, which forms the limit-periodic structures when the rotations are limited to the R3 moveset and disks are monodisperse can be realized experimentally. Limiting rotation to $\pi/3$ could be achieved by making the particles regular hexagons instead of disks. Rotating hexagons would likely be difficult, however, so instead a shape somewhere in between a hexagon and a circle might be required. Since the symmetry in the disks and their placement is required for the potential to cancel out, and this canceling out seems important for the formation of the limit-periodic structure, it may be difficult to form such a structure experimentally using the model we have presented in this paper. Slight differences in the disks or holes in the lattice could disrupt the formation of the limit-periodic structure since the interaction energies between disks falls off rapidly as the level increases. One way to form a triangular lattice is to make a Wigner crystal, which results when isotropically repulsive particles are confined to a small volume or area ¹². This

could be achieved with the model used in this paper by adding a charge to the center of each disk and restricting the area of the system to a certain size. Enforcing a single chirality could be dealt with by modifying the model so that vertically oriented dipoles are substituted for the individual charges (vertically up (normal to the plane of the disk) for positive charges and vertically down for negative charges). For such an arrangement, the particle would have the same chirality even if it was flipped over in three dimensions ¹².

The novel aspects of our work include the following. Our limit-periodic structure appears to be unique compared to those observed in earlier work since it forms in part due to the isolation of the individual levels from each other. Additionally, unlike prior tile models which considered potentials including up to next nearest neighbors ¹ or nearest neighbors ¹¹ our simulations consider intermediate-ranged potentials similar to work done recently with point dipoles ¹². Our simulations have also found competing structures not reported before in simulations of limit-periodic structures including the striped phases and the α - and β -unidirectional rattler phases. While these represent failures of the limit-periodic structure to form they are interesting in their own right. Finally, our model is a simplification of previous models, in particular the black-stripe model, and formation of a limit-periodic phase using our model demonstrates a greater degree of robustness of the limit-periodic phase than previously reported and adds to the number of models which are known to form a limit-periodic structure.

3.5 Acknowledgements

This work was supported by the Research Triangle MRSEC under grant number DMR-1121107 and the US National Science Foundation under grant OISE 1065466. We would also like to thank Dr. Sabine Klapp for helpful discussions.

3.6 References

1. T. W. Byington and J. E. S. Socolar, *Phys. Rev. Lett.*, 2012, 108, 045701
(DOI:10.1103/PhysRevLett.108.045701).
2. C. Janot, *Quasicrystals: a primer*, Clarendon Press; Oxford University Press, Oxford; New York, 1994.
3. N. A. Wasio, R. C. Quardokus, R. P. Forrest, C. S. Lent, S. A. Corcelli, J. A. Christie, K. W. Henderson and S. A. Kandel, *Nature*, 2014, 507, 86-+
(DOI:10.1038/nature12993).
4. X. B. Zeng, G. Ungar, Y. S. Liu, V. Percec, S. E. Dulcey and J. K. Hobbs, *Nature*, 2004, 428, 157-160 (DOI:10.1038/nature02368).
5. K. Hayashida, T. Dotera, A. Takano and Y. Matsushita, *Phys. Rev. Lett.*, 2007, 98, 195502 (DOI:10.1103/PhysRevLett.98.195502).
6. S. Fischer, A. Exner, K. Zielske, J. Perlich, S. Deloudi, W. Steurer, P. Lindner and S. Foerster, *Proc. Natl. Acad. Sci. U. S. A.*, 2011, 108, 1810-1814
(DOI:10.1073/pnas.1008695108).
7. D. V. Talapin, E. V. Shevchenko, M. I. Bodnarchuk, X. Ye, J. Chen and C. B. Murray, *Nature*, 2009, 461, 964-967 (DOI:10.1038/nature08439).
8. C. Xiao, N. Fujita, K. Miyasaka, Y. Sakamoto and O. Terasaki, *Nature*, 2012, 487, 349-353 (DOI:10.1038/nature11230).
9. J. Dubois, *Chem. Soc. Rev.*, 2012, 41, 6760-6777 (DOI:10.1039/c2cs35110b).
10. *Quasicrystals: an introduction to structure, physical properties and applications*, Springer, Berlin ; New York, 2002.

11. C. Marcoux, T. W. Byington, Z. Qian, P. Charbonneau and J. E. S. Socolar, *Physical Review E*, 2014, 90, 012136 (DOI:10.1103/PhysRevE.90.012136).
12. C. Marcoux Belley, Doctor of Philosophy, Duke University, 2016.
13. R. Berger, in *in Memoirs of the American Mathematical Society (66)*, ed. anonymous 1966, pp.1-72.
14. R. M. Robinson, *Inventiones Mathematicae*, 1971, 12, 177-& (DOI:10.1007/BF01418780).
15. C. Goodman-Strauss, *European Journal of Combinatorics*, 1999, 20, 375-384 (DOI:10.1006/eujc.1998.0281).
16. J. E. S. Socolar and J. M. Taylor, *Mathematical Intelligencer*, 2012, 34, 18-28 (DOI:10.1007/s00283-011-9255-y).
17. S. Gangwal, A. Pawar, I. Kretzschmar and O. D. Velev, *Soft Matter*, 2010, 6, 1413-1418 (DOI:10.1039/b925713f).
18. S. Gangwal, O. J. Cayre, M. Z. Bazant and O. D. Velev, *Phys. Rev. Lett.*, 2008, 100, 058302 (DOI:10.1103/PhysRevLett.100.058302).
19. S. Gangwal, O. J. Cayre and O. D. Velev, *Langmuir*, 2008, 24, 13312-13320 (DOI:10.1021/la8015222).
20. M. Skarabot, M. Ravnik, S. Zumer, U. Tkalec, I. Poberaj, D. Babic, N. Osterman and I. Musevic, *Physical Review E*, 2008, 77, 031705 (DOI:10.1103/PhysRevE.77.031705).
21. A. R. Leach, *Molecular modelling : principles and applications*, Pearson/Prentice Hall, Harlow, England ; New York, 2001.

22. D. G. Barci and D. A. Stariolo, *Physical Review B*, 2009, 79, 075437
(DOI:10.1103/PhysRevB.79.075437).
23. Q. Chen, S. C. Bae and S. Granick, *Nature*, 2011, 469, 381-384
(DOI:10.1038/nature09713).

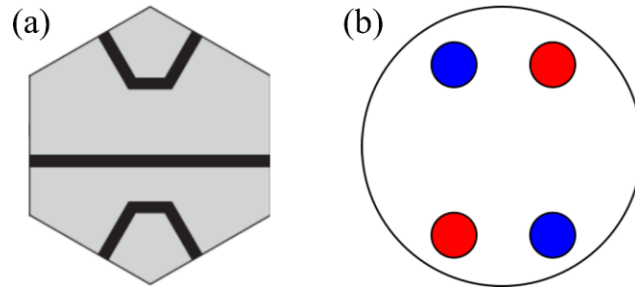


Figure 3.1. (a) Black-stripe model in which the specific pattern of lines induces the formation of a limit-periodic structure upon slow temperature quench ¹¹. (b) Double-dipole disk model with four charges of alternating sign. The charges in play a similar role to the top and bottom lines in (a); the horizontal bar in (a) is however absent in (b).

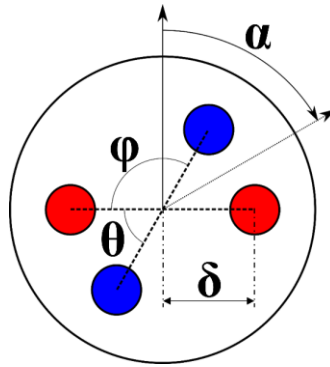


Figure 3.2. Double dipole disk model used in simulations where blue circles represent negative point charges and red circles represent positive point charges. θ and ϕ refer to fixed angles while δ refers to the distance between the center of the disk and a charge. The orientation of the particle is defined by the angle α , which for the orientation shown is equal to $\pi/3$. The orientation is therefore positive for clockwise rotations and negative for counterclockwise rotations.

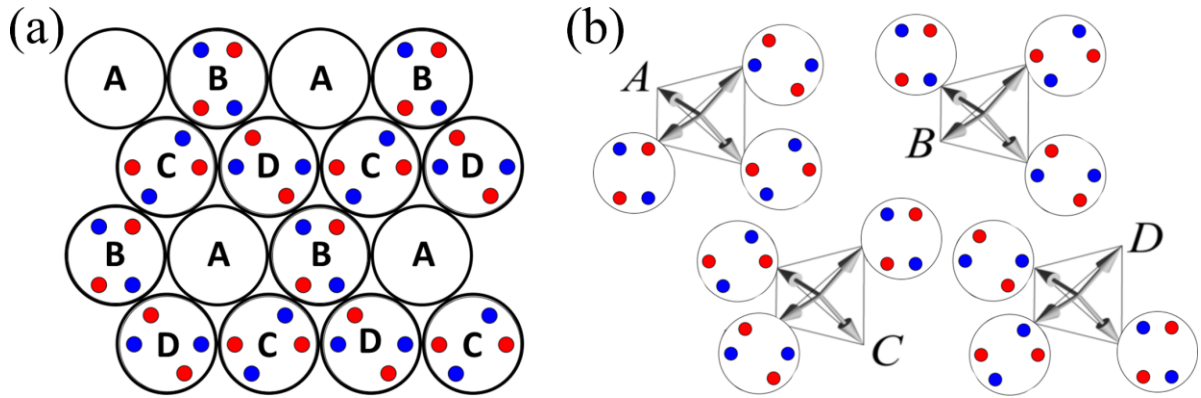


Figure 3.3. (a) Sublattice labeling with level-1 ordering shown in which sublattice A contains rattlers whose orientations are not shown. (b) Mapping used to define the value of e_x for an individual disk based on its orientation (up, left or right) and sublattice (A, B, C or D) (Figure adapted from Ref ¹¹). The 3D arrows shown inside the tetrahedrons are the four possibilities for the unit vector e_x .

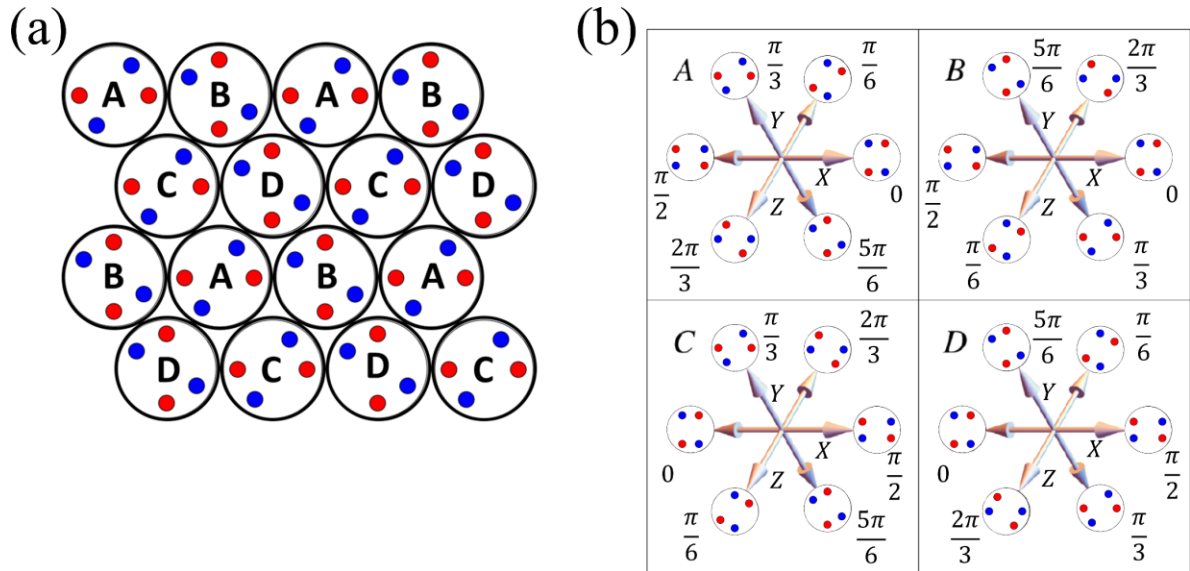


Figure 3.4. (a) Sublattice labeling with striped phase shown. (b) Mapping used to define the value of e_k for an individual disk based on its orientation and sublattice (A, B, C or D). The 3D arrows shown inside the octahedrons are the six possibilities for the unit vector e_k .

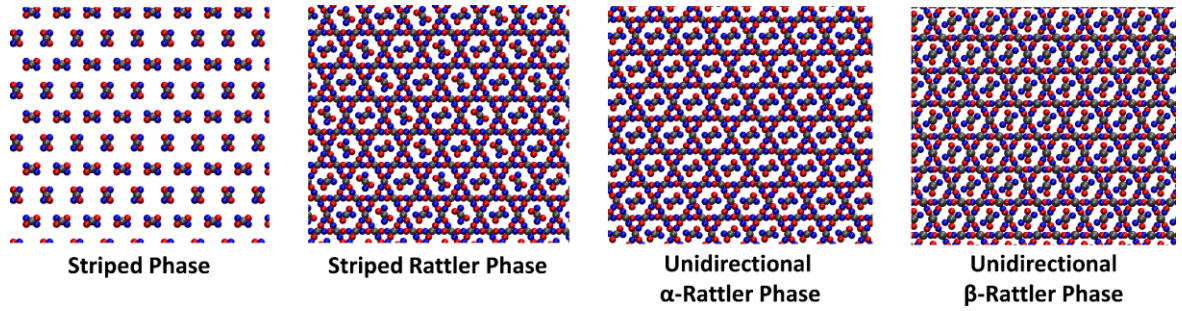


Figure 3.5. Images of some of the non-limit-periodic-structures found in our simulations. The gray spheres represent the excluded area of the disk but are shown at reduced size to better visualize the orientation of the disks. Striped phases have alternating bands of disks whose order is determined by the striped order parameter. These stripes can also occur for just the rattlers as shown in the second image. The unidirectional rattler phase is investigated by first measuring ϕ_1 on the entire system and then calculating the nematic order parameter on the rattlers.

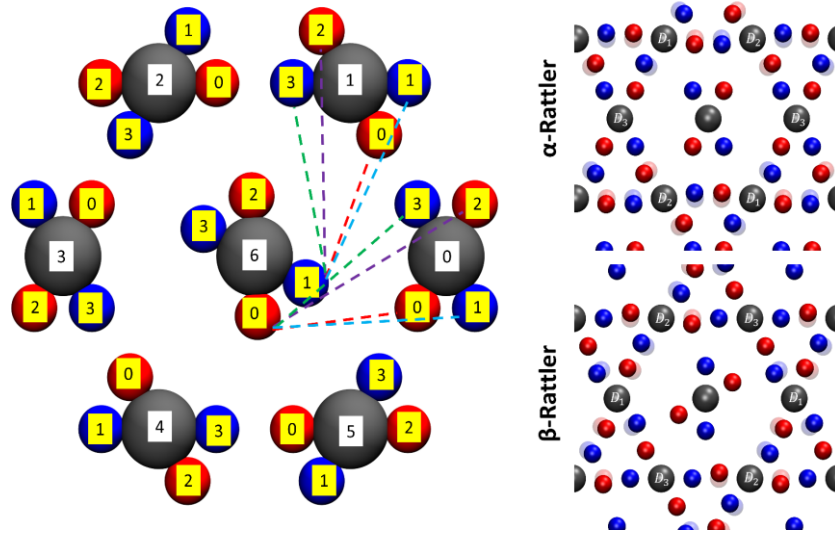


Figure 3.6. Left: Image of a rattler (disk 6) and its surrounding six disks (disks 0-5) which are in a Kagome lattice configuration. Regardless of the orientation of the rattler, its potential energy of interaction with the surrounding six disks is zero. The dotted lines show four of the distances which cancel out pairwise according to the color of the lines. Right: Images showing the distortion of the rattlers in the α -rattler and the β -rattler phases with the perfectly aligned level-1 structure shown behind transparently. D_1 and D_2 refer to the two sublattices which contain disks which are rotated off of their level-1 structure while D_3 is the non-distorted sublattice.

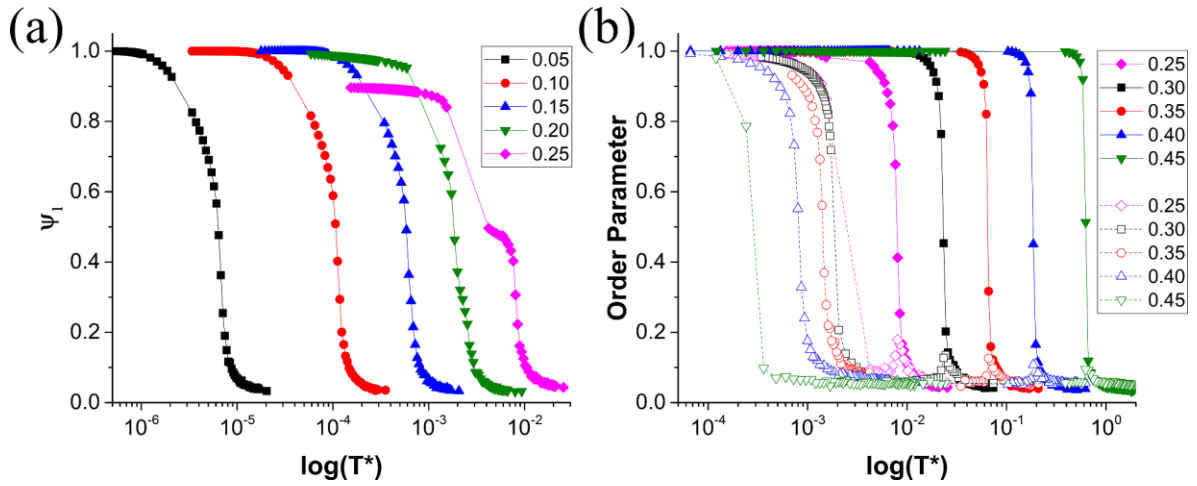


Figure 3.7. (a) Striped order parameter, ψ_1 , versus reduced temperature T^* for continuous rotation simulations. Values of δ are shown in the legend. (b) ϕ_1 (filled symbols and solid lines) and nematic order parameter (open symbols and dashed lines) for continuous rotation simulations. Values of δ are shown in the legend.

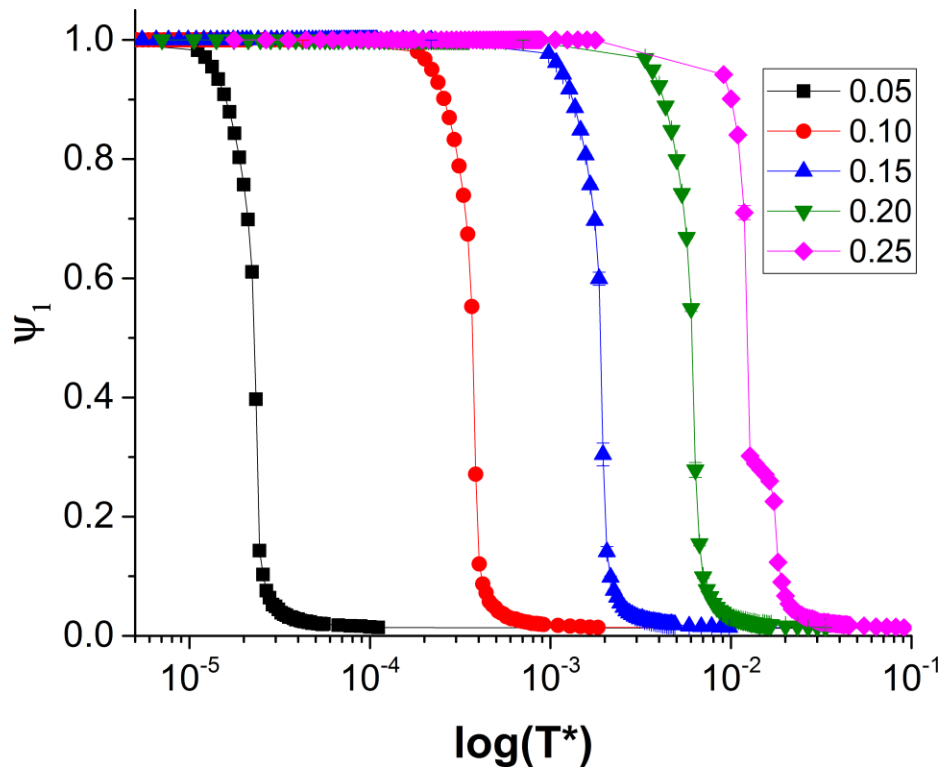


Figure 3.8. ψ_1 for $\delta \leq 0.25$ using the R6 moveset. Values in the legend indicate the value of δ .

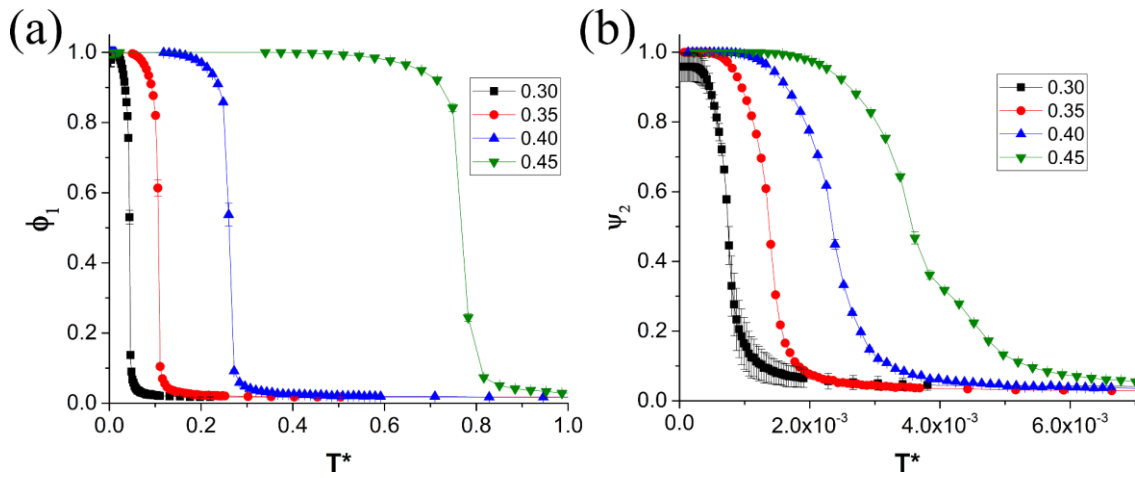


Figure 3.9. ϕ_1 (a) and ψ_2 (b) vs. T^* for $\delta \geq 0.30$ using the R6 moveset. Note the difference in the horizontal scales on the two plots. Values in the legend indicate the value of δ .

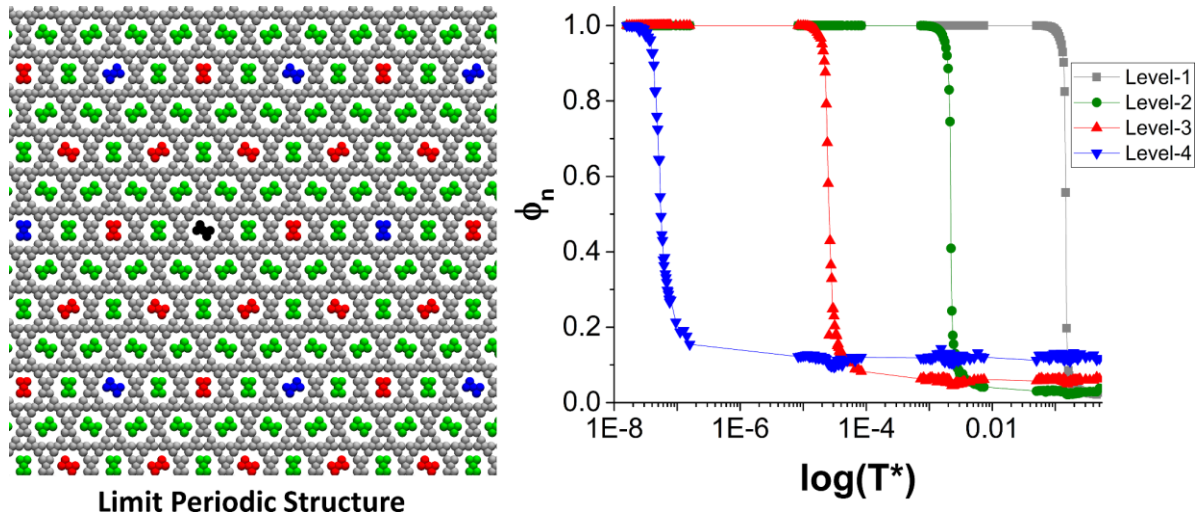


Figure 3.10. Subset of the system (22x24 of a 64x64 system) at $\delta = 0.35$ using the R3 moveset color coded according to the level the disks are in. Gray corresponds to level-1, green to level-2, red to level-3, blue to level-4 and black is not ordered. The figure on the right plots ϕ_n for these four levels versus $\log(T^*)$.

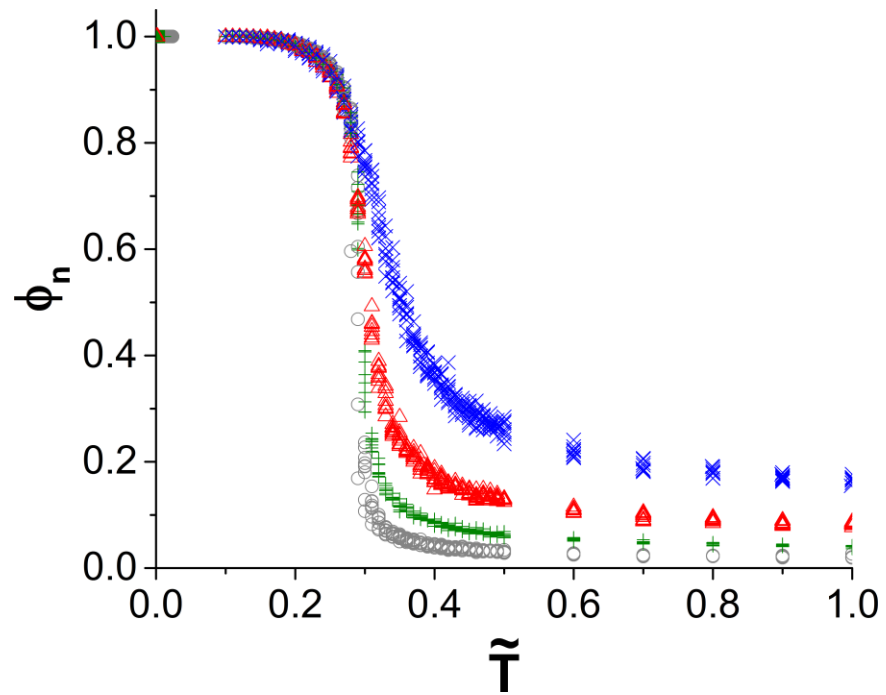


Figure 3.11. Order parameters for four levels of order plotted versus $\tilde{\tau}$ where gray circles are for level-1, green crosses for level-2, red triangles for level-3 and blue x's for level-4.

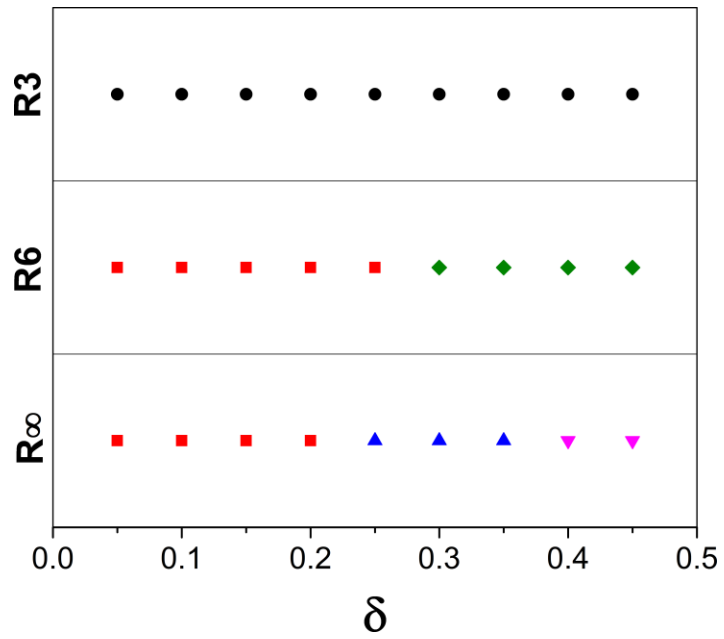


Figure 3.12. State diagram showing the different phases found for a given moveset as a function of δ . Red squares stand for striped phase, blue triangles for α -rattler phase, pink upside-down triangles for β -rattler phase, green diamonds for striped rattler phase and black circles for limit-periodic phase.

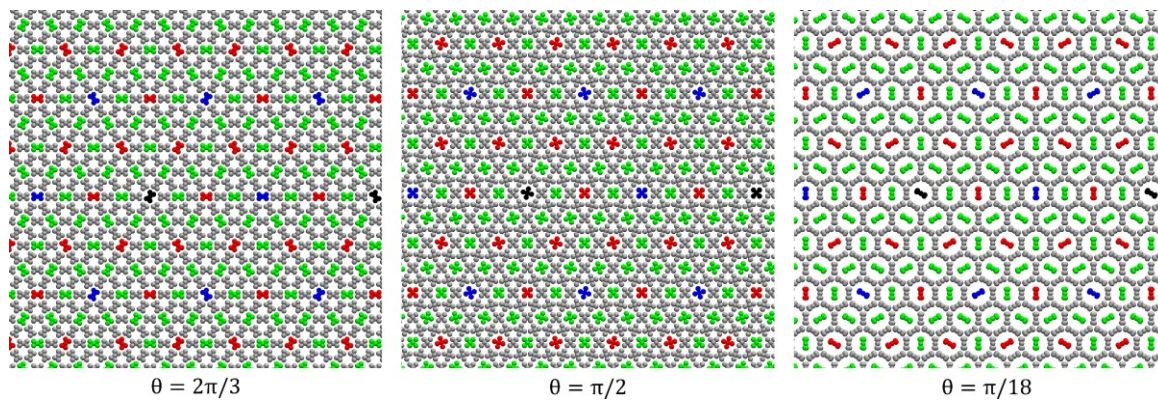


Figure 3.13. Images of the structures formed for the double-dipole model at different values of theta; disks are colored the same as in Figure 3.10. Up to level-4 order is seen in these limit-periodic structures. This suggests that θ does not influence whether the system will form a limit-periodic structure.

CHAPTER 4

Simulation Study on the Structural Properties of Colloidal Particles with Offset Dipoles

Chapter 4 is essentially a manuscript by David M. Rutkowski, Orlin D. Velev, Sabine H. L. Klapp and Carol K. Hall in preparation.

Simulation Study on the Structural Properties of Colloidal Particles with Offset Dipoles

David M Rutkowski^a, Orlin D. Velev^a, Sabine H. L. Klapp^b and Carol K. Hall^{a*}

^aDepartment of Chemical and Biomolecular Engineering, North Carolina State University, 911 Partners Way, Raleigh, North Carolina 27695, USA

^bInstitute of Theoretical Physics, Technical University of Berlin, Str. EW 7-1 Hardenberstr. 36, D-10623 Berlin, Germany

Abstract

A major research theme in materials science is determining how the self-assembly of colloidal particles is influenced by their interparticle interactions. In this paper, we describe results from quasi-2D Monte Carlo simulations of systems of colloidal particles with offset transversely-oriented extended dipoles interacting via an intermediate-ranged Yukawa potential. The systems are cooled slowly through an annealing procedure during which the temperature is lowered in discrete steps, allowing the system to equilibrate. We perform ground state calculations for two, three and four particles for several shifts of the dipole vector from the particle center. We create state diagrams in the temperature area fraction plane outlining the boundaries between fluid, string-fluid and percolated states at various values of the shift. The systems assemble into chains when the dipoles are centrally located, and into zig-zag chains that do not align in a side-side fashion when the dipoles are slightly offset from the particle center. We find that the effective cooling rate in our simulations has an impact on the structures formed with chains being more prevalent if the system is cooled

quickly and cyclic structures more prevalent if the system is cooled slowly. As the dipole is further shifted from the center, there is an increased tendency to assemble into small cyclic structures at intermediate temperatures. These systems further self-assemble into open lattice-like arrangements configurations at very low temperatures; such structures might be useful for photonic applications.

4.1 Introduction

Colloidal particles with anisotropic properties (e.g. anisotropic coating, shape or charge distribution) are of interest because they self-assemble into a wide variety of structures that could be useful in photonic crystals^{1,2}, rheological devices³ and drug delivery applications⁴. Those with anisotropic charge distribution are especially appealing because their properties and structures can be tuned in response to external electric or magnetic fields, thereby providing a route to the development of actively-controllable materials. The precise distribution of charge within a colloidal particle has been found to have a significant effect on the ultimate structures formed⁵⁻⁷. Understanding how the interactions between these particles dictate their bulk phase behavior is therefore a major focus of colloidal science, the end goal being to improve their use in novel applications.

Colloidal particles with induced or permanent dipoles have been found to assemble into chains and rings. Anisotropically charged colloidal particles have been created by placing polystyrene spheres in an external electric field, causing a separation of charge within the particle that leads to particle chaining along the field vector⁸. Such particles effectively have induced (i.e. temporary) dipoles at their centers. Colloids with permanent dipoles at their centers have also been created; ferrofluids (magnetic particles in a non-magnetic fluid) can either assemble into aggregates or isotropically oriented chains depending on the colloid's size, magnetic dipole strength, solvent conditions, etc.^{9, 10}. Anisotropy can be further increased by shifting the dipole out of the center of the particle either in an induced^{5, 6} or permanent^{7, 11} fashion. Particles with induced offset dipoles assemble into staggered chains which have a zig-zag configuration or double chains which are two parallel chains

offset by half a particle diameter. Particles with permanent offset dipoles instead form small aggregates: dimers, polyhedral or cyclic structures ⁷ or hexagonally packed lattices ¹¹. Although many simulations have been performed on systems containing centrally located point dipoles ¹²⁻¹⁷, relatively few have focused on systems containing off-center dipoles. Simulations of off-center colloidal particles, with a few exceptions ^{18, 19}, fall into two main categories:: those which investigate longitudinal point dipoles (the dipole vector is parallel to the line connecting the sphere center and the dipole vector midpoint) ^{20, 21} and those which investigate transverse point dipoles (the dipole vector is perpendicular to the line connecting the sphere center and the dipole vector midpoint) ^{18, 22, 23}. Particles of both types tend to form either chains or small cyclic aggregates, with longitudinal point dipoles forming so called magic clusters of 3, 12, 27 or more particles as in experiments on Co/Pt capped particle ¹¹, and transverse point dipoles forming staggered chains as seen in several experiments ⁵⁻⁷. Most models of dipolar colloidal particles represent the dipolar interaction with point dipoles that interact via long range potentials. Though it has been determined that a single point dipole well describes the interaction between spherical particles of finite size ²⁴, there may be experimental situations where an extended dipole is more accurate. Additionally, having the distance between the charges be a controllable parameter may lead to even more exotic phases. Both the structure and dielectric constant systems of point dipoles and extended dipoles were found to differ significantly ²⁵. Similarly, there may be large differences in the structures formed by offset dipoles in the point dipole and extended dipole representations which to our knowledge not yet been considered.

This paper describes the results of Monte Carlo simulations of systems of colloidal particles with off-center transverse, extended dipoles in quasi-2d. By using an extended dipole, we are free to change the separation distance between the charges, d . We investigate two cases, one in which the particles have $d = 0.01\sigma$, where σ is the diameter of the colloidal particle, which we refer to as Case 1, and one in which $d = 0.40\sigma$ which we refer to as Case 2. We investigate both Case 1 and Case 2 for a number of different shifts of the dipole vector out of the center of the particle. The interaction between charges is represented by a Yukawa potential of intermediate range instead of by a Coulomb potential. The Yukawa potential was chosen because it mimics electrical charges screened by a solvent at high salt concentration. This potential keeps the anisotropic character of a dipolar sphere but neglects the long-range interaction. An added benefit of using a Yukawa potential is that we do not need to utilize Ewald sums which can greatly increase the simulation time. The work presented here builds upon prior simulations particularly those by Novak et al. who performed quasi-2D simulations of offset point dipole spheres at several different offsets and a single temperature.²² We perform finite temperature simulations over a range of temperatures on systems containing 512 particles for Cases 1 and 2 for a range of displacements of the dipole from the center of the colloidal particle. For both Case 1 and Case 2 we also perform ground states analysis of two, three and four particles in which we determine the structure with the lowest potential energy.

Highlights of our results include the following. Our ground state configurations for systems containing two and three offset dipolar spheres are consistent with those from prior simulations but differences start to appear in the ground states for four offset dipolar spheres

²². We calculate state diagrams from our simulated annealing runs which outline polymerization boundaries (indicating when particles first start to associate) and percolation boundaries (indicating when a network forms). We find that the location of the percolation line is dependent on the rate of cooling especially at low area fractions. Finally, we find that systems of particles with relatively large shifts of the dipole from the center form cyclic structures at intermediate temperatures and that these further assemble into lattice-like arrangements at the lowest temperatures. These lattice assemblies generally consist of separate domains based on the chiralities of their constituent particles at high shifts and a single domain aggregate at low shifts.

4.2 Model and Methods

The offset dipolar colloidal particle considered in this paper is represented by a sphere of diameter σ , to account for the particle excluded volume and contains two embedded point charges of opposite signs as shown in Figure 4.1. The extended dipole in our model is always in the transverse orientation, i.e. the vector between the two point charges of opposite sign is perpendicular to the line connecting the sphere center and the midpoint between the two point charges. In our model d^* is the distance between the two point charges reduced by σ ; δ^* is the shift of the dipole vector, the distance between the sphere center and the midpoint between the two charges, also reduced by σ . In our model θ is the angle made by the two charges and the center of the particle. We investigate two separate cases: one where $d^* = 0.01$ (Case 1) and one where $d^* = 0.40$ (Case 2). We chose to simulate Case 1 because it is similar to a point dipole; our purpose in this case is to investigate the effect of having an

intermediate range potential. We chose to simulate Case 2 because it has a significant separation between the charges yet still allows for a broad range of shifts from the center, δ^* . As d^* becomes larger in our model, the range over which δ^* can vary and still keep the point charges inside the sphere becomes smaller. For example, at $d^* = 1.00$ the only value that δ^* can take is 0, $d^* = 0.40$ allows for δ^* to vary between 0 and 0.46 (or θ to vary from 180° to 47.2°) and $d^* = 0.01$ effectively allows δ^* to vary between 0 and 0.50 (or θ to vary from 180° to 1.1°).

An additional feature of our model is that it is chiral if the particles are constrained to rotate only in a two-dimensional plane which occurs often in our simulations since they are performed in quasi-2d. The term “quasi-2d” means that the centers of colloidal spheres in our model are constrained to lie on a plane while the point charges are free to rotate out of the plane. The chirality stems from the fact that the charges can either be in the configuration shown in Figure 4.1 or can have their identities exchanged; no in-plane rotational move is able to convert between the two. Particles in clusters are strongly bound to each other meaning they cannot rotate out of plane without an energetic penalty so at low temperatures they have a fixed chirality. Individual particles are still allowed to rotate out of plane and therefore can flip their chirality. In snapshots of our simulations we color the sphere center transparent green if it is the chirality shown in Figure 4.1 and transparent purple if it is the opposite chirality.

The interactions between a pair of colloidal particles, i and j , is the sum of the interactions between the spheres (excluded volume) and the four pairs of charges. The colloidal spheres interact with a hard sphere potential i.e. $U(r_{ij}^*) = \{\infty \text{ if } r_{ij}^* \leq$

$1.0; 0 \text{ if } r_{ij}^* > 1.0\}$ where $r_{ij}^* = r_{ij}/\sigma$ is the reduced separation distance. The point charges interact via a Yukawa interaction which can be written as $U(r^*) = -\varepsilon q_1 q_2 / r^* \exp(-\kappa^* r^*)$ where ε is a constant with units of energy per charge squared, q_1 and q_2 are the two interacting charges, $r^* = r/\sigma$ where r is the distance between the charges, and $\kappa^* = \kappa\sigma$ where κ is the inverse Debye length. The Yukawa potential in our simulations has a κ^* of 3.29. This was determined by using the formula for 1:1 electrolytes, $1/\kappa [nm^{-1}] = 0.304/[NaCl]^{0.5}$, where $[NaCl]$ is the concentration of NaCl in solution²⁶. We assumed a NaCl concentration of $10^{-6} M$ and a particle size of $\sigma = 10^{-6} m$ based on approximate sizes of colloidal particles and realistic values of salt concentration^{5,7}. We non-dimensionalize our energy by $\varepsilon q_1 q_2$ so that our reduced temperature is therefore equal to $T^* = kT/\varepsilon q_1 q_2$. The cutoff of our Yukawa potential is based on the distance between the colloidal sphere centers rather than the distance between charges and was taken to be 3.7σ . Because we base our cutoff on the colloidal sphere centers, the four charge pairs are always included in a potential energy calculation which makes for less distortion in the potential at the cutoff. We cut off our potential at 3.7σ because the absolute value of the difference in the potential compared to a cutoff at 12σ remains smaller than 10^{-6} .

We perform Monte Carlo (MC) simulations in quasi-2d at constant temperature and simulation area on systems of offset dipolar spheres. Quasi-2d mimics an experimental setup where the colloidal particles are placed between two glass slides⁵. Our simulations were performed in a square box with periodic boundary conditions in the x and y directions. In addition to performing single particle translation and rotation moves we also implemented

cluster translation and rotation moves as described in the appendix of reference ²⁷. Cluster moves were required in order to accelerate the aggregation process as particles often become frozen into dimers for a significant number of moves when only single particle moves are used. A cluster move consists of the random selection of a particle in the system followed by the recruitment of additional nearby particles into the cluster. Additional particles are recruited into the cluster with probability $\max[0, 1 - \exp(\beta_f u_f)]$ where u_f is the total potential energy between the two particles and β_f is taken randomly from the range $[0, \beta]$ where $\beta = 1/kT$. Recruited particles can themselves recruit additional particles that are their neighbors. Each possible pair of particles, either within the cluster and/or between cluster and its surroundings is considered only once. The cluster is defined after all pairs in the cluster are considered. In order to maintain super-detailed balance for the cluster moves, the acceptance probability was modified from $\min\{1, e^{-\beta(\Delta E)}\}$ to $\min\left\{1, e^{-\beta(\Delta E)} e^{\beta(\Delta U)} \prod_{ij}^R \frac{1 - e^{\beta_f u_f(r_{ij}^n)}}{1 - e^{\beta_f u_f(r_{ij}^0)}}\right\}$ where ΔE is the change in the potential energy of the system, ΔU is the change in the attractive part of the potential (i.e. positive potentials are not included) between the moved cluster and the particles it interacts with. $u_f(r_{ij}^v)$ is the potential between particles i and j in the cluster where the superscript refers to the state of the system which can be either the state before the move ($v = 0$) or after the move ($v = n$). The final (product) term is non-unity only if the potential within the cluster changes which can only occur for a cluster rotation move. There are many ways to potentially link the particles to form a given cluster; a specific set of links used to form a cluster is known as a realization of links, R ²⁷. The product only runs over the specific realization of links, R , used

to form the cluster for that move, i.e. u_f is only calculated between pairs of particles which incorporated new particles to the clusters. A cluster move was selected to occur on average once every 100 single particle moves; cluster translation and rotation moves were chosen with equal probability. We adjusted the maximum translation or rotation of all moves so that ~50% of the moves were accepted.

The simulation procedure for all of our systems is the following. All systems have 512 dipolar spheres unless otherwise stated, and are started from a high temperature, and therefore random, configuration. The systems are cooled slowly through an annealing procedure during which the temperature is lowered in discrete steps, allowing the system to equilibrate at each step. The values of the temperature at each step, T^* , are chosen as $T^* = \tilde{T}|U_{min}^*(\delta, d)|$ where \tilde{T} is a number less than or equal to 1.0 and $U_{min}^*(\delta, d)$ is the minimum pair energy experienced by a given particle which is determined via the ground state calculations that we perform for two particles (described in the next section). \tilde{T} is therefore also equal to $2/\lambda(\delta, d)$ where $\lambda(\delta, d)$ is the dipolar coupling strength referenced in many other simulations of dipolar systems²¹⁻²³ and is equal to $|U_{min}^*(\delta, d)|/2T^*$ ²³. We start from a high temperature at which the system is completely randomized and in an isotropic fluid phase. The cooling rate is slowed as the temperature is lowered in order to more accurately determine the low energy states of the systems. For each temperature step we performed 10^6 moves per particle. System averages are calculated over the last half of each run.

We define two particles to be in a cluster based on a clustering definition which takes into account both the distance between particles and their energy. If the distance between the centers of two particles is less than 1.3σ and the net potential between the two particles is

negative, we count the two particles as being part of the same cluster. This distance was chosen based on prior simulation work on dipolar particles^{12, 22, 23}.

Based on the above clustering definition, we calculate several parameters that measure the system structure. The first of these is the extent of polymerization which gives a measure of whether or not the system is at the beginning stages of aggregation. The extent of polymerization is defined as $\Phi = \langle N_a/N \rangle$ where N_a is the number of particles in a cluster of size 2 or greater and N is the number of particles in the system; the brackets indicate an ensemble average. The second parameter is the percolation probability which gives a measure of whether the system has formed a network. A percolated system is one that has at least a single cluster that both spans the simulation box and connects back to itself. A percolated cluster is therefore one which has an infinite length when viewed with its periodic images. The variable π signals whether a given configuration is percolated ($\pi = 1$) or not ($\pi = 0$) and is used in the overall definition of the percolation probability, Π , as $\Pi = \langle \pi \rangle$ where the brackets indicate an ensemble average. Of note is that percolation is a prerequisite for gelation, but it not sufficient by itself to declare a system a gel.

We also measure the number of cyclic structures in our systems by slightly modifying the aggregation criteria. For this analysis, we include particles in clusters that have separation distances $\leq 1.1\sigma$ and interaction energies less than or equal to $U_{min}^*(\delta, d)/2$. These changes ensure that only particles bound by energies close to the minimum pair energy are included and so individual cyclic structures are isolated even when cyclic structures are aggregated together. A cluster is labeled a polygon of size n if it meets two criteria. The first is that the distances from the centers of all the particles in the cluster to the geometric center of the

cluster are within 5% of $\omega/2\sin(\pi/n)$, the distance from the center of an ideal polygon of size n to one of its vertices where ω is the length of a side of polygon. The second criteria is that the orientational bond order parameter, ϕ_k , must be greater than 0.95. The orientational bond order parameter is $\phi_k = 1/n \left| \sum_{w=1}^n \exp(in\theta_{kw}) \right|$ where i is the imaginary number, n is the size of the cluster and θ_{kw} is equal to $\arccos(\hat{r}_{kw} \cdot \hat{r}_{k\lambda})$ where \hat{r}_{kw} is a unit vector between particles k and w in the cluster and $\hat{r}_{k\lambda}$ is a unit vector between particle k and a random particle λ in the cluster. Bead k is an imaginary bead placed at the geometric center of the cluster while the identity of the bead λ is fixed for a given cluster, but can be chosen arbitrarily. This procedure is used to determine the fraction of particles, f_p , in the system that are a member of a cyclic structure having up to twenty sides.

4.3 Results and Discussion

We begin by describing our ground state results for systems of two, three and four particles, with the aim of providing insight into how our model differs from previous simulated systems and how cases 1 and 2 differ. For each value of d^* and δ^* , we perform at least three simulated annealing MC runs of the two, three and four particle systems until we reach a low enough temperature that the particles effectively freeze in place. The charges are not restricted to be in-plane for the simulated annealing. We take the lowest potential energy from these runs as the ground state. For two particles, we also find the configuration with the minimum potential energy by numerically minimizing the potential energy for a pair of

particles at contact with their dipoles in plane. The charges are restricted to be in-plane in the potential energy minimization calculations. We characterize all ground state structures by measuring the angle between all pairs of dipoles in the structure, $\Delta_{ij} = \cos^{-1}(\hat{\mu}_i \cdot \hat{\mu}_j)$ where $\hat{\mu}_i$ and $\hat{\mu}_j$ are unit vectors in the direction of the dipole pointing towards the positive (red) charge and i and j run over the indexes of the particles in the structure.

For a pair of particles, we find the ground state configuration of our model by both performing simulated annealing at selected values of δ^* and by minimizing the potential energy function at contact when their dipoles are confined to the x-y plane as a function of δ^* . The potential energy functions involve a sum of the energies between the four pairs of charges as a function of the in-plane rotation angle of particle 1 with respect to the y-axis, α_1 , and particle 2 with respect to the y-axis, α_2 . We assume that the potential energy minimum occurs when the dipoles are in plane as others have^{20, 23}. This assumption proves reasonable since all of the dipoles are in the x-y plane for the structures found via our simulated annealing runs. For the minimum energy pair configuration, we plot $\cos(\Delta)$ versus δ^* as solid lines for both Case 1 (shown in red) and Case 2 (shown in blue) in Figure 4.2. The dashed lines are for the same respective cases using a Coulomb potential between the charges instead of the Yukawa potential that we use in the finite temperature simulations. The black line represents a point dipole particle²³ and coincides with the dashed red line, showing that a Coulomb potential for a dipolar system with $d^* = 0.01$ has essentially the same pair structures as the point dipole system. Switching to a Yukawa potential shifts the curve to the right, but it remains the same qualitatively. Using a charge separation of $d = 0.40$ (Case 2) shifts the curves both up and to the right so much that the antiparallel configuration

$(\cos(\theta) = -1.0)$ never occurs. The points on this plot are from the simulated annealing runs which are in agreement with the minimum pair energy calculations.

We next describe results from ground state simulations of three particles for both cases. The top left of Figure 4.3 shows the structures found in these simulated annealing runs which vary from linear chain (S1-3) at $\delta^* = 0$, to bent chain (S2-3) at $\delta^* = 0.05$, to triangular arrangement (S3-3) at $\delta^* = 0.2$, to a triangular arrangement in which two of the dipoles are antiparallel and the third is perpendicular to both the others (S4-3) at $\delta^* = 0.4$. In this notation, S stands for structure, the first number is a unique number assigned to each structure and the second number indicates the number of particles in the structure. This sequences of structures is the same as that seen by Arzu et al.²³ but slightly different from that seen by Novak et al.²² in that we do not find a “zipper” configuration. Comparison of Case 2 to Case 1 is aided by the graphs on the right of Figure 4.3 in which we plot the three angles (i.e. Δ_{12} , Δ_{13} , Δ_{23} where the subscripts indicate the indexes of the dipoles in the ground state structure) between dipole pairs in the ground state configurations, Δ_{ij} , vs δ^* . Often the angles are equal as is the case for S1-3 (all Δ_{ij} 's are 0.0) or S3-3 (all Δ_{ij} 's are 2.09) and show up in Figure 4.3 as a single point. Each structure that we find in our simulations has a unique set of angles between the three dipoles and therefore the structures are identifiable by the arrangements of the three points on the plots in Figure 4.3 for a given value of δ . For Case 2 the S2-3 region (blue) is broadened compared to Case 1 and the S3-3 region (green) shifts towards higher values of δ . Consequently, Case 2 never has the antiparallel pair arrangement region (S4-3) which is in accordance with the minimum pair energy analysis for Case 2.

Our final ground state analysis is for four particles. The top left of Figure 4.4 shows the structures found in these simulations which vary from straight chain (S1-4) at $\delta^* = 0.0$, bent chain (S2-4) at $\delta^* = 0.05$, square arrangement (S3-4) at $\delta^* = 0.1$, triangular arrangement (S4-4) at $\delta^* = 0.3$ and pair of antiparallel pairs (S5-4) at $\delta^* = 0.4$ as shown in Figure 4.4. The notation scheme is the same as before; the final number in this instance indicates that the structures contain four particles. The number of structures seen at low to intermediate δ^* for both cases is greater than for the point dipole in quasi-2d case which has only a square configuration ground state from $\delta^* = 0.0$ to $\delta^* = 0.45$ ²². S1-4, S2-4 and S4-4 consequently appear to be unique to our simulations, likely due to the limited range of our potential. Comparing Case 2 to Case 1 is aided by the plots on the right of Figure 4.4 which show the six angles (i.e. $\Delta_{12}, \Delta_{13}, \Delta_{14}, \Delta_{23}, \Delta_{24}, \Delta_{34}$ where the subscripts again refer to the indexes of the dipoles in the ground state) between pairs of dipoles in the ground state configurations Δ_{ij} , vs δ^* . For Case 2 the S3-4 region is broadened while the S4-4 region shifts slightly towards higher values of δ . Again, Case 2 is missing the antiparallel structure present at the highest values of δ^* for $d^* = 0.01$. Finding the lowest energy configurations for four particles proved difficult especially for the curved chain structure since there was a structure with extremely similar potential energy consisting of two pairs of particles with opposite chiralities that formed a zig-zag chain. The potential energy of this structure is less than 0.1% of the potential energy of the curved chain.

Since our ground states analysis shows that cyclic structures are often the lowest energy structure, we determine the size of the cyclic configuration with the lowest potential energy as a function of δ^* . We do this by measuring the potential energy of particles whose

centers are the vertexes of polygons from size three to twenty normalized by the size of the polygon. In these polygons the particles' dipoles are aligned perpendicular to the line connecting the particle center and the center of the polygon. Particles of the same chirality were used. For the dimer case we use the potential energy from the ground state analysis and so the dipoles are not restricted to being perpendicular to each other. The plot in Figure 4.5 displays the size n of the lowest energy cyclic structure as a function of δ^* for Cases 1 and 2. From this plot it can be seen that the range of δ^* where a polygon of size n is the most stable decreases as n increases. This means that the value of δ^* must be more precisely specified in order to see large polygons form. Additionally of note is that the dimer is the lowest energy state only for a small range of shifts, d^* , for Case 2. Increasing d^* moves the values over which a given cyclic structure is most stable to higher δ^* . This means that for the $d^* = 0.40$ case to see the same structure as the $d^* = 0.01$ case, the dipole would have to be shifted further out from the center. Finally, the cyclic stability regions for the point dipole occur at higher values of δ^* than for the $d^* = 0.01$ case. Since increasing d^* also moves the curve towards higher values of δ^* this suggests that there may be an "ideal" value of d^* for a given value of k in the Yukawa potential which overlaps with the point dipole data in Figure 4.5. This analysis is obviously not complete as it does not consider structures other than polygons, but it does give insight into where certain structures are most stable.

We now describe our results for systems at finite temperatures for Case 1. Systems at $\delta^* = 0.0, 0.1, 0.2, 0.3,$ and 0.4 and area fractions $0.1, 0.2, 0.3$ and 0.4 were simulated. Snapshots of final configurations are shown in Figure 4.6 for a temperature, T_1 , below the polymerization transition but above the percolation transition and at the lowest temperature

we simulated, T_2 , which is below the percolation transition. In units of \tilde{T} , T_1 is equal to 0.08, 0.07, 0.06, 0.04 and 0.02 for $\delta^* = 0.0, 0.1, 0.2, 0.3$ and 0.4 respectively. In units of \tilde{T} , T_2 is equal to 0.0005 for $\delta^* = 0.0, 0.1, 0.2$ and $1e-5$ for, for $\delta^* = 0.3$ and 0.4 respectively. The image at $\delta^* = 0.0$ shows chains typical of systems consisting of particles with central dipoles. However, as δ^* increases the structures change as more cyclic structures form at T_1 which in turn aggregate into larger superstructures at the lower temperature T_2 . The systems at $\delta^* = 0.2$ and $\delta^* = 0.4$ are particularly interesting since the particles exhibit nearly monodisperse clusters at T_1 (triangles or dimers) which further assemble into superstructures at T_2 . The $\delta^* = 0.2$ system forms a kagome-like lattice at T_2 similar to those seen in simulations of hexapolar particles²⁸, while the $\delta^* = 0.4$ system forms chains of dimers. For $\delta \geq 0.2$ the clusters tend to separate into different domains based on the chirality of the intermediate structure. Neighboring structures of the same chirality have two pairs of particles at contact while those of opposite chiralities have one particle in contact with two particles of the other cluster. The structures formed in these simulations are not completely in accordance with those predicted by the ground states analysis in Figure 4.6. For example, the ground state for $\delta^* = 0.3$ is clearly in the region of 3-mers for $d = 0.01$ yet it forms a mixture of dimers and triangle shapes at finite temperature, T_2 . Our simulations form structures similar to those seen in prior simulations of systems of point dipoles in quasi-2d by Novak et al.; their simulations were performed at a dipolar coupling strength, λ , of 5, but at slightly lower values of δ^* than ours. For example, the point dipole case forms triangles at $\delta^* = 0.3$ while we see a mixture of triangles and dimers at $\delta^* = 0.3$, (we do see all triangles at $\delta^* = 0.2$). This difference is most

likely caused by the smaller range of the potential used in our simulations compared to the point dipole potential.

We quantify the transitions between the fluid state and the states at T_1 and T_2 by plotting the percolation in Figure 4.7a) and polymerization lines in Figure 4.7b) in the ϕ vs. \tilde{T} plane for Case 1 for all values of δ^* we investigated. One interesting aspect of this diagram is that the difference between the polymerization and percolation transition temperatures increases as δ^* increases. This means that the cyclic structures that form at large δ^* and intermediate temperature are essentially fixed and have an extremely low probability of breaking apart as the temperature is lowered towards the percolation temperature. While the systems at $\delta^* = 0.1, 0.3$ and 0.4 are percolated, they do not form typical networks as they only percolate along one direction. Cyclic structures in general have a harder time forming a percolated network than the particles which form chains. Additionally, since the percolation only occurs when small, cyclic clusters aggregate to form a much larger cluster, the resulting structure will have significantly weaker connections at the junctions between these cyclic clusters than at the bonds constituting the cyclic clusters.

Next we describe results from simulations using Case 2. For Case 2 we simulated systems with $\theta = 60^\circ$ ($\delta^* = 0.346$), 90° (0.3), 120° (0.115), 135° (0.083) and 180° (0.0) for area fractions $0.1, 0.2, 0.3$ and 0.4 . Snapshots of these systems are shown in Figure 4.8 for a temperature T_1 , above the percolation transition but below the polymerization transition, and a temperature T_2 , below the percolation transition. In units of \tilde{T} , T_1 is equal to $0.0095, 0.04, 0.06, 0.07$ and 0.07 for $\theta = 60^\circ, 90^\circ, 120^\circ, 135^\circ$ and 180° respectively. In units of \tilde{T} , T_2 is equal to $1e-5$ for $\theta = 60^\circ$ and $5e-4$ for the other systems. Again, the $\delta^* = 0.0$ case forms

chains but in this instance there are fewer particles with only one nearest neighbor than for Case 1. As with Case 1, as δ^* increases for Case 2 the particles in these systems increasingly form cyclic structures. However, the specific structures formed by these systems occur at higher values of δ^* than they do in Case 1. For example, a system of all triangles occurs at $\delta^* = 0.2$ in Case 1 while it does not occur until $\delta^* = 0.346$, in agreement with Figure 4.5. Additionally, these systems are less compact than those in Case 1, especially the aggregates of triangular structures. For Case 1 at $\delta^* = 0.2$, the system forms a compact lattice-like arrangement while for Case 2 at $\delta^* = 0.346$ it forms a branched, percolating chain. The structures displayed in Figure 4.8 are likely further away from equilibrium than those in Figure 4.6; we investigate this further in simulations described later in this paper.

In order to delineate the transitions between structures, we plot the percolation and polymerization lines in the area fraction vs T^* plane for Case 2 in Figure 4.9. Compared to Case 1, the percolation lines are generally shifted towards lower values of temperature for the same or similar values of δ^* . Significantly larger error bars occur for the percolation transition at low area fraction for these systems, especially for 90° which percolated in one replicate but not the other. The polymerization transitions are less sensitive to changes in area fraction and δ^* than in Case 1. As in Case 2, the gap in temperature between the percolation and polymerization transitions increases as δ^* increases, resulting in small clusters being stable before the temperature at which they percolate. Since the structures at T_2 are likely metastable, the percolation transition temperature depends upon the cooling rate. Percolation transitions may even disappear at low area fraction and high δ^* if the system is cooled exceptionally slowly. That is, chains are more likely to form if the cooling rate is fast and

cyclic structures are more likely to form if the cooling rate is slow. In order to further quantify the comparison between the two cases, we plot in Figure 4.10 the fraction of particles that are part of a cyclic structure, f_c , as a function of δ^* for both Case 1 and 2 at all four area fractions. For Case 1 the shift to cyclic structures can be seen to occur by $\delta^* = 0.2$ while for Case 2 the shift to cyclic structures does not occur until δ^* is approximately 0.3. Increasing the area fraction of the system can be seen to reduce the number of cyclic structures, particular those of large size. This is due to the fact that the large void in the center of large polygons becomes less favored and even impossible to form as the area fraction increases.

In order to further investigate whether the structures we see at T_2 for Case 2 are equilibrium structures, we perform additional simulations in which we fix the orientation and positions of particles in cyclic structures which we then anneal. We justify these simulations by the fact that the cyclic structures we find in our earlier simulated annealing procedures are relatively stable and show no evidence of structural rearrangement upon cooling. For these simulations we therefore treat the cyclic structure as the basic particle. We expect these simulations to be further progressed towards equilibrium for a set number of moves than our usual simulations since we removed the degrees of freedom for individual particles making up the cyclic structures. We simulate systems of particles where the angle between the charges is $(n - 2)180^\circ/n$ where n is the size of the polygon for $n = 2, 3, 6$ and 8 . The system is a 50:50 mixture of chiralities since our single particle simulations appear to have no bias for one chirality over the other. The number of fused cyclic clusters in these simulations is equal to $\lceil 512/n \rceil$ where the brackets indicate a function that rounds up to the next highest

integer and n is the number of individual particles in an individual cyclic structure. Though we never see a system of all hexagons or octagons, we still simulate them to determine whether the final state into which such a system would self-assemble is lower in potential energy than the structure in Figure 4.8.

The structures formed in these simulations of cyclic cluster motion can be seen in Figure 4.11. The structures in this figure are all slightly lower in potential energy than the structures in Figure 4.8 at T_2 , suggesting that the ground states for our systems consist of open lattices. Getting to these ground states in our simulations is increasingly difficult as the angle increases (or equivalently the shift decreases) as we do not obtain cyclic structures in our single particle simulations at small shifts. Entropy effects have been noted to disfavor the creation of large cyclic structures as there is a void space in the center²¹ though the ground state for centrally located dipoles at low volume fractions are cyclic structures rather than chains. The structure at 60° is very similar to that in Case 1 at $\delta^* = 0.2$ suggesting that the simulations of Case 1 were further progressed towards equilibrium than Case 2. The simulations of particles where $\theta = 60^\circ$ and $\theta = 90^\circ$ form structures in which the final aggregate phase separates based on chirality whereas simulations with particles where $\theta = 120^\circ$ and $\theta = 135^\circ$ form structures in which the chiralities are mixed. In order to explain this difference between the behaviors with respect to chirality we measure the minimum pair energy between same chirality and opposite chirality cyclic structures of size n with angle $(n - 2)180^\circ/n$ using the same simulated annealing procedure as was done for single particle systems. From this we find that when n equals 3 or 4, the minimum pair energy is lower for pairs of the same chirality but when n is 6 or 8 the minimum pair energy is lower for opposite

chirality. Finally, we mention the open circles in Figure 4.9a) which show the percolation transitions measured in these fused cyclic cluster simulations. These percolation transitions all disappear for area fractions lower than 0.3 meaning that the cyclic structures aggregate into a single aggregate which is not percolated, in contrast to the rest of the structures in Figure 4.11. At higher area fraction, the percolation transitions for the 60° and 90° systems occur approximately at the same temperature for the single particle simulations, but the percolation transitions for 120° and 135° are shifted to significantly lower temperatures, underlining the differences between the structures formed by the single particle and fused cyclic cluster simulations.

4.4 Conclusions

We have performed quasi-2D Monte Carlo simulations of systems of offset dipolar particles with an extended dipole for small charge separation, $d^* = 0.01$ (Case 1), and intermediate charge separation, $d^* = 0.40$ (Case 2) at four area fractions. We investigate several values of the offset δ^* of the dipole out of the particle center; the dipoles considered here are perpendicular to the offset vector. We calculated the ground state structures for two, three and four particle systems for both Case 1 and Case 2 and determined the minimum energy structure as a function of δ^* . We also perform finite temperature simulations for both Case 1 and Case 2 and found the polymerization and percolation transitions for these systems. In determining these transitions, we used simulated annealing, which is a process in which we lower the temperature of the system in discrete steps while allowing the system to equilibrate at each step. We also measured the number of cyclic structures formed in our

simulations as a function of δ^* for both cases. We supplemented our simulations in Case 2 with simulations where we fuse the particles into cyclic structures and then perform the simulations with the goal of determining whether our finite temperature simulations for this case are at the ground state.

Through our simulations we have found that the shift in the dipole position, δ^* , from the dipole center has a significant impact on the structures formed while the charge separation has a smaller impact at least between $d^* = 0.01$ and $d^* = 0.40$. Structures found in our simulations can be characterized as either chains or cyclic structures, with cyclic structures becoming more favorable as δ^* increases. In addition to this dependence on δ^* , we find that the cooling rate in these simulated annealing runs has a large effect on the structures formed, with chains forming more regularly when the system is cooled quickly and cyclic structures forming more regularly when the system is cooled slowly. We outlined the phase boundaries between fluid and string-fluid as well as the percolation line for all systems simulated. Finally, via our fused cyclic cluster simulations we have found that the cyclic structures assemble into a single large aggregate upon quenching to low temperatures, and assemble into open lattice-like assemblies at intermediate to large values of shift.

Novel aspects of our work include the following. We have found that increasing the charge separation does not significantly change the types of structures into which the particles aggregate; it merely alters the value of δ^* at which specific structures are seen. This may hold for larger shifts as well since the range of possible shifts decreases as d^* increases. Though our systems are most similar to systems of colloidal particles with permanent, electric dipoles in relatively high salt environments, they form structures at least qualitatively

similar to those with permanent magnetic cubes embedded in them which interact via a long-range interaction ⁷. This suggests that the anisotropic interaction is more important than the long-range nature of the point dipole potential in forming small clusters since we see similar structures to the point dipole case.

The structures formed in our simulations may be quite different from those formed by a long-range point dipole model. In particular, the structures found in our fused cyclic cluster simulations have patterns that occur over longer distances than the cutoff used, e.g. see the right two images of Figure 4.11, and so may be expected to form drastically different structures if a longer ranged potential is used. However, the fact that our fused cyclic cluster simulations at $\theta = 60^\circ$ form the same structures as seen by Van Workum and Douglas et al. ²⁸ who simulated triangular arrangements of particles with centrally located point dipoles is interesting. It is difficult to compare the structures formed at low temperature in our simulations to the point dipole case in general since only a few simulations at intermediate temperatures have been performed with the offset point dipole system ¹⁸⁻²²; however, we see similar structures to the point dipole system at intermediate temperatures. Further investigation of the offset point dipole system would be needed in order to determine whether the point dipole system also forms open lattice-like structures at low temperatures.

4.5 Acknowledgements

This work was supported by the Research Triangle MRSEC under grant number DMR-1121107, the US National Science Foundation under grant OISE 1065466 and the German Research Foundation (DFG) through grant IRTG 1524.

4.6 References

1. Q. Chen, S. C. Bae and S. Granick, *Nature*, 2011, 469, 381-384 (DOI:10.1038/nature09713).
2. J. F. Galisteo-Lopez, M. Ibisate, R. Sapienza, L. S. Froufe-Perez, A. Blanco and C. Lopez, *Adv Mater*, 2011, 23, 30-69 (DOI:10.1002/adma.201000356).
3. O. Cayre, V. Paunov and O. Velev, *Journal of Materials Chemistry*, 2003, 13, 2445-2450 (DOI:10.1039/b308817k).
4. A. Lubbe, C. Alexiou and C. Bergemann, *J. Surg. Res.*, 2001, 95, 200-206 (DOI:10.1006/jsre.2000.6030).
5. S. K. Smoukov, S. Gangwal, M. Marquez and O. D. Velev, *Soft Matter*, 2009, 5, 1285-1292 (DOI:10.1039/b814304h).
6. B. Ren, A. Ruditskiy, J. H. (. Song and I. Kretzschmar, *Langmuir*, 2012, 28, 1149-1156 (DOI:10.1021/la203969f).
7. S. Sacanna, L. Rossi and D. J. Pine, *J. Am. Chem. Soc.*, 2012, 134, 6112-6115 (DOI:10.1021/ja301344n).
8. S. Lumsdon, E. Kaler and O. Velev, *Langmuir*, 2004, 20, 2108-2116 (DOI:10.1021/la035812y).
9. K. Butter, P. Bomans, P. Frederik, G. Vroege and A. Philipse, *Nature Materials*, 2003, 2, 88-91 (DOI:10.1038/nmat811).
10. L. Donselaar, P. Frederik, P. Bomans, P. Buining, B. Humbel and A. Philipse, *J Magn Magn Mater*, 1999, 201, 58-61 (DOI:10.1016/S0304-8853(99)00118-3).

11. L. Baraban, D. Makarov, M. Albrecht, N. Rivier, P. Leiderer and A. Erbe, *Physical Review E*, 2008, 77, 031407 (DOI:10.1103/PhysRevE.77.031407).
12. L. Rovigatti, J. Russo and F. Sciortino, *Soft Matter*, 2012, 8, 6310-6319 (DOI:10.1039/c2sm25192b).
13. J. Weis, *Journal of Physics-Condensed Matter*, 2003, 15, S1471-S1495 (DOI:10.1088/0953-8984/15/15/311).
14. S. Klapp, *Journal of Physics-Condensed Matter*, 2005, 17, R525-R550 (DOI:10.1088/0953-8984/17/15/R02).
15. D. Levesque and J. Weis, *Physical Review E*, 1994, 49, 5131-5140 (DOI:10.1103/PhysRevE.49.5131).
16. J. Tavares, J. Weis and M. da Gama, *Physical Review E*, 1999, 59, 4388-4395 (DOI:10.1103/PhysRevE.59.4388).
17. P. Camp, J. Shelley and G. Patey, *Phys. Rev. Lett.*, 2000, 84, 115-118 (DOI:10.1103/PhysRevLett.84.115).
18. A. I. Abrikosov, S. Sacanna, A. P. Philipse and P. Linse, *Soft Matter*, 2013, 9, 8904-8913 (DOI:10.1039/c3sm27128e).
19. N. Mikuszeit, L. Baraban, E. Y. Vedmedenko, A. Erbe, P. Leiderer and R. Wiesendanger, *Physical Review B*, 2009, 80, 014402 (DOI:10.1103/PhysRevB.80.014402).
20. S. Kantorovich, R. Weeber, J. J. Cerda and C. Holm, *Soft Matter*, 2011, 7, 5217-5227 (DOI:10.1039/c1sm05186e).

21. M. Klinkigt, R. Weeber, S. Kantorovich and C. Holm, *Soft Matter*, 2013, 9, 3535-3546 (DOI:10.1039/c2sm27290c).
22. E. V. Novak, E. S. Pyanzina and S. S. Kantorovich, *Journal of Physics-Condensed Matter*, 2015, 27, 234102 (DOI:10.1088/0953-8984/27/23/234102).
23. A. B. Yener and S. H. L. Klapp, *Soft Matter*, 2016, 12, 2066-2075 (DOI:10.1039/c5sm02648b).
24. B. W. Kwaadgras, R. van Roij and M. Dijkstra, *J. Chem. Phys.*, 2014, 140, 154901 (DOI:10.1063/1.4870251).
25. V. Ballenegger and J. P. Hansen, *Mol. Phys.*, 2004, 102, 599-609 (DOI:10.1080/00268970410001675554).
26. J. N. Israelachvili, *Intermolecular and surface forces*, Academic Press, Burlington, MA, 2011.
27. S. Whitlam and P. L. Geissler, *J. Chem. Phys.*, 2007, 127, 154101 (DOI:10.1063/1.2790421).
28. K. Van Workum and J. Douglas, *Physical Review E*, 2006, 73, 031502 (DOI:10.1103/PhysRevE.73.031502).

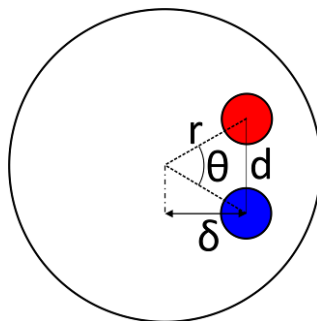


Figure 4.1. Model of the offset-dipole sphere used in this work. The large sphere represents the excluded volume of the particle and has a diameter of σ . The two smaller spheres represent the locations of the positive (red) and negative (blue) charges on the extended dipole. The charges do not, in actuality, have a physical size and are pictured here as spheres for clarity.

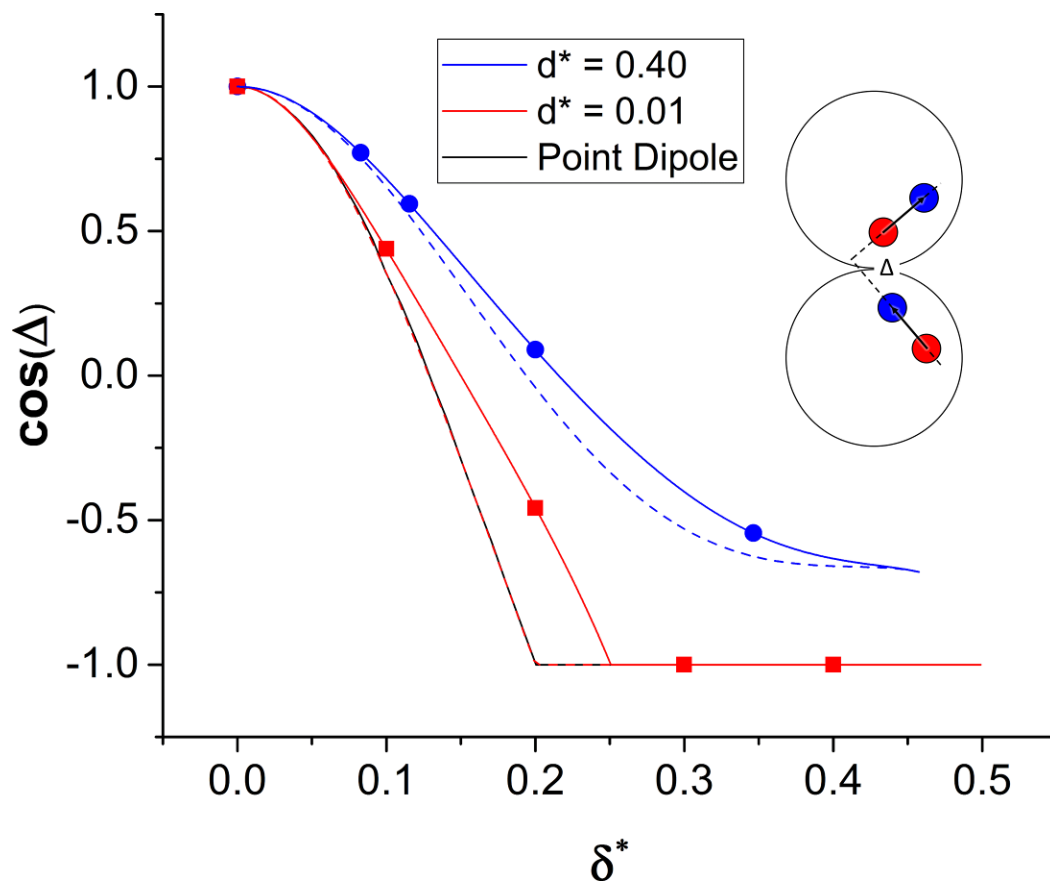


Figure 4.2. Cosine of the angle between two extended dipoles for two offset dipoles confined to the x-y plane at their minimum potential energy (ground state) configuration as a function of the displacement, δ^* . Lines represent minimization of the pair potential energy as a function of δ^* for either a point dipole (black)²³, Case 1 (red) and Case 2 (blue). Dashed lines are results for $k=0$ (Coulomb potential). Points are results from simulated annealing MC simulations.

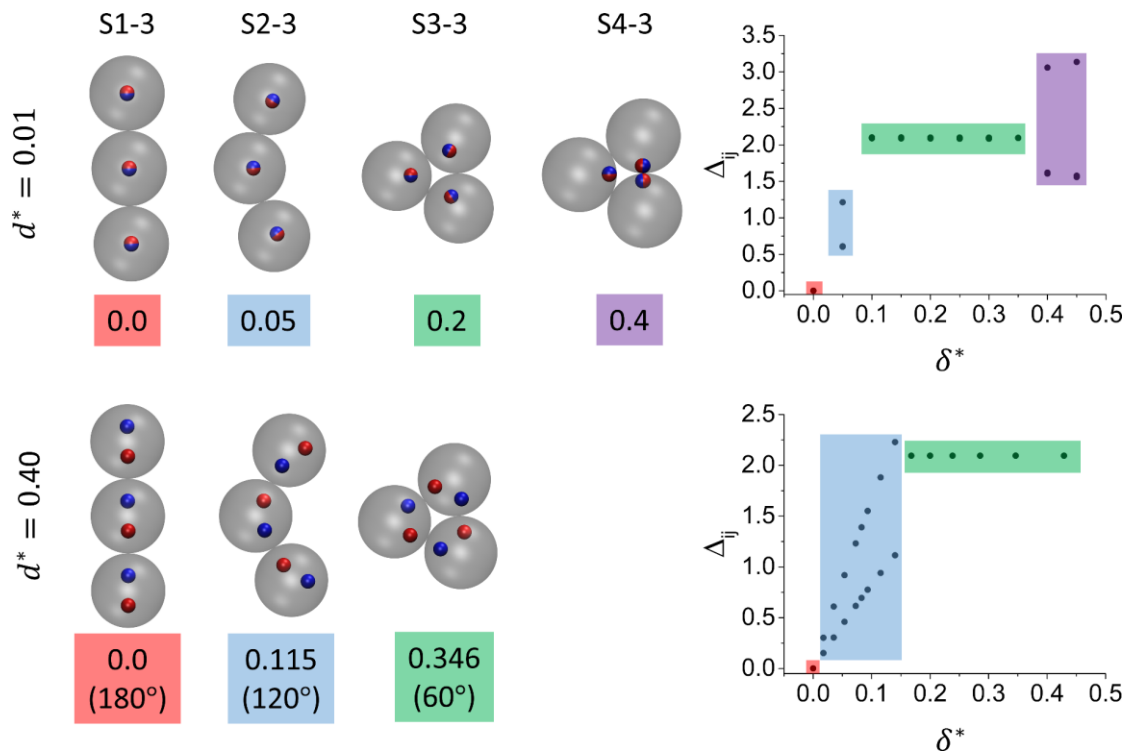


Figure 4.3. Ground state structures for systems of three particles for both Case 1 and Case 2. Images on the left show representative structures where the value below the image is δ^* for the particle and the numbers in parenthesis for Case 2 are the angle θ . The plots on the right display the Δ_{ij} for the three pairs of dipoles (Δ_{12} , Δ_{13} , Δ_{23}) as a function of δ^* . Colors on the right plots highlight regions where the corresponding structures on the left are the minimum energy structure.

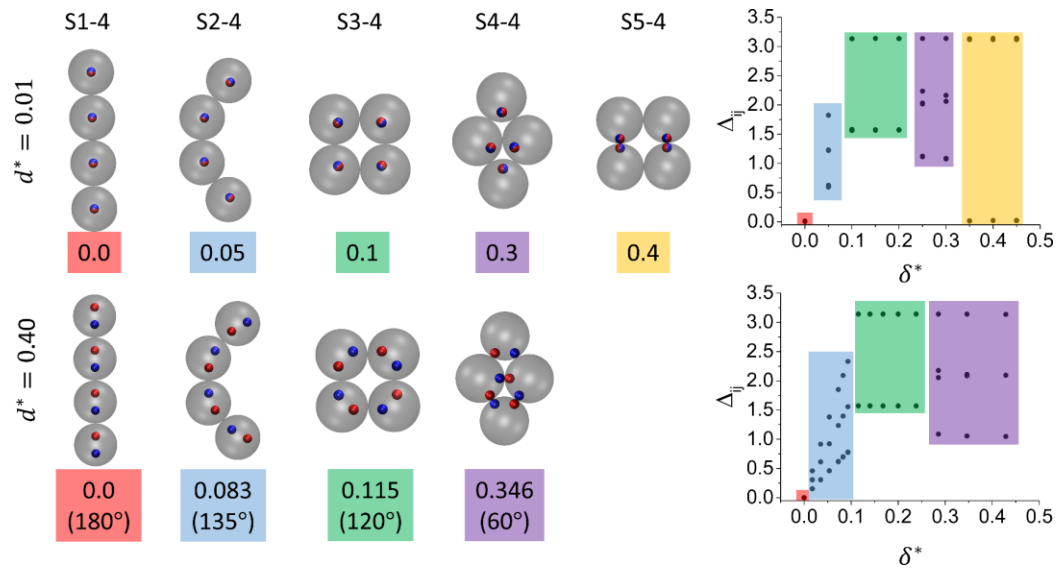


Figure 4.4 Ground state structures for systems of four particles for both Case 1 and Case 2. Images on the left show representative structures where the number below the image is the value of δ^* for the particle and the number in parenthesis for Case 2 is equal to θ . The plots on the right display the values of Δ_{ij} as a function of δ^* . Colors on the right plots highlight regions where the corresponding structures on the left are the minimum energy structure.

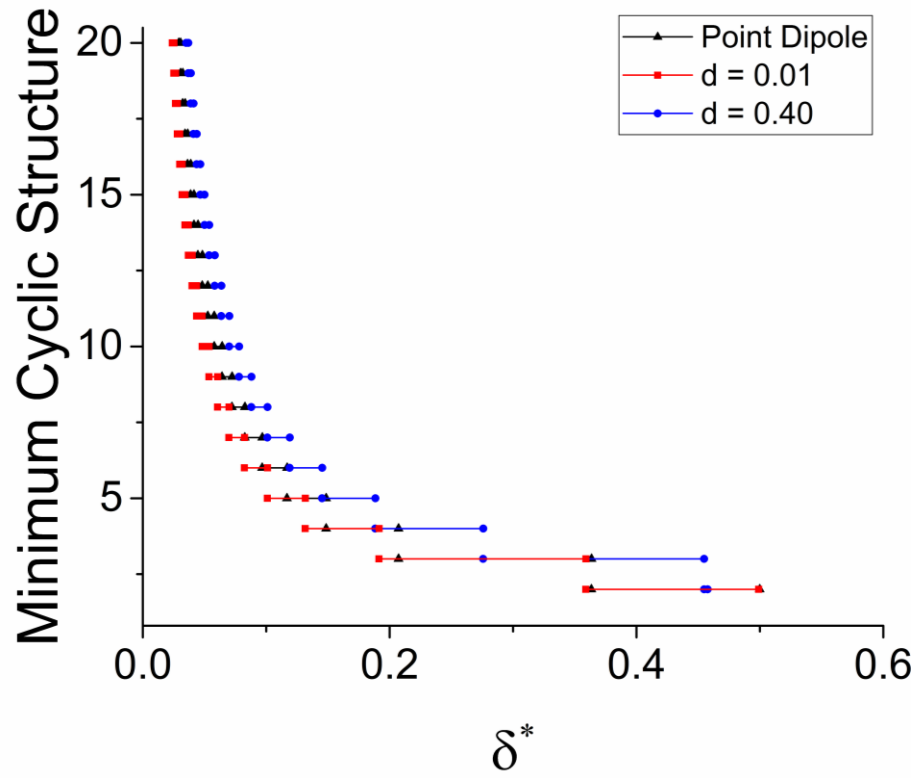


Figure 4.5. Plot showing the most stable cyclic structure as a function of the shift of the dipole, δ^* from the particle center, δ , for Case 1 and 2.

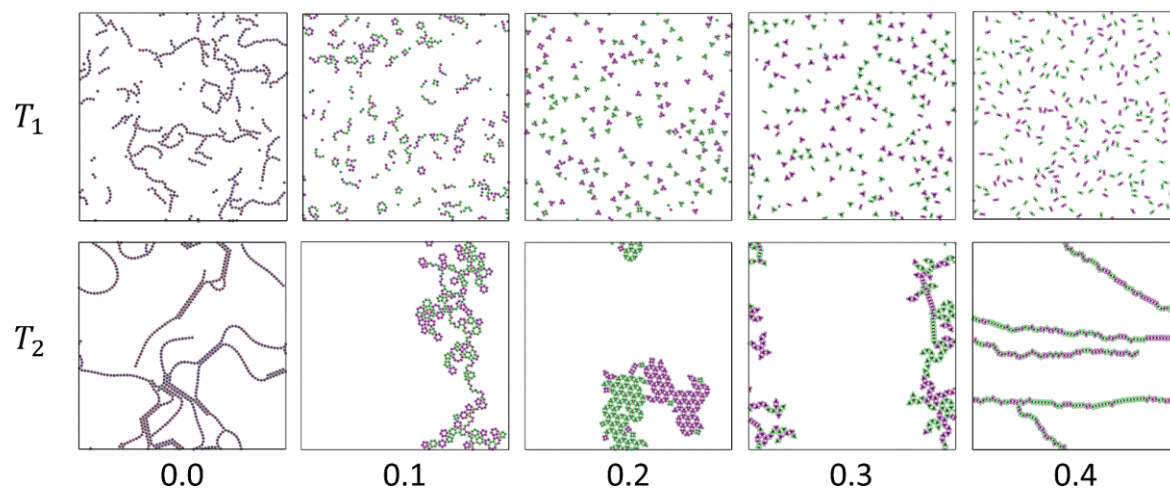


Figure 4.6. Snapshots of low temperature systems at $\varphi = 0.1$ for $d^* = 0.01$ systems. Green indicates one chirality while purple the other. Numbers indicate the value of δ^* . T_1 is a temperature below the polymerization transition but above the percolation transition and T_2 is a temperature below the percolation transition for each system.

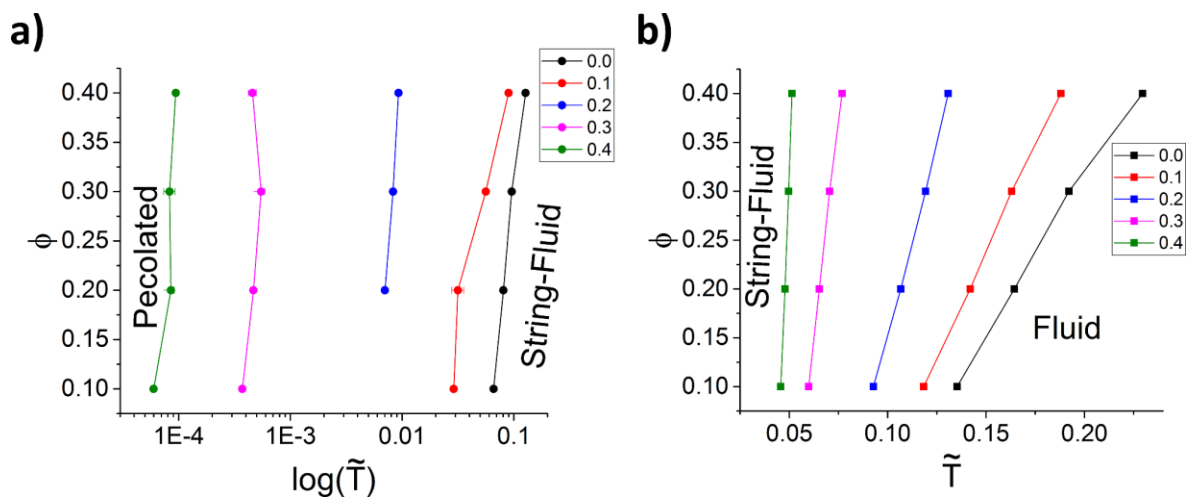


Figure 4.7. a) Percolation and b) polymerization transition lines as functions of \tilde{T} for Case 1. Numbers in the legends indicate the value of δ^* .

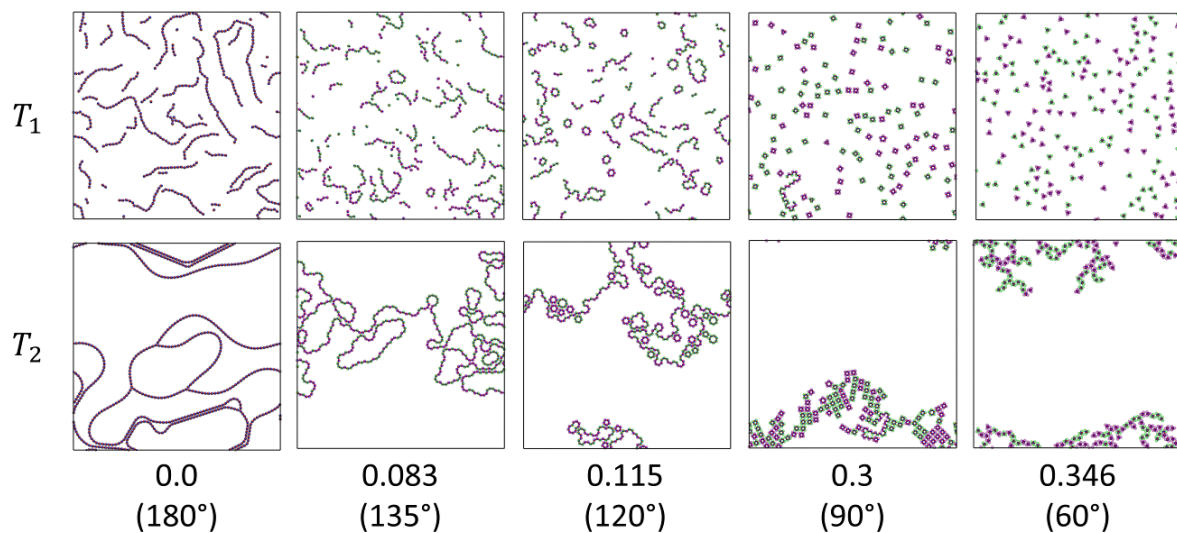


Figure 4.8. Snapshots of structures formed in finite temperature simulations using Case 2. T_1 is a temperature below the polymerization transition but above the percolation transition and T_2 is a temperature below percolation transition for each system.

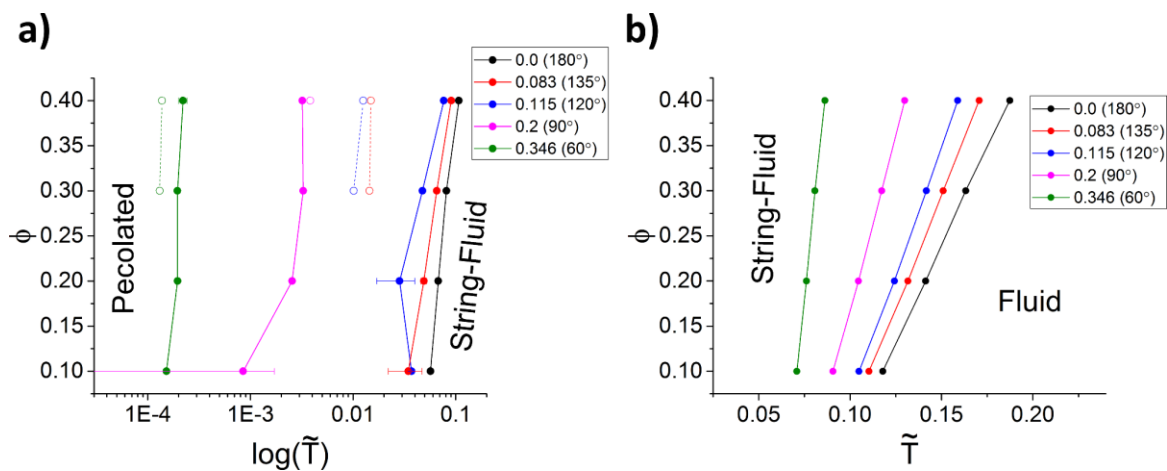


Figure 4.9. a) Percolation and b) polymerization transition lines as functions of \tilde{T} for Case 2. Numbers in the legends indicate the value of δ^* while those in the parenthesis indicate the value of θ . The open circles are the percolation transitions for the fused cyclic cluster simulations which are described later.

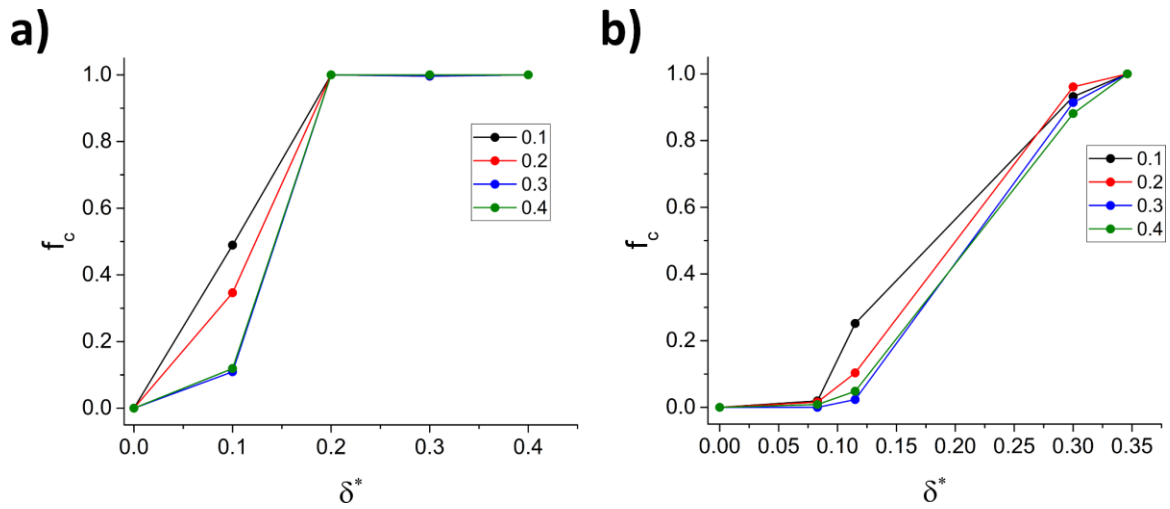


Figure 4.10. Fraction of particles that are in polygons, f_c , as a function of δ^* for a) Case 1 and b) Case 2. Numbers in the legends indicate the area fraction for each curve. These values were calculated for configurations at T_2 .

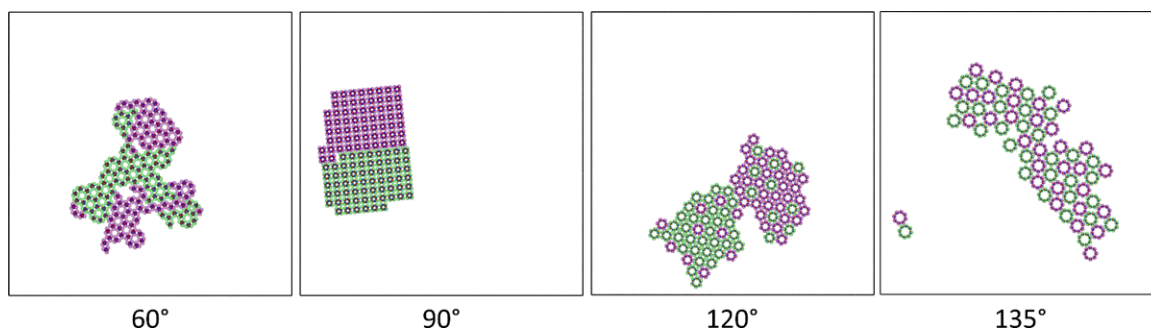


Figure 4.11. Structures formed from fused cyclic cluster simulations for particles with $d^* = 0.40$ at an area fraction of 0.1. Values below the images indicate the angle, θ , used in our model as shown in Figure 4.1.

CHAPTER 5

Capillary Bridging as a Tool for Assembling Discrete Clusters of Patchy Particles

Chapter 5 is a manuscript by Bhuvnesh Bharti, David M. Rutkowski, Koohee Han, Aakash Umesh Kumar, Carol K. Hall and Orlin D. Velev which was accepted by JACS. The author of this thesis performed the Monte Carlo simulations in this paper, none of the experimental work described was performed by the author of this thesis.

Capillary Bridging as a Tool for Assembling Discrete Clusters of Patchy Particles

Bhuvnesh Bharti^{a*}, David M. Rutkowski^a, Koohee Han^a, Aakash Umesh Kumar^a, Carol K. Hall^a and Orlin D. Velev^{a*}

^aDepartment of Chemical and Biomolecular Engineering, North Carolina State University, 911 Partners Way, Raleigh, North Carolina 27695, USA

Abstract

Janus and patchy particles are emerging as models for studying complex directed assembly patterns and as precursors of new structured materials and composites. Here we show how lipid induced capillary bridging could serve as a new and non-conventional method of assembling patchy particles into ordered structures. Iron oxide surface patches on latex microspheres were selectively wetted with liquid lipids, driving the particle assembly into 2D and 3D clusters via interparticle capillary bridge formation. The liquid phase of the bridges allows local reorganization of the particles within the clusters and assists in forming *true* equilibrium configurations. The temperature driven fluid-to-gel and gel-to-fluid phase transitions of the fatty acids within the bridge act as a thermal switch for cluster assembly and disassembly. By complementing the experiments with Monte-Carlo simulations we show that the equilibrium cluster morphology is determined by the patch characteristics, namely; their size, number, and shape. The study demonstrates the ability of capillary bridging as a versatile tool to assemble thermoresponsive clusters and aggregates. This method of binding particles is simple, robust and generic, and can be extended further to assemble particles with

non-spherical shapes and complex surface chemistries enabling the making of sophisticated colloidal molecules.

5.1 Introduction

Self-assembly of atoms, molecules, and particles is the origin of all physical mesoscopic matter.^{1,2} The properties of these materials are governed by the spatial organization and symmetry of the particle assemblies. The equilibrium morphology of the self-assembled state of these building blocks is determined by their packing efficiency (entropy) and interparticle interaction (enthalpy), but the lack of means of controlling these parameters hinders the fabrication of structures with complex functionality. In order to further extend the role of self-assembly, colloidal particles with directional pair-interactions have been proposed as precursors to generate ordered domains and clusters with unusual patterns and symmetry.³⁻⁷ The key parameters determining the assembled state of these particles are the number of surface interaction sites (patches), surface patch area, the magnitude of interaction potential, packing efficiency, and particle shape.^{2,8-13} The interparticle interactions play a major role in driving and governing the assembly process. To assemble ordered domains and structures, these interactions must allow particle-to-particle re-organization so as to inhibit the persistence of kinetically trapped configurations, and attain a thermodynamic minimum energy state.

The binding forces used in colloidal self-assembly include electrostatic and van der Waals (DLVO type), hydrophobic, and lock-and-key type of interactions (DNA, and other molecular recognition binding).¹⁴⁻¹⁹ One non-conventional method of binding particles is through the formation of capillary bridges. In this case, particles wetted with a liquid that come in surface contact with each other attain an interconnected state, where the wetting liquid forms interparticle capillary bridges.²⁰⁻²³ The origin of capillary attraction is the

interfacial tension between the dispersing liquid and surface wetting liquid. This is in contrast with the molecular mechanism of hydrophobic attraction, where the entropy gain due to loss of water molecules during the binding process is the driving force. The capillary forces are spatially isotropic and, much like oppositely charged particle-pairs, yield random aggregates.^{20,24} A directional aspect to the interactions can be introduced by spatially defining the interaction spots on a particle's surface, i.e. discretizing the interaction domain and hence introducing spatial restriction in the interactions.²⁵ For example, silica/gold Janus particles in water/2,6-lutidine binary liquid mixtures exhibit temperature-controlled wetting of the particles.²⁶ In the 2-phase region of the binary liquid, water preferentially wets the silica hemisphere and results into the formation of capillary bridged 2D clusters. These self-assemblies exist within a narrow temperature range of 1-2 °C.²⁶ Beyond this temperature range, macroscopic phase separation of the two liquids occurs, resulting in the formation of particle-covered Pickering emulsion droplets.^{27,28}

In this article we present an approach for liquid lipid-based capillary binding of patchy particles into colloidal clusters over a wide temperature range with no macroscopic phase separation or emulsion formation. The capillary binding enables completely reversible assembly-disassembly of clusters during capillary bridge freezing and melting cycles. Both experimentally and by using Monte-Carlo simulations we show that the near-equilibrium morphology of the colloidal clusters is governed by the physical properties of the surface patches on the particles.

We induce direct condensation of surface wetting agent (lipid) from bulk onto the surface patch of a microparticle to create interaction sites. This approach stems from our

recent report on the assembly of iron oxide nanoparticles into networked filaments via capillarity-mediated binding between liquid-lipid shells on the particles.²² The strong affinity of the fatty acids for iron oxide²⁹ leads to surface wetting and formation of a condensed liquid-lipid shell selectively on the patch. The spatial overlap of these liquid shells on the patches leads to the formation of capillary bridges between the iron oxide nanoparticles.³⁰

5.2 MC Simulation Details

We chose to simulate in 3D under the effects of gravity rather than to use purely 2D because the experimental structures were essentially 3D in nature, which 2D simulations would not be able to mimic. NVT Monte Carlo simulations were performed on 100 Janus spheres in a cubic simulation box under the effect of gravity at an area fraction of 0.10, where the area fraction is the sum of the circular projections of the spheres on the x-y plane divided by the area of the x-y plane. (Particle overlap is minimal.) Small spheres on the surface of the particles were assigned to be either type B or type A depending on their position with respect to a plane which is perpendicular to the x-axis and located at $x = d$ in a coordinate system centered on the Janus sphere center. All small spheres to the right of this plane (i.e., have larger x-coordinates than d) are type B while all points to the left (i.e. have smaller x-coordinates than d) are type A. Points having an x-coordinate of exactly d alternate between type B and type A. Clusters in our simulations were defined to exist when two particles have a net attractive interaction between them.

5.2.1 Monodisperse interaction potential

These simulations focused on Janus particles which were monodisperse, had a diameter of 4 μm , and had a density of 1.05 g/cm^3 in a solution with a density of 1.0 g/cm^3 . We varied the location of the plane used to define the types of surface beads so that the area of the patch consisting of type B relative to the area of the entire particle varied from 0.10 to 0.50. The B - B interaction in this system was modeled as a square well with width 0.3σ , where σ is equal to the diameter of a 4 μm particle, and depth $1.25\text{e-}22$ J. This value was chosen by iteratively changing the interaction energies in the system at constant temperature until the final aggregates resembled those seen in experiment at the same conditions. We chose this value as our scaling energy, ϵ , for all simulations and consequently our reduced well depth for the monodisperse systems was equal to 1.0. The repulsive interactions between A - A and A - B points were modeled with a single square shoulder of the same magnitude and interaction range. These particles all had 252 small spheres on the surface which were defined to be either type A or type B according to the procedure outlined in the previous subsection. Each particle experienced a drop in reduced gravitational potential energy of 525.6 ($6.57\text{e-}20$ J) per particle diameter traveled in the negative z -direction, calculated from the particle's density and the buoyancy of the particle as a function of the particle and solution densities. After allowing the system to randomize at the bottom of the box with interactions between particles turned off, we instantaneously turned on the interactions at a temperature of 298K and ran the system until the particles equilibrated.

5.2.2 Interaction potentials for a mixture of 4 μm and 2 μm spheres

Simulations were also performed on a binary, 50:50 mixture of Janus particles of different sizes. The well depth and square shoulder height for the interaction between these two particles needed to be increased compared to the previously described monodisperse system to a magnitude of 2.0 in energy reduced by the monodisperse interaction energy in order to see structures similar to experiment. The width of the square well and shoulder was kept at 0.3σ for all interactions, where σ is the diameter of a 4 μm particle. The same number (252 particles) of smaller spheres was used to coat the surface of the 4 μm while a reduced number (60 particles) was used for the 2 μm particles in accordance with the approximate ratio of the surface area between the two different sphere sizes. The 2 μm particles experienced a reduced gravitational force compared to the larger 4 μm due to their smaller size; each 2 μm size particle had a drop in reduced gravitational potential energy of 65.68 (8.21e-21 J) per 2 μm traveled in the negative z-direction. The 4 μm in this section had the same gravitational potential as in the prior, monodisperse simulations. The simulations were carried out using the same procedure as for the monodisperse case.

5.3 Results and Discussion

This report is based on the use of 4 μm latex microspheres with iron oxide surface patches as building blocks for assembling 2D and 3D clusters. The surface patches were formed on negatively charged polystyrene microbeads by the previously reported technique of metal (here iron) vapor deposition.³¹ The iron patch size, shape, and orientation were fine-tuned by changing the angle of the deposition. Here we define the fractional patch area (f) as

a measure of the particle's patchiness (or Janus balance). The value of f was determined by analyzing scanning electron microscope (SEM) images (Figure 5.6) where $f = a_{patch}/a_{total}$, with a_{patch} and a_{total} are equal to the iron patch area and the total surface area of the particle, respectively. In order to minimize residual magnetisation and van der Waals attraction, the layer of iron metal deposited on the particles was only 5 nm thick.³² It has been previously shown that upon transferring the iron patched particles into aqueous dispersion, a layer of iron oxide spontaneously forms on the patch.³³ A subsequent addition of fatty acid amine salts at pH 9.5 results in selective wetting of the iron oxide patch with a liquid lipid layer, which promotes the formation of interparticle capillary bridges (Figure 5.1a).

The self-assembly of patchy colloids is governed by the surface interaction between the particles. In our case of metallo-dielectric patchy particles, we determine the surface potential of the sulfonate functionalized polymer hemisphere by measuring the electrophoretic mobility of unpatched polystyrene microbeads. The surface potential for the metal patch at pH 9.5 was determined by measuring the zeta-potential of an iron oxide coated flat substrate using tracer particles (Figure 5.7). The surface potentials were measured both in water and in fatty acid salt solution. The net zeta potentials of all surfaces were found to be in the range -20 mV and -50 mV, hence the surfaces were electrostatically repulsive (Figure 5.8, Figure 5.1b).

5.3.1 Liquid-lipid driven particle clustering

In a typical experiment, patchy microspheres were dispersed in aqueous fatty acid amine salt solution and transferred into a sealed microchamber. The particles were allowed to

self-assemble at a pre-set temperature and the kinetics of the assembly process was monitored using an Olympus BX-61 microscope. Initially, only single particles or low aggregation number clusters were observed. At a fixed particle concentration, the mean cluster-aggregation number increases over time due to increasing probability of patch-to-patch encounter, resulting in capillary bridged clusters (Figure 5.9). The gravitational force acting on the particles restricted the colloidal clusters to the bottom of the assembly chamber. The near-equilibrium structures (after 9 hours) formed by the lipid-wetted Janus particles ($f=0.5$) are shown in Figure 5.2. The micrograph shows co-existence of 2D planar and 3D structures. We investigated the specific case of low particle number density (< 2 vol. %) where discrete clusters were formed and no network or lattice formation was observed.

The capillary interaction driving microparticle cluster formation is unique in several fundamental aspects. When the lipid-wetted surface patches approach each other, there is an initial electrostatic repulsion followed by a short range square-well-like attraction at even closer separations (Figure 5.1b).^{30,34} This attraction has been attributed to the formation of capillary bridging between the liquid-coated particles/patches.^{30,35} In the present case of lipid-wetted particles, the capillary bridging dominates other secondary interactions (van der Waals, electrostatic etc.) and drives the self-assembly process. The capillary binding forces are known to be orders of magnitude stronger than other conventional forces (electrostatic, van der Waals etc.).³⁶ Despite the strong attraction, we observed that the liquid nature of the bridges allows high reconfigurability of the interparticle ‘bonds’. In our experiments we commonly see that when two independent clusters coalesce, the individual particles within the parent cluster reorient to accommodate the changed aggregation number. The ability of a

liquid bridges to realign the bound particles is the key to attain true equilibrium morphology of the clusters. Here the local stresses within a kinetically trapped cluster are dissipated by particle-to-particle rollover and reorientation, allowing to achieve a minimum energy state. This assembly-reassembly of patchy particles is different from the self-assembly driven by strong hydrophobic, electrostatic, or van der Waals interactions, where such reconfigurations are not expected.^{37,38} A decrease in the magnitude of the net interparticle interaction (\sim thermal energy) also results into structural reconfigurability³⁹. In the present case of strong capillary binding (much larger than the thermal energy),²² the reorientation of the linked particles is solely due to liquid fatty acid.

5.3.2 Thermal switching of clusters

Fatty acid aqueous dispersions have the ability to spontaneously transition between fluid and gel phases. The corresponding phase transition temperature (T_P) depends upon the number of carbon atoms in the fatty acid backbone and the identity of the dispersing counterion.²² The effect of the fatty acid phase change on the self-assembly of Janus particles was investigated using ethanol amine salts of dodecanoic acid ($C_{11}H_{23}COOH$, $T_P \sim 8^\circ C$) and hexadecanoic acid ($C_{15}H_{31}COOH$, $T_P \sim 40^\circ C$).²² The data for the temperature dependence of the fraction of particles assembled (non-singlet particles) in $C_{11}H_{23}COOH$ and $C_{15}H_{31}COOH$ are shown in Figure 5.3a. For $C_{11}H_{23}COOH$, the Janus particles spontaneously assembled into clusters below $40^\circ C$, whereas no assembly was observed for $C_{15}H_{31}COOH$ in this temperature range. In the case of $C_{15}H_{23}COOH$, the assembly was observed only above the corresponding phase transition temperature ($40^\circ C$). This observation indicates that the

fluidity of the fatty acid is a prerequisite for the assembly process. We believe that a lipid surface patch is ‘sticky’ only when the adsorbed lipid layer is in the fluid state, which further leads to capillary bridging and particle assembly. The gel-to-fluid and fluid-to-gel transformation of lipids is a first order phase transition, and hence the particles can be thermally triggered to adopt either a fully assembled or a disassembled state (Figure 5.3a).

The observed dependence of the capillary bridge formation on the lipid phase transition leads to an intriguing question of what happens to a cluster when the capillary bridges ‘freeze’. This was investigated for clusters formed by $C_{15}H_{23}COOH$ at $50\text{ }^{\circ}C$ ($> T_P$), by gradually lowering the temperature to $30\text{ }^{\circ}C$. We found that the pre-assembled clusters disintegrate upon decreasing the temperature below the corresponding phase transition temperature (Figures 5.3b and c). The cooling results in lipid gelation, making the interparticle capillary bridges brittle, which causes their subsequent fracture.²² The lipid gelation might also result in an effective dewetting of the surface patch and the observed disassembly. Further studies would enable complete understanding of the impact of the lipid phase behavior on the patch and on the capillary bridging.

5.3.3 Monte Carlo simulations of patch particle clustering

The interparticle interactions involved in the capillary bridging and cluster formation could be affected in a non-trivial way by several control parameters, hence a concurrent theoretical/simulation approach is necessary to better understand the process. We developed a simple Monte Carlo (MC) simulation model to interpret our experimental observations. Similar models have been used previously to predict the self-assembly of Janus particles.⁴⁰

Each individual particle was modeled by a set of 252 evenly spaced domains covering the surface of a central spherical core.⁴¹ Based on our experimental findings (Figure 5.1b), the surface domains on the particle were divided into two types representing (1) charged polymer surface – type *A* or (2) lipid coated surface patch – type *B*. The two types of domains cover a central core such that the resulting particle contains a single patch of type *B* with fractional surface coverage f (Figure 5.4a inset). In MC simulations the fractional patch area is defined to be the fraction of *A* domains on a particle. The capillary bridging attractive interaction between *B* – *B* domains was approximated by a short range attractive square-well potential with well-width of 0.3σ , where σ is the diameter of the patchy particle, and well-depth 1.0ϵ , where ϵ is the interaction energy in arbitrary units. The corresponding minimum energy between a pair of colloidal particles varied between 270ϵ and 590ϵ , depending on the value of f . The simulations were performed at $T^* = kT/\epsilon = 32.9$, which corresponds to a real temperature of 298 K. The *A*–*A*, and *A*–*B* type interactions were modeled by square shoulders of the same width and magnitude as the square well describing the type *B*–*B* interactions. The overall interaction between such patchy spheres was the sum of the *A*–*A*, *A*–*B* and *B*–*B* interactions. In a typical simulation run, 100 particles were randomly placed in a cubic simulation box of approximately 28σ edge length. The simulations were performed with periodic boundary conditions in the x and y directions and a hard wall boundary in the z direction. In our experiments, the gravitational force restricts the clusters to the bottom of the assembly chamber. To account for this effect in our simulation, we introduce an additional gravitational potential acting on the particle clusters in the z -direction of the simulation box. Because of this quasi 2D character of our system, we specify the particle area fraction for the

x - y plane projections of the Janus spheres (instead of the spheres' total volume fraction) and set it to 0.10. The near-equilibrium assemblies were formed in our simulations by minimizing the ensemble energy. Further details on the simulation procedure are provided in the section 5.2.

The assemblies formed by patchy particles (with $f = 0.15$) in our MC simulations and experiments are shown in Figure 5.4a and b, respectively. Both the simulations and experiments show the presence of low aggregation number 2D clusters. Here we investigate the change in the cluster morphology upon increasing the patch area. In our MC simulation, the surface patch area can be increased by increasing the relative population of B domains on a particle (Figure 5.4c, d, and e), whereas in experiments it can be increased by changing the relative angle of metal vapor deposition onto the particles.³¹ Both in experiments and MC simulations, we find an increase in the fraction of particles assembled with increasing surface patch area; the experimental observations (Figure 5.4f, open squares) overlay the MC simulation findings (Figure 5.4f, filled circles, Figure 5.10). In addition, we find that the simulated assembly kinetics of different patch sized particles is qualitatively similar to that in our experiments (Figure 5.11). The simulations offer a facile fundamental tool to determine the clustering pathways followed by particles with different patch characteristics, and to understand why specific cluster morphologies arise at different physical conditions. They help guide the design of colloidal building blocks that will self-assemble into clusters of unusual morphology, which is non-trivial to establish by experiments alone. The simulations also show that the interactions among the experimental particles can be approximated reasonably well by a patchy sphere model with simple short-range interactions. Because the

simulations describe the experimental assembly quite well, they could be used to explore patch configurations that have not yet been fabricated.

5.3.4 Capillary bridging of complex particles and their mixtures

The potential of the method to achieve complexity in the interactions and the assembled cluster morphologies can be illustrated by using multi-disperse building block particles or by changing the patch morphology. A few representative clusters formed by a mixture of 4 μm and 2 μm Janus particles are shown in Figure 5.5a-c. The particles assembled into mixed clusters composed of both small (diameter $\sim 2 \mu\text{m}$) and large (diameter $\sim 4 \mu\text{m}$) Janus particles. A wide variety of self-assembled structures were observed, including bi-particle dimers and trimers (Figure 5.5a); a hexamer with one large and five small particles (Figure 5.5b); and small-particle rings around large particle dimers (Figure 5.5c). We believe that morphology of the assembled clusters is determined by the minimization of the net balance of the repulsive electrostatic and attractive capillary interactions on a particle within the clusters. The range and absolute magnitude of the interactions will play a key role in guiding the self-assembly process and the near-equilibrium structures. The capillary bridging allows local reorganization of the bound particles and hence favors the maximization of patch-to-patch contact area within a cluster (Fig. 5.12). This reorganization of particles stems from the minimization of capillary binding energy by immediate rearrangement of the interparticle bridges. This is in contrast to the case of strong electrostatic and other conventional forces that bind the particles into clusters, where such rearrangements and corresponding assemblies are rarely observed.³⁸ Here again, our MC

simulations correctly predict the assembly of the complex structures in the experiments (Figure 5.5a-c insets).

The shape and number of ‘sticky-patches’ on a particle surface greatly influence the equilibrium morphology of self-assembled clusters. We illustrate this by introducing two distinct iron oxide patches onto the 4 μm particles by selective metal vapor deposition. Unlike previous studies where the patches were located diagonally opposite each other on the surface of particles,⁴² the triangular patches are introduced adjacent to each other (SEM, Figure 5.6). Experimental images of clusters formed by these double-patched particles are shown in Figure 5.5d-f. Here the self-assemblies formed both in experiment and in MC simulation (Figure 5.5d-f, Figure 5.12b) were limited to 2D, with spatially loose or open clusters. The formation of 2D clusters by the double patched particles can be attributed to the low surface fraction patch area, which restricts the formation of 3D assemblies. The two discrete patches on the surface induce an additional directionality in the assembly process that favors the formation of elongated assemblies, reminiscent of co-polymerization (Figure 5.5f, Figure 5.12).⁴³ Many more types of multi-patchy assemblies can be realized by capillary binding of engineered particles with complex shapes and surface patch characteristics. Liquid bridging facilitate new pathways to self-assemble micro- and nanoscale building blocks into clusters of unusual symmetries and morphologies.

5.4 Conclusions

In conclusion, we found that the thermoresponsive self-assembly of microparticles can be directed by selective surface wetting and formation of capillary bridges between the

patches on the particles. The wetting of the patches induces a short-range attractive potential, which guides the assembly of particles into clusters of desired morphologies. The minimization of the capillary binding energy by spatially reconfiguring the flexible bridges drives the cluster reassembly and growth. We believe that the reconfigurability of particles linked via capillary bridge will assist in assembling equilibrium states of faceted particles, which otherwise are restricted to dissipate local stresses because of the anisotropic shape and non-reconfigurable interparticle binding. The liquid characteristic of capillary bridging driven assembly may also result over time in defect-free colloidal clusters and lattices. In other words, the initial defects can be self-repaired by particle reorganization enabled by the liquid based capillary binding. We believe that this method of liquid lipid bridging opens up new opportunities to assemble clusters, networks, and lattices of anisotropic colloidal building blocks with of unusual physical, chemical, and optical properties.

5.5 Acknowledgments

The financial support by the Research Triangle NSF-MRSEC on Programmable Soft Matter (DMR-1121107) and (CBET-1604116) is gratefully acknowledged. We thank Sangchul Roh for assistance with SEM measurements.

5.6 References

1. Whitesides, G. M.; Grzybowski, B. *Science* 2002, *295*, 2418.
2. Zhang, J.; Luijten, E.; Granick, S. *Annu. Rev. Phys. Chem.* 2015, *66*, 581.
3. Walther, A.; Müller, A. H. E. *Chem. Rev.* 2013, *113*, 5194.
4. Sacanna, S.; Rossi, L.; Pine, D. J. *J. Am. Chem. Soc.* 2012, *134*, 6112.
5. Zhang; Glotzer, S. C. *Nano Lett.* 2004, *4*, 1407.
6. Chen, Q.; Bae, S. C.; Granick, S. *J. Am. Chem. Soc.* 2012, *134*, 11080.
7. Bharti, B.; Velev, O. D. *Langmuir* 2015, *31*, 7897.
8. Chen, Q.; Yan, J.; Zhang, J.; Bae, S. C.; Granick, S. *Langmuir* 2012, *28*, 13555.
9. Sun, Y.; Chen, M.; Zhou, S.; Hu, J.; Wu, L. *ACS Nano* 2015, *9*, 12513.
10. (Lenis, J.; Razavi, S.; Cao, K. D.; Lin, B.; Lee, K. Y. C.; Tu, R. S.; Kretzschmar, I. *J. Am. Chem. Soc.* 2015, *137*, 15370.
11. Cavallaro, M.; Botto, L.; Lewandowski, E. P.; Wang, M.; Stebe, K. J. *Proc. Natl. Acad. Sci.* 2011, *108*, 20923.
12. Botto, L.; Lewandowski, E. P.; Cavallaro, M.; Stebe, K. J. *Soft Matter* 2012, *8*, 9957.
13. Lewandowski, E. P.; Cavallaro, M.; Botto, L.; Bernate, J. C.; Garbin, V.; Stebe, K. J. *Langmuir* 2010, *26*, 15142.
14. Zhou, Y.; Wang, D.; Huang, S.; Auernhammer, G.; He, Y.; Butt, H.-J.; Wu, S. *Chem. Commun.* 2015, *51*, 2725.
15. Wang, Y.; Wang, Y.; Zheng, X.; Ducrot, É.; Yodh, J. S.; Weck, M.; Pine, D. J. *Nat. Commun.* 2015, *6*, 7253.
16. McGinley, J. T.; Jenkins, I.; Sinno, T.; Crocker, J. C. *Soft Matter* 2013, *9*, 9119.

17. Rogers, W. B.; Manoharan, V. N. *Science* 2015, 347, 639.
18. Jones, M. R.; Seeman, N. C.; Mirkin, C. A. *Science* 2015, 347, 1260901.
19. Chen, Q.; Whitmer, J. K.; Jiang, S.; Bae, S. C.; Luijten, E.; Granick, S. *Science* 2011, 331, 199.
20. Koos, E.; Willenbacher, N. *Science* 2011, 331, 897.
21. Butt, H.-J.; Kappl, M. *Adv. Colloid Interface Sci.* 2009, 146, 48.
22. Bharti, B.; Fameau, A.-L.; Rubinstein, M.; Velev, O. D. *Nat. Mater.* 2015, 14, 1104.
23. Bowden, N.; Choi, I. S.; Grzybowski, B. A.; Whitesides, G. M.; Street, O. *J. Am. Chem. Soc.* 1999, 121, 5373.
24. Bharti, B.; Findenegg, G. H.; Velev, O. D. *Sci. Rep.* 2012, 2, 1004.
25. Lipowsky, R. *Curr. Opin. Colloid Interface Sci.* 2001, 6, 40.
26. Yu, C.; Zhang, J.; Granick, S. *Angew. Chem. Int. Ed.* 2014, 53, 4364.
27. Velev, O. D.; Furusawa, K.; Nagayama, K. *Langmuir* 1996, 12, 2374.
28. Dinsmore, a D.; Hsu, M. F.; Nikolaides, M. G.; Marquez, M.; Bausch, A. R.; Weitz, D. A. *Science* 2002, 298, 1006.
29. Chernyshova, I. V; Ponnurangam, S.; Somasundaran, P. *Langmuir* 2011, 27, 10007.
30. Bharti, B.; Fameau, A.-L.; Velev, O. D. *Faraday Discuss.* 2015, 181, 437.
31. Pawar, A. B.; Kretzschmar, I. *Macromol. Rapid Commun.* 2010, 31, 150.
32. Shemi, O.; Solomon, M. J. *Langmuir* 2014, 30, 15408.
33. Ren, B.; Ruditskiy, A.; Song, J. H. K.; Kretzschmar, I. *Langmuir* 2012, 28, 1149.
34. Zemb, T.; Kunz, W. *Curr. Opin. Colloid Interface Sci.* 2016, 22, 113.
35. Hijnen, N.; Clegg, P. S. *Langmuir* 2014, 30, 5763.

36. Min, Y.; Akbulut, M.; Kristiansen, K.; Golan, Y.; Israelachvili, J. *Nat. Mater.* 2008, 7, 527.
37. Chandler, D. *Nature* 2005, 437, 640.
38. Wang, H.; Hansen, M. B.; Löwik, D. W. P. M.; van Hest, J. C. M.; Li, Y.; Jansen, J. A.; Leeuwenburgh, S. C. G. *Adv. Mater.* 2011, 23, H119.
39. Walker, D. A.; Browne, K. P.; Kovalczyk, B.; Grzybowski, B. A. *Angew. Chemie - Int. Ed.* 2010, 49, 6760.
40. Liang, H.; Cacciuto, A.; Luijter, E.; Granick, S. *Nano Lett.* 2006, 6, 2510.
41. Hardin, R. H.; Sloane, N. J. A.; Smith, W. D. Tables of Spherical Codes with Icosahedral Symmetry <http://neilsloane.com/icosahedral.codes/>.
42. Mao, X.; Chen, Q.; Granick, S. *Nat. Mater.* 2013, 12, 217.
43. Liu, K.; Nie, Z.; Zhao, N.; Li, W.; Rubinstein, M.; Kumacheva, E. *Science* 2010, 329, 197.

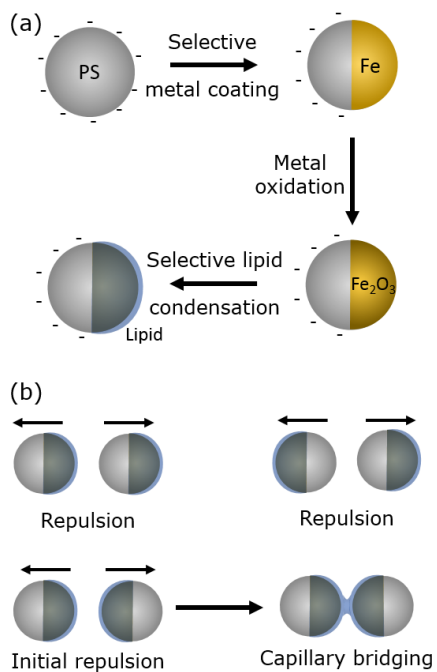


Figure 5.1. (a) A schematic summarizing the general methodology for fabricating lipid patched polystyrene (PS) microspheres. (b) Interactions between all three surface-pairs of the patchy microparticle. Here the thickness of the liquid fatty acid layer and particle size are not to scale.

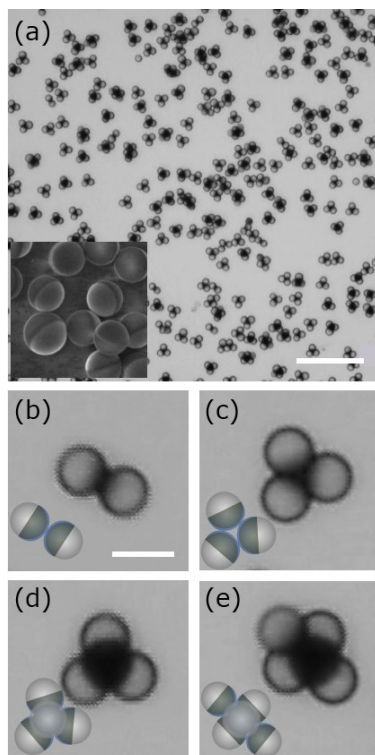


Figure 5.2. (a) Optical micrographs illustrating the self-assembly of lipid-wetted Janus particles into ordered colloidal clusters in aqueous dispersion. The inset shows an SEM image of the Janus particles before assembly in the dried state. (b-e) Examples of 2D and 3D clusters formed by capillary binding of the microspheres. Scale bar in (a) 50 μm and (b) 5 μm .

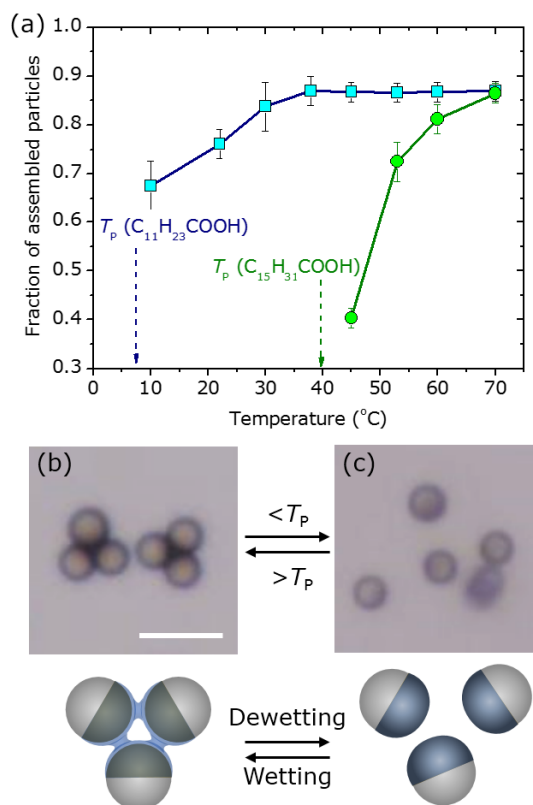


Figure 5.3. (a) The fraction of Janus particles self-assembled into clusters at different temperatures for ethanolamine salts of n -dodecanoic acid (squares) and n -hexadecanoic acid (circles). The vertical lines indicate the fluid-to-gel phase transition temperature (T_p) of the fatty acids on iron oxide surfaces. (b) and (c) The clusters disassembled upon decreasing the temperature below the fluid-to-gel phase transition of the fatty acid, i.e. when the liquid in the capillary bridge freezes. At temperature $T < T_p$, the fraction of assembled particles remains negligibly small. The corresponding schematics illustrate thermally reversible capillary bridge formation and rupturing. Scale bar in (b) 10 μ m.

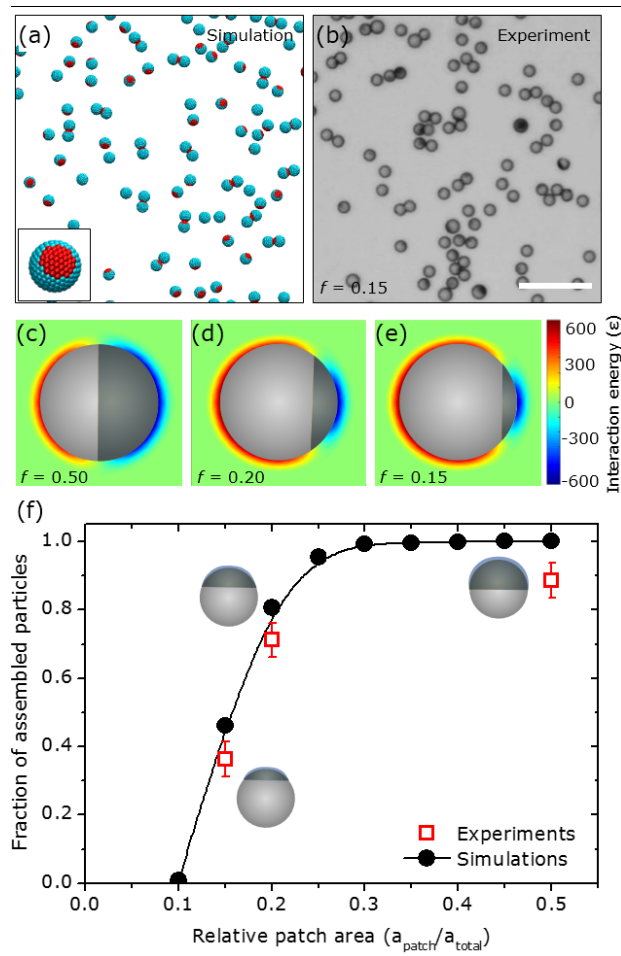


Figure 5.4. (a) Self-assemblies formed by the patchy particles ($f = 0.15$) in Monte Carlo simulations of the capillary assembly process. The inset shows an individual particle unit formed by distributing 252 domains on a central core. (b) Micrograph of patchy microspheres with fractional patch area of 0.15 assembled into low aggregation number clusters. (c-e) Surface interaction energy map for different patch sized particles ($f = 0.50$, 0.20, and 0.15). The attractive interaction between the lipid coated patches was modeled on the basis of a square-well attractive potential. (f) The increase in the fraction of assembled particles upon increasing the relative patch area (f) in simulations (filled circles) and experiments (open squares). Scale bar in (b) 50 μm .

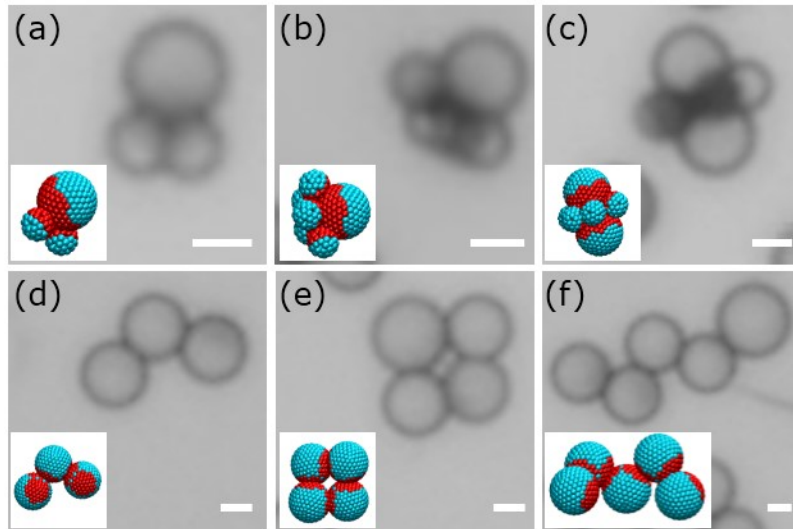


Figure 5.5. (a-c) Micrographs of the assemblies formed by a mixture of 4 μm and 2 μm Janus particles. (d-f) Capillary bridged self-assemblies formed by double-patched microspheres. The insets in the frames are the clusters observed in corresponding Monte Carlo simulations. Scale bar in each image is 2 μm .

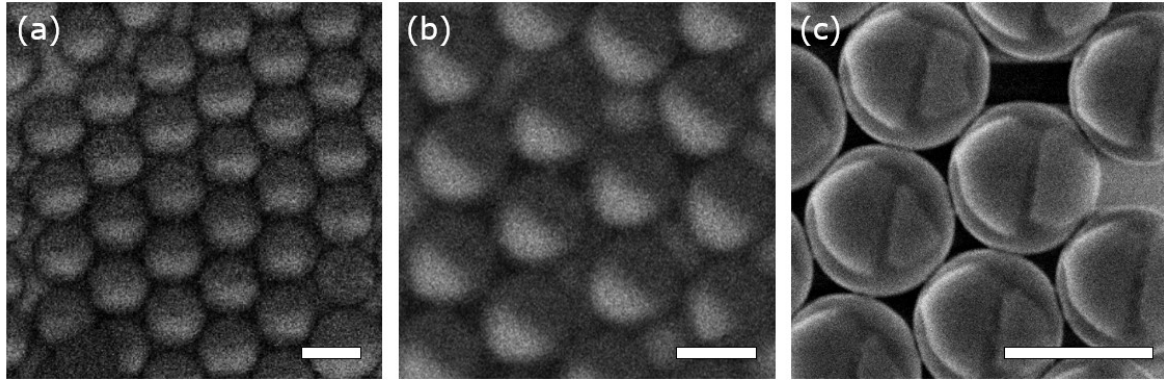


Figure 5.6. SEM image of the single patched particles with relative surface patch area ' f ' (a) 0.2; and (b) $f = 0.15$. The value of fractional patch area (light grey region on the particles) was estimated by analyzing the micrographs using ImageJ software package. (c) SEM micrograph for double patched particles where two distinct triangular patches were introduced onto the particles surface by metal vapor deposition from diagonally opposite sides. Scale bar = 4 μm .

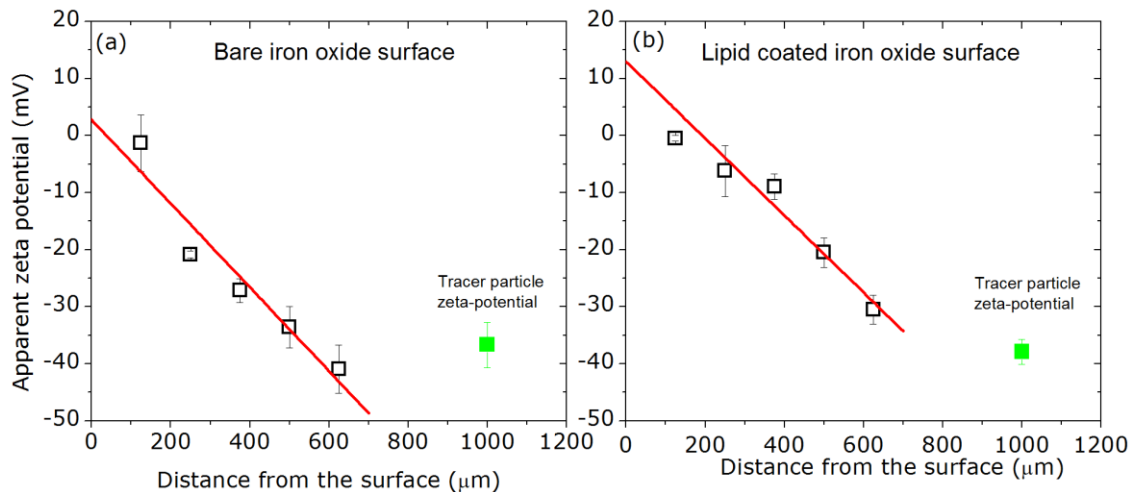


Figure 5.7. Determination of the zeta potential of iron oxide coated flat surface at pH 9.5. Here the zeta potential was determined by measuring the apparent zeta potential (or electrophoretic mobility) of tracer particles (-37 mV) away from the flat surface. The scattered points are experimentally measured data points and the red linear fit to the points.

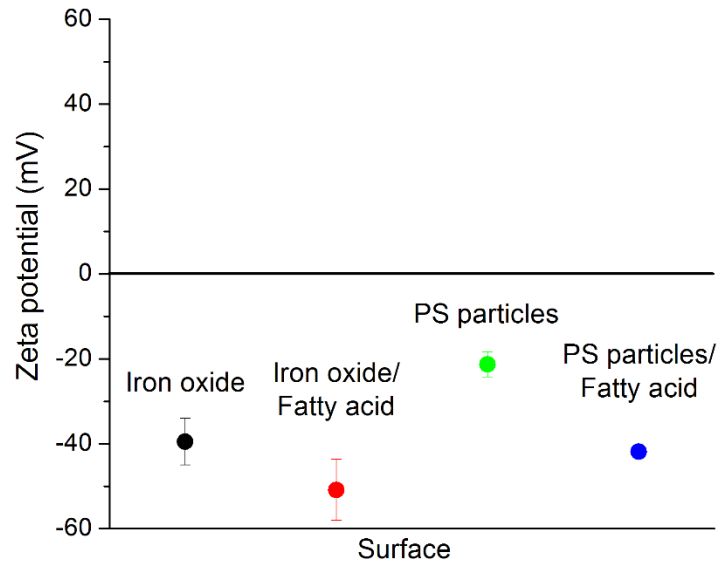


Figure 5.8. Zeta potential of all surfaces present in the assembly dispersion. All the surfaces were negatively charged at pH 9.5 and hence electrostatically repulsive.

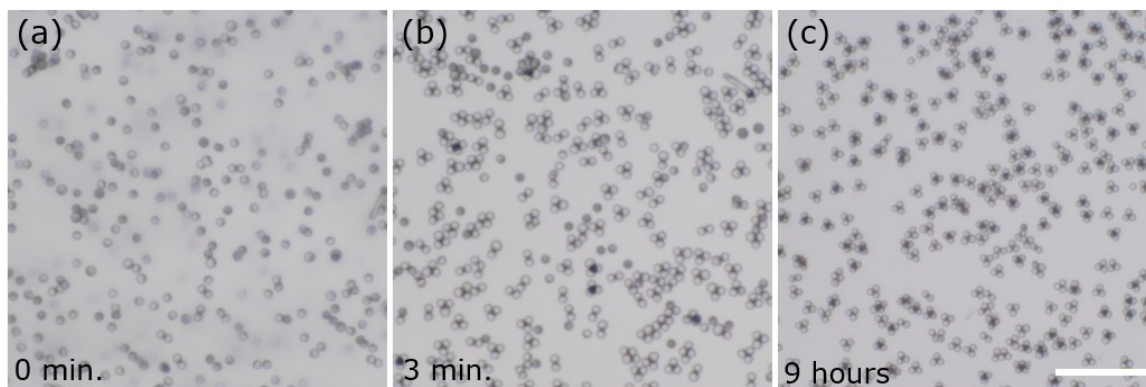


Figure 5.9. Microscope images showing the dynamics of the self-assembly of Janus particles driven by lipid mediated capillary bridging. Mean cluster aggregation number increases as the assembly progresses. The kinetics of assembly is quantified in Figure 5.10. Scale in (c) = 50 μm .

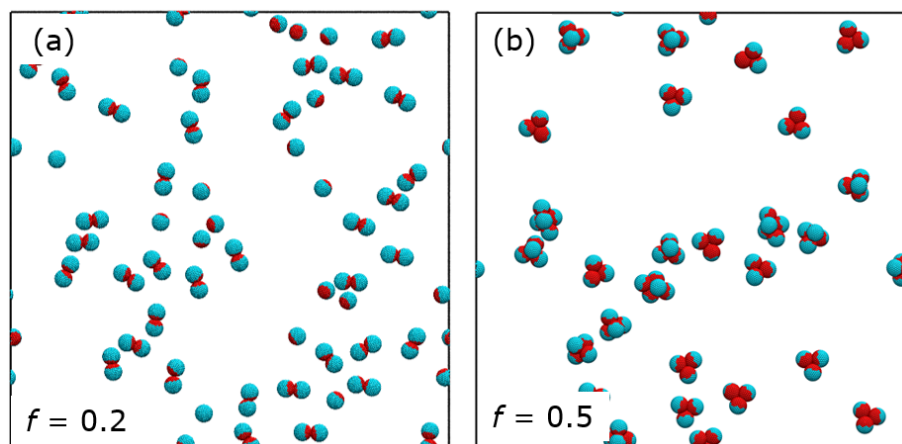


Figure 5.10. Monte Carlo simulation snapshots showing the near-equilibrium clusters formed by patchy particles with surface patch fraction (a) $f = 0.2$, and (b) $f = 0.5$. The red-red patches were attractive, and red-blue and blue-blue patches were repulsive.

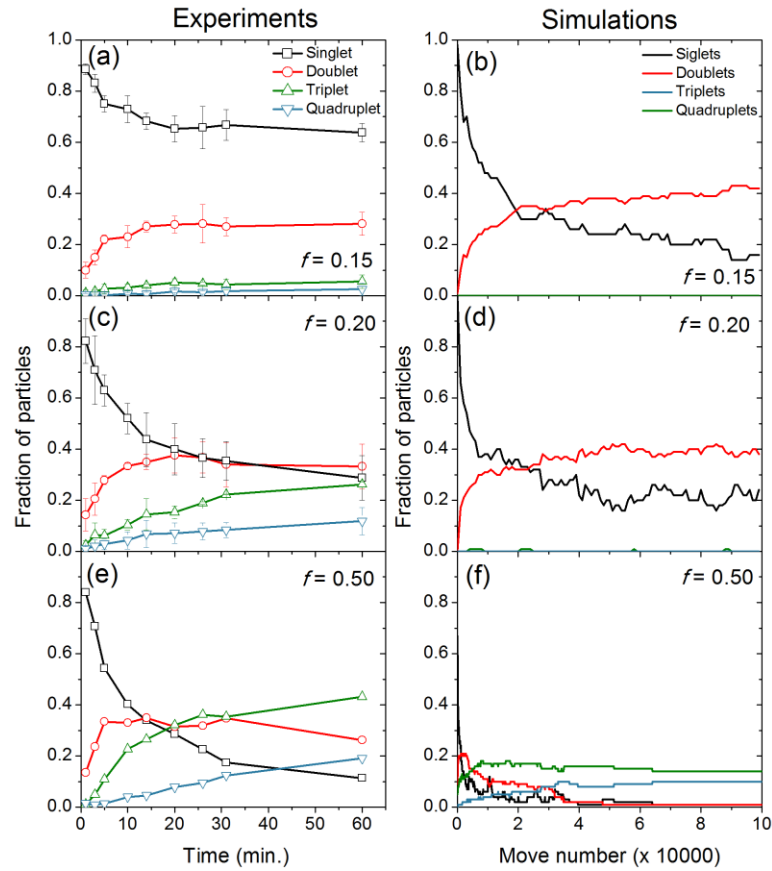


Figure 5.11. Kinetics of particle clustering for different patch sized particles (a-b) $f = 0.15$, (c-d) $f = 0.20$, (e-f) $f = 0.50$. Both MC simulations (b, d, f) and experiments (a, c, e) show similar qualitative behavior where particles assemble (or reassemble) into higher aggregation number clusters with increasing assembly duration (or move number for simulations).

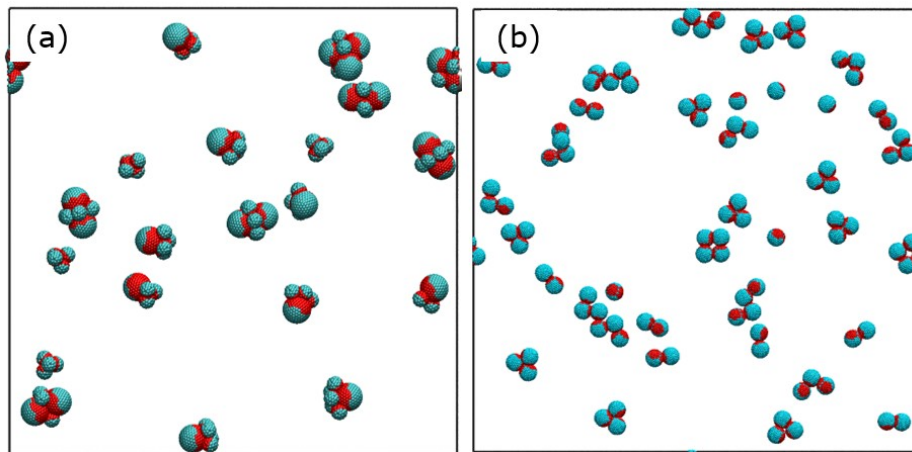


Figure 5.12. Monte Carlo simulations snapshots for the equilibrium clusters formed by (a) Mixture of dissimilar sized particles Janus particles ($f = 0.5$), and (b) Double-patched particles.

CHAPTER 6

Conclusions and Future Work

6.1 Conclusions

In the preceding chapters, we investigated how charge separation affects systems of 2d colloidal spherocylinders, whether a model consisting of four point charges can form a limit periodic structure, how the charge separation and shift in offset dipolar particles affects the structure that they form, and how the surface coverage affects the assembly of Janus spheres under the influence of gravity. We summarize the major findings from these sections below.

Chapter 2. Using DMD simulations we determine that the charge separation has a large effect on the structures that systems of dipolar spherocylinders form, with head-tail contacts dominating the system at large charge separations and side-side contact dominating the system at small charge separations. Rods with small charge separations form dense aggregates while rods with large charge separations form coarse gel-like structures. Structural phase boundaries between fluid, string-fluid, and “gel” (networked) phases are mapped out and characterized as to whether they have global head-to-tail or global side-by-side order. For particles with large charge separations we observe a structural coarsening transition in which the head-tail networks thicken as temperature is lowered. We also find interesting, triangularly-connected networks at intermediate charge separation which may find use in encapsulating smaller particles. These simulations illustrate how the area fraction, connectivity and coarseness of gel structures consisting of rod-like colloidal particles can be controlled by specifying the physical characteristics of the rod particle undergoing the aggregation process.

Chapter 3. Using 2d MC simulations we were able to show that systems of disks with four embedded charges constrained to a triangular lattice are able to form a limit-periodic structure under strict rotational constraints. The formation of the limit periodic structure is not affected by either the distance the charges are from the center of the particle or the angle between the charges, suggesting that a point quadrupole may also be able to form the limit periodic structure. Reducing the restraints on the rotational moveset and allowing either $\pi/6$ rotations or continuous rotations results in striped phases or phases with nematic order. In order to facilitate easy rotation, a shape in between a circle and a hexagon will likely have to be used. The potential energy between the levels of the limit-periodic structure using our model turn out to be zero, meaning the disks interact directly with others of the same level. This is in contrast to prior models whose interactions are either only up to next-nearest neighbors ¹ or nearest neighbors ². The advantages of our model compared to earlier models is that it is simpler than prior models and it forms limit periodic structure with a greater degree of robustness than prior models.

Chapter 4. Quasi-2d Monte Carlo has been used to (a) determine the ground states for a system of offset extended dipolar spheres containing up to four particles and (b) to simulate the assembly of large systems of these particles with two different charge separations at finite temperature. The results from these simulations show that the extent of the shift of the dipole out of the center of the sphere has a large effect on the structure that they form while the charge separation and the area fraction play a lesser role. We find that several of our structures are similar to those found experimentally ³ and those found in prior

simulations of point dipole particles, validating our use of an intermediate range Yukawa potential. By using a shorter-range potential, we are able to explore a larger range of temperatures more efficiently than simulations that employ a longer-range potential. At temperatures lower than previously reported for such systems we find that cyclic structures are able to aggregate into open lattice-like structures.

Chapter 5. Using 3d MC simulations under the influence of gravity we have simulated a system of 100 spheres. Each sphere is modeled as having 252 points distributed evenly on its surface. The identity of the points on the surface of the particle and the interactions that they experience with points on other spheres are designed to mimic recently fabricated Janus particles with both a metal and fatty acid chain surface coating. The structures found via simulation compare well qualitatively with those seen in experiment; the same structural motifs are seen in both. In particular, we find the same two -stage assembly process found in experiment for four particles where a planar arrangement first forms that eventually converts to a tetrahedral arrangement. We find excellent agreement with experiment for the fraction of particles that assemble as a function of the coverage of the Janus sphere.

6.2 Future Recommendations

In this thesis, we have investigated and discussed the effects of charge separation on the self-assembly of colloidal particles. The scope of this work can be extended. Recommendations for future work are summarized below.

6.2.1 Simulations in External Fields

Though we simulated a diverse set of particles in the work outlined in this thesis, we focused only on permanent dipoles outside of an external field. While this is interesting in its own right, one of the main benefits of electrically-responsive colloidal particles is being able to control their behavior via the manipulation of external electric or magnetic fields. We have performed several test simulations using Monte Carlo on offset dipoles in a fixed external field and found the staggered and double chains seen in experiments ³. We implemented the external field in these simulations by including a term in the potential energy calculations equal to $-\vec{\mu} \cdot \vec{E}$ where $\vec{\mu}$ is the dipole moment of an individual particle and \vec{E} is the external field vector ⁴. Further investigation into this system via Monte Carlo simulations would be interesting. We could compare the structures formed in the field to the structures formed in zero field and see how the charge separation affects the separation between nearest neighbors in the aligned chains. Additionally, several recent papers have focused on how time-dependent fields affect the assembly of colloidal particles ⁵⁻⁷. Molecular dynamics, particularly Brownian and Langevin dynamics which have been used in prior simulations involving external fields ⁸, would be more appropriate than Monte Carlo in order to investigate these types of systems. Molecular dynamics simulations have already been performed on magnetic Janus colloids under the influence of a precessing magnetic field, resulting in the formation of microtubules ⁵.

We could also simulate dipolar particles under the effect of external fields using DMD. The implementation of this is not as straightforward as the MC case, but there are several possibilities. The first of these is to implement a “ghost” collision which would

impart a velocity to a positive charge in one direction along the field line and to the negative charge in the direction antiparallel to the direction of the negative charge. This is similar to how the Andersen thermostat maintains the temperature in DMD. However, it is not exactly clear how the frequency or the strength of the collisions corresponds to an experimental quantity. Regardless of the method used, the incorporation of a time dependent field would likely have to be done in steps with each step changing the field direction or magnitude discretely.

6.2.2 3d Offset Dipolar Spheres

Our investigation into offset dipoles in 2d in Chapter 4 found that systems of these particles form several interesting structures including open lattices. Continuing this investigation in 3d would likely result in the discovery of even more complicated structures. Simulations of 3d offset point dipoles by Arzu et al. ⁹ resulted in the formation of several structures, similar to those found in quasi-2d. However, the ground state analysis from these 3d simulations found a structure that is not possible in quasi-2d: an assembly of four particles placed at the vertices of a tetrahedron. If a system is found to form such tetrahedron assemblies at an intermediate temperature it would be interesting to determine what these tetrahedrons would self-assemble into at very low temperature. If they behaved similarly to the triangular assemblies in Chapter 4, spherical assemblies of tetrahedrons may form that would further assemble into an open 3d analogue of a kagome lattice.

6.2.3 Spheres with Four Embedded Point Dipoles

As mentioned in Chapter 3, the chirality of our particles in the double-dipole disk simulations are important. One of the suggested modifications to the model in order to make it more experimentally feasible is to change the point charges into point dipoles oriented perpendicular to the plane of the disk so that even if the particle “flipped” it would still have the same chirality. Simulating systems of these particles would help determine if a more robust model could form the limit-periodic structure. Dealing with point dipoles would require Ewald sums which may inhibit the formation of the limit-periodic structure since Ewald sums have been found to enhance periodicity ¹⁰. If this turns out to be the case, it may be worthwhile to attempt to simulate extended dipoles so that each disk would have eight total charges split over four extended dipoles. Further modifications to the model could include allowing for out-of-plane rotation or changing the particle shape from circular to something in between a hexagon and a circle shape, i.e. a hexagon with rounded edges, with the exact shape having to be tuned.

6.3 References

1. T. W. Byington and J. E. S. Socolar, *Phys. Rev. Lett.*, 2012, 108, 045701 (DOI:10.1103/PhysRevLett.108.045701).
2. C. Marcoux, T. W. Byington, Z. Qian, P. Charbonneau and J. E. S. Socolar, *Physical Review E*, 2014, 90, 012136 (DOI:10.1103/PhysRevE.90.012136).
3. S. K. Smoukov, S. Gangwal, M. Marquez and O. D. Velev, *Soft Matter*, 2009, 5, 1285-1292 (DOI:10.1039/b814304h).
4. H. Schmidle and S. H. L. Klapp, *J. Chem. Phys.*, 2011, 134, 114903 (DOI:10.1063/1.3564916).
5. J. Yan, M. Bloom, S. C. Bae, E. Luijten and S. Granick, *Nature*, 2012, 491, 578-+ (DOI:10.1038/nature11619).
6. A. Snezhko and I. S. Aranson, *Nature Materials*, 2011, 10, 698-703 (DOI:10.1038/NMAT3083).
7. J. Yan, S. C. Bae and S. Granick, *Soft Matter*, 2015, 11, 147-153 (DOI:10.1039/c4sm01962h).
8. S. H. L. Klapp, *Current Opinion in Colloid & Interface Science*, 2016, 21, 76-85 (DOI:10.1016/j.cocis.2016.01.004).
9. A. B. Yener and S. H. L. Klapp, *Soft Matter*, 2016, 12, 2066-2075 (DOI:10.1039/c5sm02648b).
10. C. J. Fennell and J. D. Gezelter, *J. Chem. Phys.*, 2006, 124, 234104 (DOI:10.1063/1.2206581).